ADVANCED IMAGING OF DISEASE: FETAL ALCOHOL SPECTRUM DISORDERS AND DUCHENNE MUSCULAR DYSTROPHY

A Dissertation

by

SHARLA MAE BIRCH

Submitted to the Office of Graduate and Professional Studies of
Texas A&M University
in partial fulfillment of the requirements for the degree of

DOCTOR OF PHILOSOPHY

Chair of Committee,	Joe N. Kornegay
Committee Members,	Shannon E. Washburn
	Brian F. Porter
	Ann B. Kier
	Mark W. Lenox
Head of Department,	Ramesh Vemulapalli

December 2016

Major Subject: Veterinary Pathobiology

ABSTRACT

Advanced imaging techniques are being increasingly utilized as quantitative biomarkers and outcome parameters to identify and monitor disease and evaluate new treatments. Validation of these techniques in animal models is imperative to reliably interpret results and apply them clinically in humans. Studies reported here utilized computed tomography (CT) and magnetic resonance imaging (MRI) to characterize the sheep model of fetal alcohol spectrum disorders (FASD) and the golden retriever (GRMD) model of Duchenne muscular dystrophy (DMD). Objective biomarkers are necessary to help identify some children with (FASD) who do not demonstrate the facial dysmorphology criterion for diagnosis. The sheep model of first trimester binge alcohol exposure was used to study the utility of CT and MRI to distinguish disease. Based on CT assessment, total skull bone volume was significantly more sensitive than cranial circumference in identifying 6-month-old lambs exposed to binge alcohol. Poor nutrition may also contribute to adverse developmental outcomes of prenatal alcohol exposure and choline supplementation has shown benefit in rodent models. Magnetic resonance imaging (MRI) was used to study the brains of 6-month-old lambs from alcohol-exposed pregnant sheep supplemented with and without choline throughout pregnancy. Total brain volume in lambs was reduced regardless of choline supplementation. Duchenne muscular dystrophy (DMD) is an X-linked disease caused by mutations in the dystrophin gene. Therapies for DMD must be assessed using objective biomarkers such as MRI to document potential benefit. The lack of studies correlating MRI indices and histopathologic lesions has limited interpretation. The pectineus muscle from GRMD dogs was used to register and correlate histology with MRI using a novel registration technique, compare histology segmentation between Aperio and a custom algorithm for automated histomorphometry, and compare metrics between 4.7T and 3T scanners. We found that histology and MR images co-registered but metrics were poorly correlated. Aperio and the custom algorithm had similar results and with optimization, it could be applied to the current research. Only T1 values were correlated between MRI scanners but neither T1 values, nor any of the 3T metrics correlated with histologic segmentations. Multiple imaging modalities outlined in this dissertation show the usefulness of objective quantitative techniques that could be adapted and applied to any disease entity.

DEDICATION

This work is dedicated to my son Byron. From the time I was a young adult, I knew that someday I would be a mother. You are the part that completes me, the reason I live, and the reason I have spent countless years pursing this amazing career. During the first seven years of your life you accompanied me through an anatomic pathology residency, studying for my pathology board certification exam and becoming board certified, the start of a PhD, the start of a post-doctoral position, and finally the completion of a PhD. I hope that someday you will understand the sacrifices I made to provide you with an amazing life. This is all for you. I love you to the moon and back. Infinity doubled.

ACKNOWLEDGEMENTS

I would like to thank my committee chair, Dr. Kornegay, and my committee members, Dr. Washburn, Dr. Porter, Dr. Kier, and Dr. Lenox, for their guidance and support throughout the course of this research.

Thank you to Dr. Kornegay for meeting me in the Critical Care Café on one of your visits to Texas A&M. It was during this visit that I found a “home” with your lab. Thank you for helping me develop this somewhat non-traditional PhD that allowed me to work on two entirely different diseases at the same time. I never imagined in a million years that this is where my career would have taken me.

Thank you to Dr. Shannon Washburn for assisting me in completing and publishing the two fetal alcohol imaging studies outlined in this dissertation. We managed to hold all of the pieces together during an extremely tough time. I have thoroughly enjoyed working with you and I hope that we can collaborate in the future.

Thank you to Dr. Lenox for all of your help in the world of imaging. I came to you with a small grant and you moved mountains to get me everything I needed for the fetal alcohol studies. Your passion for invention and technology is inspiring.

Thank you Dr. Porter for your guidance while I was a pathology resident. You convinced me to do this PhD even though I was adamantly against it when I came to A&M. It was through you that I met Dr. Cudd and began working in fetal alcohol research. Thanks for pushing me to pursue the PhD.

Thank you Dr. Kier (and Dr. Porter) for encouraging me to apply for the NIH T32 grant. I can't express how important the grant was in not only helping me decide to do a PhD, but also financially making it possible. What an amazing opportunity.

Thank you to my colleagues and lab mates in the Kornegay lab. Cindy, you are one of a kind. I am so happy to have you as a mentor and friend. Ben, Jack, Sarah, Mary, Ezgi, Sara and Pete, my time in the lab with you has been fantastic. I will consider you all friends for life. Mandy and Heather, without the two of you, the life line of the lab would not exist. Thank you times a million for all your help with the dogs, sample collection, and everything else I ever needed.

Thanks also go to my friends and colleagues and the veterinary pathobiology department faculty and staff for making my time at Texas A&M University a great experience. I also want to extend my gratitude to the National Institutes of Health (NIH) institutional T32 training program grant to Texas A&M University College of Veterinary Medicine and Biomedical Sciences for funding three years of PhD graduate studies and salary. Thanks also to Solid Biosciences for supporting one year of graduate studies and for funding a two year postdoctoral position at Texas A&M University.

Thank you to the late Dr. Tim Cudd for helping me regain a passion for research and for getting me involved in fetal alcohol research. Your work ethic, love for research, and your kind heart were all inspirational to me. You may be gone but the impact you left on me will never be forgotten. I am so very grateful that we crossed paths, if only for a few years. Godspeed.

Thank you to my friends for putting up with my crazy study schedules, work commitments, and absence from life in general while pursuing this degree and all of my other studies. Most of you think I'm crazy, hopefully my new found sanity will convince you otherwise.

Thank you to my parents, Dan and Billie Jo, for your constant encouragement and for always supporting me in every decision I ever made over the past 37 years (even when I said I wanted this PhD). I hope that I have made you proud. I could never thank you enough for everything that you've done. My student status is finally ending after grade 32. I told you I wouldn't be a (paying) student forever!

Thank you to my son Byron. You have taught me that it is possible to love someone more than life itself. You have also taught me balance. I love my career and I love being a mom. It's possible to be happy and have both. You are a constant reminder of why I do what I do. You give me the day-to-day strength to continue doing research and finding answers for children affected by these two devastating diseases. I am dedicated to doing what I can as a mother, veterinarian, pathologist, researcher, and professor to benefit the world in what little time I have on this earth.

CONTRIBUTORS AND FUNDING SOURCES

Contributors

This work was supported by a dissertation committee consisting of Professor Dr. Joe N. Kornegay (advisor) joint appointment in the Department of Veterinary Integrative Biosciences (VIBS) and Veterinary Pathobiology (VTPB) and Director of the Texas A&M Institute for Preclinical Studies (TIPS), Clinical Associate Professor Dr. Shannon E. Washburn of the Department of Veterinary Physiology and Pharmacology (VTPP), Clinical Associate Professor Dr. Brian F. Porter of the Department of Veterinary Pathobiology (VTPB), Professor Dr. Ann B. Kier of the Department of Veterinary Pathobiology (VTPB), and Adjunct Professor Dr. Mark W. Lenox of the Department of Biomedical Engineering.

The choline mass spectroscopy pilot study work described in chapter III was conducted in part by Dr. Jan Adams and Dr. Carl Keen of the Department of Nutrition at UC Davis.

Those participating in the fetal alcohol portions of the studies wish to acknowledge the primary and important role of the late Dr. Timothy Cudd in designing and initiating this work.

Funding Sources

The studies outlined in Chapters II and III were supported by Texas A&M CVM Post-Doctoral Grant (SMB) and NIAAA Grant AA017120 and AA18166-2 (SEW). This work was done in conjunction with the Collaborative Initiative on Fetal Alcohol Spectrum

Disorders (CIFASD), which is funded by grants from the National Institute on Alcohol and Alcohol Abuse (NIAAA). Additional information about CIFASD can be found at www.cifasd.org.

Three years of graduate study and salary were funded by the National Institutes of Health (NIH) institutional T32 training program grant to Texas A&M University College of Veterinary Medicine and Biomedical Sciences (2012-2015).

One year of graduate study and a two year postdoctoral position were funded by Solid Biosciences.

TABLE OF CONTENTS

LIST OF FIGURES

LIST OF TABLES

Page

CHAPTER I

INTRODUCTION

I.1 History of magnetic resonance imaging (MRI)

MRI has advanced tremendously since it was first used clinically over 30 years ago with it now being a primary diagnostic modality commonly found in a majority of medical clinics, hospitals, and research institutions around the world. The first clinical scanner was used in the early 1980s but the history of MRI dates back some 40 years before that when Isidor Isaac Rabi described nuclear magnetic resonance (NMR). Rabi developed a way to measure the magnetic characteristics of atomic nuclei and was awarded a Nobel Prize in Physics in 1944. Two other physicists, Felix Bloch and Edward Purcell, independently observed NMR in solids and liquids earning them a shared Nobel Prize for Physics in 1952 [1, 2]. Erwin Hahn developed spin echo in 1950 [3] while in 1966 Richard Ernst developed Fourier transform NMR spectroscopy, earning a Nobel Prize in Chemistry in 1991 for his contributions [4]. Raymond Damadian made an exciting discovery in 1971 when he utilized NMR to evaluate T1 and T2 relaxation times in rat tumors, finding tumor tissue had longer T2 times [5]. The foundation for MRI as we know it today was ultimately laid by Paul Lautebur and Peter Mansfield when they independently described magnetic field gradients to localize NMR signals, and their contributions earned a shared Nobel Prize in Physiology/Medicine in 2003 [6, 7]. Following this important ground work, Damadian produced the first MR images of the human thorax in 1977 while Mansfield and Maudlsey imaged a human finger [8]. During the next three years, the human wrist, abdomen, head, and body were all scanned [9-12] and the first commercial scanner was released in 1983 by General Electric and Siemens. In the late 80s, Michael Moseley developed techniques in diffusion imaging with fMRI [13, 14] and Le Bihan et al. continued that work with diffusion coefficients [15] eventually leading to diffusion tensor imaging (DTI) and blood oxygenation level-dependent (BOLD) methods in 1990 [16, 17].

Since the early 90s, there is an ever growing number of techniques that are being developed and techniques currently in use that far exceed the rudimentary scans done in early investigations as described above. Each year there are thousands of publications that outline new techniques, methods for analysis, and advancements in the imaging field. Importantly, we are now evaluating MRI as an outcome biomarker for pre-clinical research because it is non-invasive and it provides objective and quantifiable outputs. Studies outlined in this dissertation demonstrate the immense potential that MRI holds in clinical evaluations, therapeutic development, and future research in two entirely different disease entities, fetal alcohol spectrum disorders (FASD) and Duchenne muscular dystrophy (DMD).

I.1.1 Magnetic resonance imaging (MRI) for brain scans in fetal alcohol spectrum disorders (FASD)

Fetal alcohol spectrum disorders (FASD) is an umbrella term that encompasses a full range of effects resulting from prenatal exposure to alcohol, with fetal alcohol syndrome (FAS) being the most severe [18]. Over a span of nearly 20 years, binge drinking among pregnant women has not significantly declined [19] and in the United

States, FASD is a leading cause of preventable birth defects and developmental disorders [20]. Because FASD is still a problem today, MRI has become one of the leading diagnostic tools in identifying children with abnormalities.

For the first time in 1992, two children with fetal alcohol syndrome were imaged with MRI and structural abnormalities in the brain were reported [21]. Prior to this time, abnormalities had been reported but they were primarily based on postmortem examination in infants [22]. This discovery has led to numerous reports in both humans and animals documenting brain changes related to alcohol exposure. One of the most consistent findings in studies of FASD is an overall volumetric reduction [23-28] as well as global decreases in brain volume [25, 29]. More focused studies have documented abnormalities in the corpus callosum that include volume reductions [30], shape changes [31-33], complete [24, 30, 34] and partial agenesis and hypoplasia [21, 24, 35, 36]. The cerebellum is another target of alcohol exposure with reports of decreased volume and surface area [21, 25, 35] increased sensitivity in the anterior vermis [35, 37], and hypoplasia [36]. Since the cerebellum is involved with motor function and attention regulation, deficits in attention [38], balance [39], coordination [40, 41], verbal learning, and memory [42] may be related to increased sensitivity in this part of the brain. The basal ganglia is also a target of alcohol, specifically causing volume reductions in the caudate nucleus [21, 25]. This portion of the brain has been tied to verbal learning and recall and could account for deficits in affected children [43]. Abnormal brain networks in this portion of the brain can result in behavioral changes, deficits in executive functioning [44, 45] and also connections to the motor cortex [46] associated with coordination [41, 47] and fine motor skills [48, 49]. The hippocampus is another structure commonly studied in FASD but some studies have reported a reduced volume [35, 50] while others report that the hippocampus is spared [25]. Joseph et al. recently showed shape variations in the hippocampus associated with prenatal alcohol exposure [51]. A recent study found that moderate alcohol doses administered in a binge like pattern throughout gestation fail to alter cell numbers in the hippocampus and the olfactory bulb and that high exposure during the third trimester is required for injury [52]. Finally, whole brain studies have revealed that heavy prenatal alcohol exposure results in increased gray matter and relatively less white matter as well as thicker cortices [29, 53, 54]. Children with thinner cortices showed increased verbal performance [55] and intellectual function [56] while the FASD group had signs of immature brain development.

As evidenced from the literature above, it is clear that prenatal alcohol exposure affects a large number of structures in the brain thus making it a focus in research with imaging modalities like MRI. Volumetric reductions are often used as biomarkers but as potential treatments and interventions are developed, animal model mechanistic studies are imperative to control for population and alcohol exposure differences often seen in human studies. The ovine model offers significant benefits over the mouse, most notably with *in utero* brain development more closely tracking with humans [57]. Also, there are a vast number of new techniques and imaging technologies first used in fetal alcohol research over the last decade that need to be critically evaluated in animal models if they will be used as biomarkers, like diffusion tensor imaging (DTI) [26, 58-61], magnetic resonance spectroscopy (MRS) [62-64], single photon emission computed tomography

(SPECT) [34, 50, 65], positron emission tomography (PET) [66], and functional magnetic resonance imaging (fMRI) [27, 67-72]. The study outlined in chapter III of this dissertation utilizes MRI and quantitative techniques to evaluate the brain when a therapeutic intervention is introduced.

I.1.2 Magnetic resonance imaging (MRI) for skeletal muscle scans in Duchenne muscular dystrophy (DMD)

Duchenne muscular dystrophy (DMD) is an X-linked progressive degenerative skeletal muscle disease that affects 1: 3,500 boys and results from mutations in the dystrophin gene [73]. Boys are typically diagnosed with DMD between 3-5 years of age, they are wheelchair bound by their early teens and they often die from cardiopulmonary complications between 20-30 years old. Despite our detailed knowledge of dystrophin and scientific advancements over the last thirty years, there is no cure for DMD. Non-invasive methods such as MRI are crucial in monitoring disease progression and in determining the efficacy of new treatments as they are developed and tested.

MRI was first used in 1986 to analyze and compare normal patients to patients with pathologic skeletal muscle disease, including DMD [74]. This study and numerous others that followed showed that MRI had the capability to distinguish structure and composition changes in the skeletal muscle of DMD patients [75-78]. Qualitative skeletal muscle assessment initially used T1 weighted images and post contrast imaging to identify structure defects [77-80]. T1 values in DMD are typically high early in the disease and then the values decline as the disease progresses and also as the muscle are replaced with fatty deposits [78]. In a study evaluating nine skeletal muscles, eight muscles had a significant difference in the T1 weighted signal intensities when DMD patients treated with steroids were compared to healthy controls [81]. Garrood et al. also showed that gadolinium enhancement was increased in the tibialis muscles of DMD patients doing exercise and that the T2 values in thigh muscles were significantly higher than normal controls. Eight out of nine muscles also showed an increase in T1 weighted signal intensity in DMD patients compared to normal, suggestive of fat infiltration [81].

Muscle cross sectional area is another technique used in quantitatively evaluating DMD. This technique measures individual muscles traced on axial slices from T1 weighted images. Mathur et al. found that the cross sectional area in the posterior calf muscles were greater (~60%) in DMD boys compared to normal controls but the tibialis and quadriceps were not significantly different. Additionally, DMD boys under the age of ten had a larger cross sectional areas in the quadriceps compared to controls but this cross sectional area became smaller as the boys got older (>10 years old) and the disease progressed [82]. Another studied evaluated the proportion of contractile skeletal muscle to non-contractile tissue in DMD boys and found that proportions of non-contractile tissue were greater compared to controls and non-contractile tissue also increased with age. This proportion of non-contractile tissue also correlated with several functional tests (rise from floor, timed 30 ft. walk, ascending steps) [83]. T2 weighted images are also valuable in evaluating DMD and have been shown to reflect muscles changes associated with damage, inflammation and fat infiltration. Kim et al. found that the T2 value from the gluteus maximus muscles was highly correlated to the non-quantitative MRI score for fat infiltration. This T2 value also correlated with clinical measures including age, clinical function scale, timed Gower score and time to run 30ft [84]. T2 values can also be used to map a region of interest longitudinally, and thus muscle heterogeneity can be monitored with disease progression [75]. Fat suppression sequences have also become important when evaluating DMD boys because early in the disease, the muscles are infiltrated with edema and inflammation versus fat later on. Short-tau inversion recovery images (STIR) suppress the fat and allow extracellular water associated with edema and inflammation to become more definable. Marden et al used STIR sequences and discovered that young boys lacking fatty infiltration had increased areas of signal intensity associated with edema and inflammation that would have otherwise been missed [77].

The three-point Dixon technique is beneficial in studying DMD because it allows the signal intensities in each voxel of tissue to be separated into values for both fat and water. This sequence produces high resolution maps for fat and water that allow fat to be quantified in individual muscles. In a study of DMD boys, the three-point Dixon technique was used to quantify fat in the thigh muscles and the results showed that quantitative fat values correlated better with disease severity than strength measures [85]. Magnetic resonance spectroscopy (MRS), proton spectroscopy (^{1}H) and phosphorus (^{31}P), has also been used to study muscles in DMD [86-88] and is beneficial in that it allows muscles metabolites to be evaluated [75]. Torriani et al. showed in a study of lower leg muscles in DMD boys that there is a distinct pattern of involvement and increased fat deposition that correlates with functional measures [87]. Hsieh et al. used MRS and found that boys with DMD have reduced trimethylamines to muscle total creatine ratio and that this correlates negatively with function [89]. In 2015, MRI with ^{1}H-MRS and T2 maps were used to evaluate 42 boys with DMD and 31 normal controls. T2 maps were found to be more accurate than MRS in the gluteus maximus and vastus lateralis. MRS fat fractions likely underestimate the actual fat because of the presence of edema associated with the disease [88].

Diffusion weighted imaging (DWI) has also been used to evaluate muscle pathology and several reports show that DWI derived quantitative parameters can potentially be used as biomarkers or outcome measures [90, 91]. The apparent diffusion coefficient (ADC) has been shown to be elevated in inflammatory myopathies, with fractional anisotropy (FA) showing inconsistent results [92, 93]. In a DMD study, DWI parameters correlated with clinical and NMR markers for disease severity [90] but a longitudinal study has not been done. Changes in ADC and FA in DMD are primarily due to the degree of fat infiltration. In a recent study of DMD boys, an increase in ADC was identified in the tibialis muscle when the effects of fat and signal to noise were taken into account [94].

As evidenced above, MRI has become an important tool for studying muscle over the last two decades because it is non-invasive and readily available. A majority of the reports listed above focus on several physiologic and pathologic events that take place in Duchenne muscular dystrophy that allow for visual changes on MRI including 1) muscle necrosis which leads to edema and inflammation, 2) continued cyclic damage which ultimately leads to fibrofatty infiltration, and 3) the eventual loss and atrophy of muscle mass. The use of MRI in skeletal muscle is definitely not as refined as its use in the brain but as technology continues to advance, quantitative methods to identify outcome parameters in DMD will continue to be validated. The techniques outlined in chapter IV of this dissertation are novel and to the author's knowledge, have not been used in evaluating DMD.

I.2 History of computed tomography (CT)

Computed tomography wouldn't exist today if it weren't for the accidental discovery of radiation and ultimately X-rays by Wilhelm Conrad Röntgen in 1895 [95]. His initial experiments were reported in the New York Times and by 1901 he was awarded the first ever Nobel Prize in physics for his discovery. The world was fascinated with x-ray pictures but E. Thompson was already trying to develop three-dimensional x-ray images using stereoscopic techniques. Doctor Karol Meyer developed an early method resembling the process of scanning by computed tomography. He obtaining stratigraphic images with a moving X-ray tube and stationary film cassette. Carlo Baese patented a simultaneous moving tube and cassette in 1915. Johann Radon published his work on "radon transform" in 1917 which was the mathematical basis of CT, explaining that density can be reconstructed. Allesandro Vallebona implemented stratigraphy in the early 1930s whereby the x-ray source and film detector were fixed to a pendulum. Some of his theories were wrong but the helped lead to computed tomography. In the mid-50s, Allan Cormack was interested in radiotherapy treatment so he developed a mathematical approach to solving problems with variations in body tissues. He then moved to Harvard and worked on image reconstruction of x-ray projections and he built a tomographic device in 1963. Independently of Cormack, Godfrey Hounsfield worked on the technical development of radar air defense systems. Hounsfield began his research in tomography by initially using gamma radiation and he used the power of computers to solve the problem of image reconstruction. This is how the term “computed” tomography came about. The gamma ray source in early scanners had low output so some exposures took over nine days to complete. The first image with enough detail to tell the difference between tissues of a formalin fixed brain took 2.5 hours to reconstruct and was 80 x 80 pixels in resolution. This device was patented in 1968. In clinical testing, the gamma tube was replaced with an x-ray tube and scan time was shortened to nine hours with a reconstruction time of twenty minutes. In 1971, the prototype scanner EMI Mark I was installed at Atkinson Morley’s Hospital with the help of neurologists James Ambrose and Louis Kreel [95]. The opening was only large enough to scan a head. The first tomographic examination was of a woman with a suspected brain tumor. The image produced made it possible to differentiate brain tissue from a developing cyst. In 1972, Hounsfield formally presented his results and by the end of 1973 [96], the first commercial CT scanner was on the market, EMI CT 1000. Advancements in the machine made it possible to acquire an image in 20 seconds and then the resolution was increased to 320 x 320 pixels. In 1979 both Cormack and Hounsfield were awarded the Nobel Prize for Physiology or Medicine. Remarkable advancements have taken place since this time most notably the fan-beam (1976), spiral CT (1989), 4-slice spiral CT (1998), 8-slice spiral CT (2001), 16-slice spiral CT (2002), 64-slice spiral CT (2004), dual-source CT (2005), 320-slice spiral CT (2007), high-definition CT (2008), and 640-slice spiral CT (2012). Additionally, the future of CT involves fusion imaging in which there is superimposition of images from two dependent imaging modalities to produce an image which provides greater information. Examples are positron emission tomography (PET)-CT, single-photon emission computerized tomography (SPECT)-CT, and CT-MRI.

One of the benefits of CT is that it can be used for quantitative data collection and analysis on both bone and soft tissues in one scan. Facial measures are routinely taken clinically in children suspected of prenatal alcohol exposure. These same facial measures can be taken with CT by creating a 3D reconstruction of the face. Additionally, the underlying bone can also be evaluated. CT was used to evaluate both soft tissue and bone in the sheep model of FASD outlined in chapter II of this dissertation.

I.2.1 Computed tomography (CT) and fetal alcohol spectrum disorders (FASD)

There are currently no published studies that utilize computed tomography in FASD. A major downside in CT imaging involves concerns over radiation exposure leading to CT technology and manufacturers claiming to generate the desired image with the lowest radiation dosage for particular studies. The “Alliance for Radiation Safety in Pediatric Imaging” initiated a campaign called “Image Gently” with goals to reduce radiation exposure in children by amending adult protocols. Additionally, the benefit gained from imaging needs to exceed the overall risk. It is likely that because of this campaign, the study outlined in chapter II of this dissertation would not be clinically applicable at this time. However, as computer and CT technology advance, the benefit of scanning a child with fetal alcohol spectrum disorders will far outweigh the risk and the techniques explained in this dissertation will have already been validated in an animal model.

CHAPTER II

COMPUTED TOMOGRAPHY ASSESSMENT OF PERIPUBERTAL CRANIOFACIAL MORPHOLOGY IN A SHEEP MODEL OF BINGE ALCOHOL DRINKING IN THE FIRST TRIMESTER*

II.1 Overview

Identification of facial dysmorphology is essential for the diagnosis of fetal alcohol syndrome (FAS), however, most children with fetal alcohol spectrum disorders (FASD) do not meet the dysmorphology criterion. Additional objective indicators are needed to help identify the broader spectrum of children affected by prenatal alcohol exposure. Computed tomography (CT) was used in a sheep model of prenatal binge alcohol exposure to test the hypothesis that quantitative measures of craniofacial bone volumes and linear distances could identify alcohol-exposed lambs. Pregnant sheep were randomly assigned to four groups: heavy binge alcohol, 2.5 g/kg/day (HBA); binge alcohol, 1.75 g/kg/day (BA); saline control (SC); and normal control (NC). Intravenous alcohol (BA; HBA) or saline (SC) infusions were given three consecutive days per week from gestation day 4-41, and a CT scan was performed on postnatal day 182. The volumes of eight skull bones, cranial circumference, and 19 linear measures of the face and skull were compared among treatment groups. Lambs from both alcohol groups showed significant reduction in seven of the eight skull bones and total skull bone volume, as well as cranial circumference.

---

*Reprinted with permission from “Computed tomography assessment of peripubertal craniofacial morphology in a sheep model of binge alcohol drinking in the first trimester” by Birch SM, Lenox MW, Kornegay JN, Shen L, Ai H, Ren X, Goodlett CR, Cudd TA, Washburn SE, 2015. *Alcohol*, 49(7): 675-89, Copyright © 2015 by Elsevier Inc.

Alcohol exposure also decreased four of the 19 craniofacial measures. Discriminant analysis showed that alcohol-exposed and control lambs could be classified with high accuracy based on total skull bone volume, frontal, parietal or mandibular bone volumes, cranial circumference, or interorbital distance. Total skull volume was significantly more sensitive than cranial circumference in identifying the alcohol-exposed lambs when alcohol-exposed lambs were classified using the typical FAS diagnostic cutoff of $\leq 10^{th}$ percentile. This first demonstration of the usefulness of CT-derived craniofacial measures in a sheep model of FASD following binge-like alcohol exposure during the first trimester suggests that volumetric measurement of cranial bones may be a novel biomarker for binge alcohol exposure during the first trimester to help identify non-dysmorphic children with FASD.

II.2 Introduction

The teratogenic effects of alcohol abuse during pregnancy were formally identified as fetal alcohol syndrome (FAS) about four decades ago [97]. FAS is diagnosed primarily based on three criteria: 1) presence of at least two of three characteristic dysmorphic facial features (smooth philtrum, thin upper lip, and short palpebral fissures); 2) growth deficits in height and/or weight; and 3) structural, neurologic, or functional central nervous system (CNS) abnormalities [98, 99]. It is now recognized that the large majority of children with untoward effects from prenatal alcohol exposure do not fully meet the criteria for a diagnosis of FAS, but still express a broad range of skeletal, neurological, developmental, behavioral or learning abnormalities [100-102]. In 2004, the designation fetal alcohol spectrum disorders (FASD) was adopted as an umbrella term to encompass the full range of effects resulting from prenatal exposure to alcohol, with FAS being the most severe [18].

In the United States, FASD is a leading cause of preventable birth defects and developmental disorders [20] with a prevalence ranging from 1% of all births [103, 104] to as high as 2-5% [105]. FASD places a large burden on the economy, with estimates of the cost as high as $4 billion annually due to health care, lost productivity, and special education [103, 106]. Despite extensive efforts to inform the public about the risks of alcohol use during pregnancy, 7% of approximately half a million pregnant women surveyed had consumed alcohol in the previous 30 days and 1.4% reported binge drinking [107]. Over a span of nearly 20 years, binge drinking among pregnant women has not significantly declined [19].

Optimal management of children with FASD depends on accurate identification of the full spectrum of children adversely affected by prenatal alcohol exposure. Diagnosis of FAS through clinical screening relies on trained recognition or anthropometric measurements of dysmorphic features of soft tissue structures of the face, yet children with FAS constitute fewer than 10% of all children with FASD. Reliable indicators of adverse effects of prenatal alcohol exposure are needed to help identify the much larger number of children with FASD who do not meet the facial dysmorphology criterion. Quantitative analysis of craniofacial bones, which are derived from embryonic neural crest cells that are sensitive to alcohol exposure during neurulation [108], provides a potential approach for identifying a more sensitive indicator. Relatively little work has been done to evaluate the underlying craniofacial bones, and its potential use as a quantitative indicator to identify children with FASD is largely untapped.

Binge drinking during the first trimester (including prior to pregnancy recognition) is the most common pattern of risk drinking in women of childbearing age [109-111]. Craniofacial bone changes are an appropriate candidate as a structural biomarker for binge drinking, in part because of the spatiotemporal links between embryonic CNS and craniofacial development during the first trimester. Bones that form the neurocranium (frontal, parietal, and occipital bones) are derived principally from the neural crest and paraxial mesoderm, whereas bones that form the viscerocranium (mandible, maxilla, nasal, lacrimal, and jugal bones) originate primarily from the first two pharyngeal arches [112]. During neurulation, neural crest cells originate at the junction of the neural folds and eventually the cells migrate to various locations throughout the embryo to form body structures [108]. A subset of neural crest cells, cranial neural crest cells, form structures of the face (bones, cartilage, and cranial nerves) [113], and are highly sensitive to alcohol. Damage to these cells results in dysmorphic craniofacial features and some associated brain abnormalities associated with FAS [114-116].

In humans, key events over the first trimester of pregnancy [117] include neurulation (spanning post fertilization days 22-31) which involves formation of the neural tube and neural crest, with anterior neuropore closure by day 30. Emergence of the full five vesicle stage is evident at five weeks, along with formation of the pontine flexure, optic cup and nasal pit. Formation of the telencephalic cortical plate begins at 7-8 weeks with the appearance of the five zones of the emerging cerebral cortex (marginal, cortical plate, subplate, subventricular and ventricular zones). By comparing the timing of the same events during embryonic development in sheep (that have a 147 day gestation), it is possible to establish temporal equivalence in sheep to the first eight weeks of human development. In sheep, neural tube formation extends into the third gestational week and the anterior neuropore closes by gestational day (GD) 21. The five vesicle stage is evident in the fourth gestational week, while the cortical plate begins forming in the lateral wall of the telencephalon at GD35. By GD40, the lateral wall has formed a defined cortical plate and the five zones of the emerging cerebral cortex are evident [118]. Comparatively, the first forty days of embryonic development in the sheep is roughly equivalent to the first eight weeks of human development.

Experimental animal models, primarily mouse models, have shown that binge-like alcohol exposure during the first trimester equivalent is sufficient to induce abnormal craniofacial development. These studies have identified key roles of dose and timing of prenatal alcohol exposure in producing craniofacial effects that model some of those seen in FAS [113, 119]. Specifically, they have shown quantitatively that measurable craniofacial changes do occur [120-123]. A major goal of the current study was to extend this approach to a well-defined sheep model of binge alcohol exposure during a portion of the first trimester equivalent, to assess whether quantitative analyses of craniofacial bone volumes using computed tomography (CT) in six-month-old (peripubertal) lambs could accurately predict exposure.

In this study, sheep were evaluated at six months of age because we wanted a target age comparable to middle school-aged children about to enter puberty during early adolescence. Sheep reach puberty when they attain 50-70% of their mature body weight, typically between 7-8 months of age, depending on breed [124]. Therefore, the developmental status of these lambs may be analogous to children in their middle school years with undiagnosed FASD that have developmental, behavioral, and/or learning deficits often identified by educators. Additionally, we sought to compare the relative accuracy of classifications of prenatal alcohol exposure through a single CT scan which allowed measurement of both cranial bone volumes and linear distance measures taken from bone (cranial) and soft tissue (facial) landmarks, along with cranial circumference. If confirmed, these quantitative approaches in this sheep model could provide new indices of the effects of prenatal alcohol exposure that may prove more sensitive than traditional FAS diagnostic indices (head circumference; facial morphometrics). This could translate into improved identification of children with FASD.

Measures evaluated in the current study include the volume of the bones of the neurocranium and viscerocranium, along with linear measurements of the skull, face, and cranial circumference. CT was utilized because it is non-invasive, readily available in most hospitals, produces high-resolution, three-dimensional images and one scan allows measurement of bony and soft tissue structures of the face. CT has been effectively used to study fixation artifacts in embryologic studies [125] and recently in studies of craniofacial dysmorphology in mouse models of FASD [126, 127]. Repeated weekend binge drinking (3 consecutive days per week) over the first eight weeks of human pregnancy was modeled from GD4-41 in the sheep with two binge-like alcohol treatments. The first treatment modeled heavy binge drinking (2.5 g/kg per day, peak blood alcohol concentrations (BACs) above 250 mg/dl) and the second treatment modeled more typical binge drinking (1.75 g/kg per day, peak BACs around 200 mg/dl). We hypothesized that, relative to the control groups, lambs given binge-like prenatal alcohol exposure would: 1) have reduced CT-derived volumes of the skull bones; 2) have reduced cranial circumferences; 3) have altered craniofacial morphometrics of bone as well as face; and 4) be classified accurately in terms of prenatal alcohol exposure based on one or more of these measures. Because FAS is often associated with binge drinking during the first trimester, comparisons between the two binge treatment conditions could help determine whether more intense binge exposure episodes produce increasingly severe effects on craniofacial morphometrics or skull bone volumes.

II.3 Materials and methods

II.3.1 Animals

All animals and experimental procedures were approved by the Institutional Animal Care and Use Committee (IACUC) at Texas A&M University. Prior to breeding, Suffolk ewes (aged 2-5 years) received multi-species Clostridium bacterin-toxoid (Covexin 8, Intervet/Schering-Plough Animal Health, Summit, NJ) 2 ml intramuscularly, albendazole (Valbazen Suspension 7.5 mg/kg, Pfizer Animal Health, New York, NY) 0.75 ml/25 lb of body weight orally, and ivermectin (Ivomec Drench for Sheep 0.8%, Merial, Duluth, GA) 3 ml/26 lb body weight orally. The day of mating (the day that the ewes were marked by the ram) was designated as GD 0, and ewes entered the experiment the next day. Ewes were penned individually for the experiment but had visual contact at all times with herd mates in adjacent pens in an environmentally regulated facility (22°C and a 12:12 light/dark cycle). Ewes entering the experiment were randomly assigned to one of four treatment groups: normal control (NC), saline control (SC), binge alcohol (BA), or heavy binge alcohol (HBA). Pregnancy was confirmed ultrasonographically on GD 25, and if ewes were not pregnant, they were removed from the experiment. Ewes were fed a "complete" ration (TAMU Ewe Ration, Nutrena, Cargill, Minneapolis, MN) designed to meet 100% NRC requirements as calculated by ARIES (software version 2007, University of California, Davis) and had free access to drinking water. Maternal food consumption was monitored daily. All subjects consumed all feed offered.

Just before parturition, ewes were moved to a covered pen outside where they lambed naturally. At birth, newborn lambs were weighed and measured, and their navels were dipped in iodine (VetOne Stronger Iodine, 7%, MWI, Meridian, ID). They were also given oxytetracycline (Liquamycin®, LA-200®, 200 mg/ml, Pfizer Animal Health, New York, NY) 1 ml intramuscularly and selenium/vitamin E (BO-SE®, 1 mg/ml, Intervet/Schering-Plough Animal Health, Summit, NJ) 0.5 ml subcutaneously. Each ewe was checked for satisfactory milk production, and lambs were closely monitored for nursing, weight gain, and health status over the next two months. At one and two months of age, lambs were vaccinated using multi-species clostridium bacterin-toxoid (Covexin 8, Intervet/Schering-Plough Animal Health, Summit, NJ) 2 ml intramuscularly. Nursing lambs and ewes remained together until the lambs reached two months of age, at which time they were separated from their mothers and weaned. Ewes were removed from the premises, and weaned lambs remained in the same outdoor covered pens for the rest of the study. At weaning, lambs received moxidectin (Cydectin® Oral Drench for Sheep 0.1%, 1 mg/ml, Boehringer Ingelheim, St. Joseph, MO) 0.2 ml/kg body weight orally, amprolium (Corid® 9.6% Oral Solution, Merial, Duluth, GA) 0.5 ml/kg orally once daily for 10 days, and vitamin B1 (Thiamine Hydrochloride, 500 mg/ml, Rafter 8 Products, Calgary, Alberta, Canada) 1.5 ml subcutaneously once daily every third day for a total of four treatments. Weaned lambs were fed a "complete" ration (Ringmaster Start-To-Finish Show Lamb Pellets, Nutrena, Minneapolis, MN) designed to meet 100% NRC requirements as calculated by ARIES (software version 2007, University of California, Davis) and had free access to drinking water. At six months of age, lambs were euthanized using sodium pentobarbital (Beuthanasia®, Intervet/Schering-Plough Animal Health, Summit, NJ) 75 mg/kg intravenously. Computed tomography (CT) imaging was performed immediately after euthanasia.

II.3.2 Treatment groups

Ewes (n=36) were randomly assigned to one of four treatments - normal control (NC) group (n = 8 ewes), the saline control (SC) group (n = 8 ewes), the binge alcohol (BA; 1.75 g/kg) group (n = 8 ewes), and the heavy binge alcohol (HBA; 2.5 g/kg) group (n = 12 ewes). An intravenous catheter (16 ga., 5.25 inch Angiocath™; Becton Dickinson, Sandy, UT) was placed into the jugular vein of each ewe (except for the NC group) on GD 4. Beginning on this day, alcohol (2.5 or 1.75 g/kg body weight) or saline was administered intravenously over a 1-hour period via a pump (VetFlo® 7701B IV Vet Infusion Pump, Grady Medical, Temecula, CA). The alcohol solution was prepared by adding 95% ethanol to sterile 0.9% saline to achieve a 40% w/v alcohol solution. Solutions were prepared under aseptic conditions and were passed through a 0.2 μm bacteriostatic filter. The saline control group received an infusion of isotonic saline (0.9%) that was equal in volume to the alcohol infusions. Infusions were administered on three consecutive days per week from GD 4-41, followed by four days without treatment (18 treatments total). Lambs produced from ewes in the four treatment groups that entered the imaging study included 8 NC lambs (1 female, 7 males), 8 SC lambs (4 females, 4 males), 8 BA lambs (6 females, 2 males), and 12 HBA lambs (6 females, 6 males).

II.3.3 Maternal blood alcohol concentration

Blood was drawn from the jugular vein of each ewe one hour after alcohol infusions began to measure peak BAC as previously described [128]. A 20 µl aliquot of blood was collected in a microcapillary tube and transferred into a vial containing 0.6 N perchloric acid and 4 mM n-propyl alcohol (internal standard) in distilled water. The vial was tightly capped with a septum-sealed lid and stored at room temperature until analysis by headspace gas chromatography (Varian Associates model 3900, Palo Alto, CA) at least 24 h after collection.

II.3.4 Computed tomography imaging

Images were acquired on a computed tomography (CT) scanner (Biograph mCT®, Siemens Medical, USA) that operated at 120 kVp and 300 mA maximum cube current. In the standard mode of operation, the distance from the detector to the source was 1.0856e+003 mm and source to subject distance was 595 mm. The data collection diameter of the scan field of view (SFOV) was 500 mm, and the reconstruction diameter of the display field of view (DFOV) was 300 mm. The matrix was 512 x 512, pixel size was 0.59 mm, slice thickness was 1 mm, and voxel volume was 0.348 mm^3. The image acquisition was performed on animals immediately after euthanasia. Before animal scanning, daily system calibration was performed for accuracy. Long-term scanner maintenance was performed in compliance with the operating manual (Siemens Biograph mCT ® versions VG10A, VG21A, VG30A, VG40A, chapters 7 and 12).

II.3.5 Image analysis

Amira Software (Visage Imaging, Inc., San Diego, CA) was used for bone segmentation and acquisition of skull measurements and craniofacial measurements. After three-dimensional (3D) reconstruction of the head scan, bony tissues were segmented (identified) as previously described [126]. A threshold of 160 HU (Hounsfield Units) was used to complete all bony tissue segmentations and skull measurements, and -350 HU was used for soft tissue facial measurements. Amira Software to visualize soft tissue structures and underlying craniofacial bones and then manually extracted a total of 29 measurements: 1) nine 2D skull craniofacial measurements (distance, mm): upper facial depth, lower facial depth, orbital height and width, minimal frontal width, bitragal width, bigonial width, interorbital distance, and nasal length (Table I and Figure I); 2) ten 2D craniofacial soft-tissue measurements (distance, mm): nasal width, nasal length, nasal bridge length, philtrum length, lower facial height, mid-facial depth, lower facial depth, palpebral fissure length, inner canthal width, and outer canthal width (Table I and Figure II); 3) eight 3D individual skull bone volumes plus total skull bone volume (volume; mm^3): mandible, frontal, parietal, occipital, maxilla, nasal, lacrimal, and jugal bones (Figure III), with total skull the sum of all eight; and 4) 2D cranial circumference (distance, mm). Though cranial circumference was obtained as part of the skull distance measures

Table I. Craniofacial measurements and landmarks

Figure	Location	Number	Measurement
1	Skull	1	Upper facial depth[a]
		2	Lower facial depth[a]
		3	Cranial circumference
		4	Orbital height[a]
		5	Orbital width[a]
		6	Minimal frontal width
		7	Bitragal width
		8	Bigonial width
		9	Interorbital distance
		10	Nasal length
2	Face	11	Nasal width
		12	Nasal length
		13	Nasal bridge length
		14	Philtrum length
		15	Lower facial height
		16	Mid-facial depth[a]
		17	Lower facial depth[a]
		18	Palpebral fissure length[a]
		19	Inner canthal width
		20	Outer canthal width

Numbers are keyed to Figures 1 and 2.

[a] Both right and left side measurements were taken.

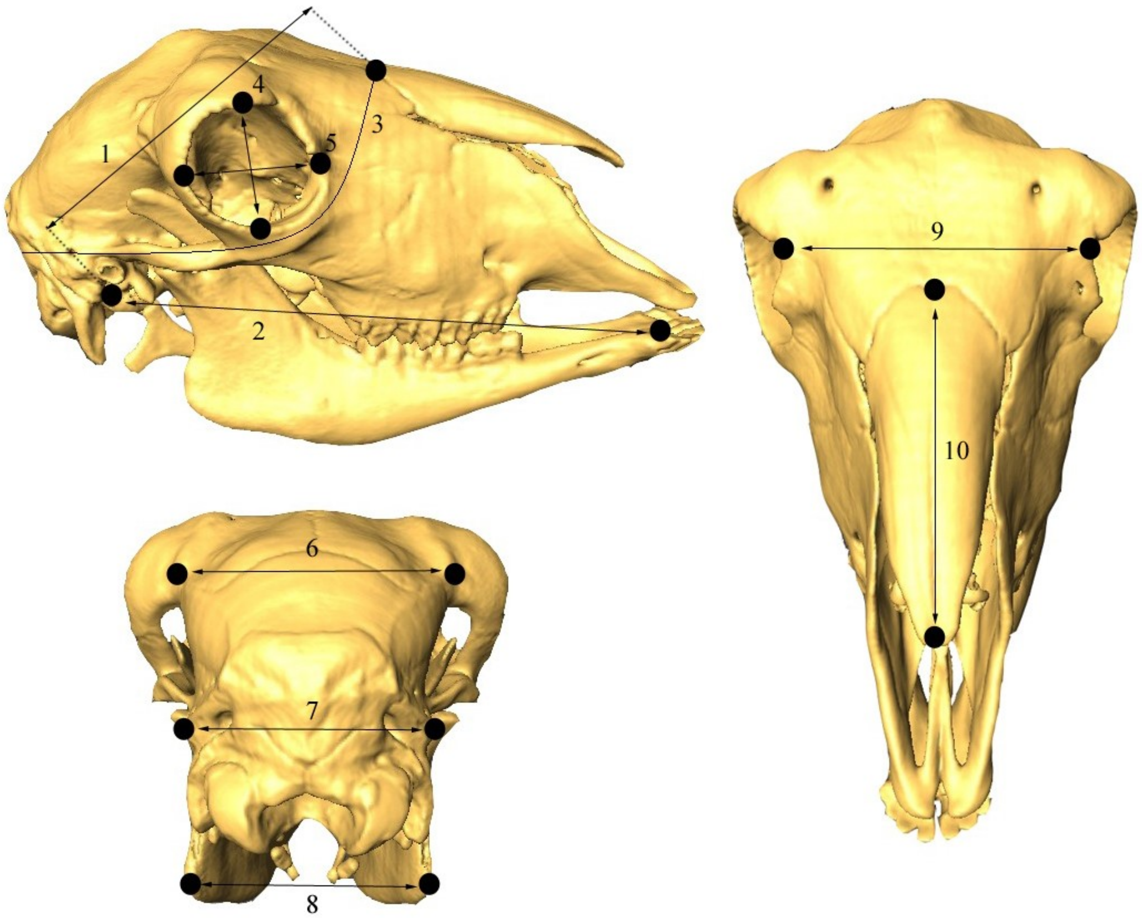

Figure I. Normal control lamb skull. Lateral, caudal, and dorsal 3D aspects of the skull shown as visualized with Amira Software (Visage Imaging, Inc., San Diego). The 10 skull linear measurements obtained from each of the lamb skulls are shown as identified in Table I.

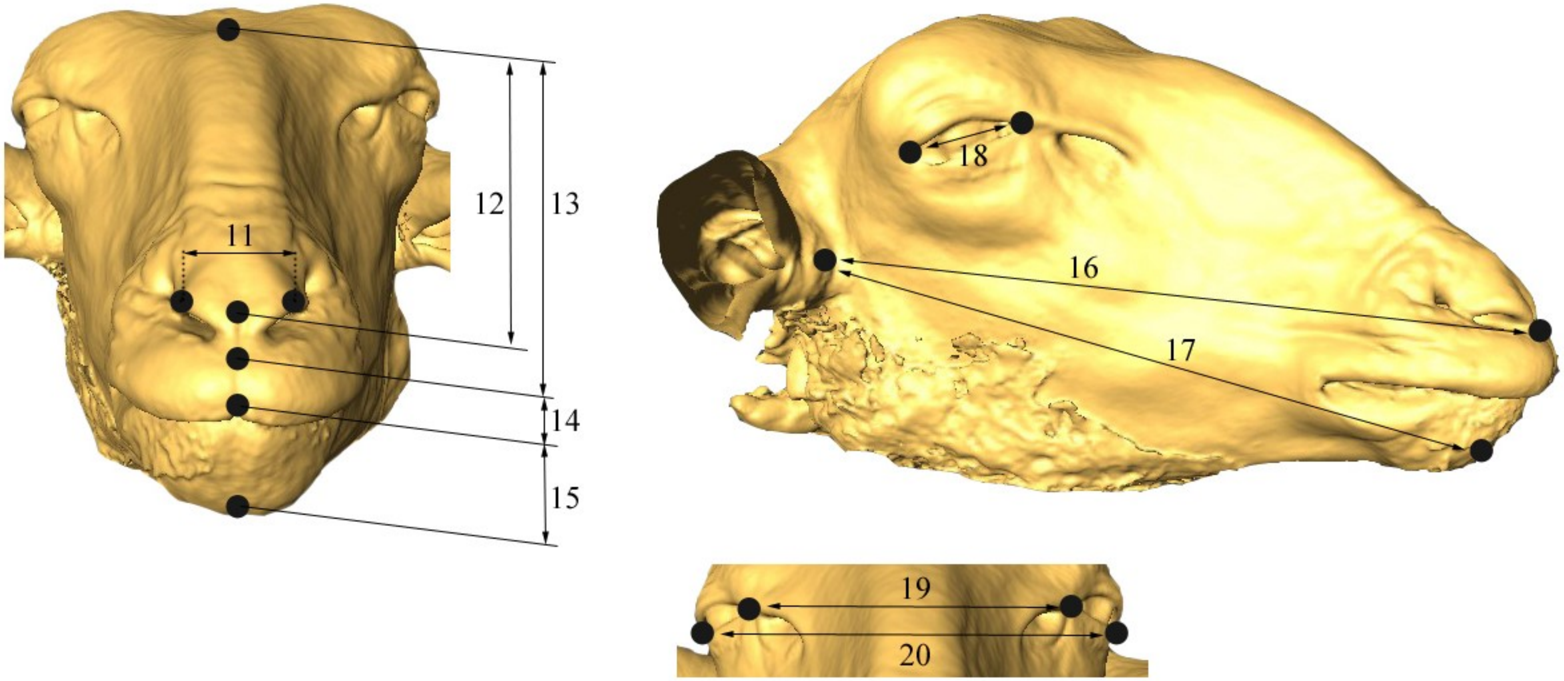

Figure II. Normal control lamb face. Rostral and lateral 3D aspects shown of the lamb face as visualized with Amira Software (Visage Imaging, Inc., San Diego). The 10 face linear measurements obtained from each lamb are shown as identified in Table I. The ears have been cropped from the image.

in the lambs, it was separated from the craniofacial measures for the purposes of initial analyses. This was done because head circumference is typically obtained separately from the dysmorphology exam in clinical settings as part of the diagnostic measures to identify children with FAS, and it is interpreted separately from facial dysmorphology [129]. All measurements were taken by one of the authors (SMB) who was blinded to the treatment groups. To decrease measurement error, each measurement was repeated in triplicate with subsequent measures taken only if the first three measurements differed by >2mm. In instances in which >3 measurements were taken, outliers >2mm were not used. The nineteen 2D craniofacial measurements and the cranial circumference measurement were acquired utilizing a measurement tool in Amira. The eight bones of the skull were manually segmented, and their volumes were calculated based on the segmentation results. For the bilateral linear measurements of the face and skull, preliminary analyses indicated there were no significant differences between the left and right sides, so only the left side of all bilateral measurements of the face and skull were used for subsequent analyses. Total skull bone volume was calculated by adding all of the individual bone segmentations together (left and right sides where applicable). Ear measurements were not taken because the ears were inadvertently cropped in the CT output file.

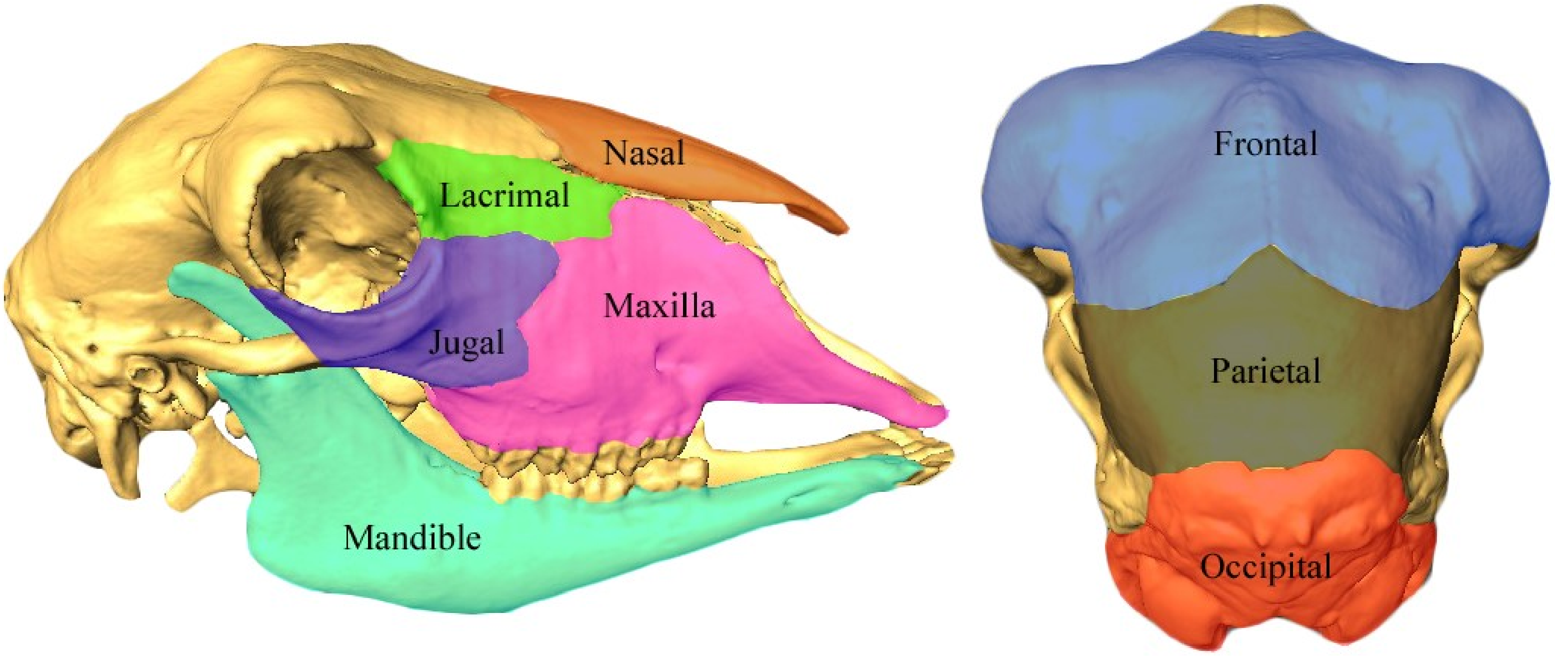

Figure III. Segmented normal control lamb skull. Lateral and caudal 3D aspects shown of a normal lamb skull as visualized with Amira Software (Visage Imaging, Inc., San Diego). The 8 bones segmented for bone volumes on each lamb skull are shown. In the lateral view, only the right sided segmentation is visible. Total skull bone volume was calculated by adding together the volume of all of the bone segmentations (left and right sides).

II.3.6 Statistical analysis

Given the unequal numbers of males and females in the NC and BA groups and the low number of lambs of each sex across treatment groups overall, the power to detect potential sex differences was very limited. The data was first screened for potential differences between males and females. This was to determine whether the male and female data could be combined within groups for the purposes of statistical analysis without confounding the analysis of prenatal treatment. The NC group had only one female and the BA group had only two males. The within-group ranking of the data of those subjects was determined and each fell within the range of the majority sex of the group. Therefore, the individual data did not skew the within-group distribution for any measure for either the NC or BA groups. For the two groups with equal numbers of males and females (SC and HBA), a two-way analyses of variance (ANOVA) with sex and treatment as grouping factors was calculated. None of the measures showed a significant main or interactive effect of sex, so the data of males and females were combined within groups for subsequent analyses of variance.

Treatment effects on measurements of skull bone volumes, skull distances, face distances, and cranial circumference were first analyzed with one-way between-subjects ANOVA using Bonferroni-corrected alpha levels to set the significance level within each set of data. Thus, for the nine skull bone volumes and nine skull distance measures, a Bonferroni-corrected alpha level of 0.0056 (= 0.05/9) was used for the nine univariate ANOVAs. For the ten face distance measures, the Bonferroni-corrected alpha level was 0.005 (= 0.05/10). For cranial circumference, the alpha level was 0.05. Measures that met the Bonferroni-corrected alpha level on the univariate test were then analyzed using pairwise comparisons among the four treatments within each measure, and the multiple comparisons were corrected by the Holm-Sidak method ($p < 0.05$). In addition, two different one-way between-subjects analyses of covariance (ANCOVA) were calculated for individual skull bone volumes. The first included covaried total skull bone volume and sex, while the second were covaried cranial circumference and sex. Separate ANCOVAs were also calculated for the facial and skull bone linear distances, covarying for cranial circumference and sex. The main purpose of these covariance analyses was to determine the extent to which individual skull bone volumes (or craniofacial linear measures) could provide quantitative evidence of the effects of binge alcohol treatment beyond that which might be associated with reduced head size, as well as to control for any influences of sex differences. This approach follows a publication that assessed similar measures in a prenatal mouse model [126]. To determine whether total bone volume provides a better identification of alcohol-exposed lambs than cranial circumference (akin to head circumference in FAS screening), the 10th percentile was calculated for each measure. Each distribution, total skull bone volume and cranial circumference, from the NC and SC groups (not significantly different) was combined to form control distributions for each measure. Lambs in the BA and HBA groups were then classified based on whether or not they were $\leq$ 10th percentile of the control distribution for each measure (similar to the FAS screening cutoff). The relative sensitivity of the two measures was determined by comparing the number of lambs in the 10th percentile of the two measures using Fisher's Exact Test.

II.3.7 Discriminant analysis

Univariate discriminant analyses of the craniofacial bone measures were examined for six pairwise comparisons: NC vs. HBA, NC vs. BA, NC vs. SC, SC vs. BA, SC vs. HBA, and BA vs. HBA. Univariate Receiver Operating Characteristic (ROC) analysis was implemented using Matlab (The MathWorks, Inc., Natick, MA) and was performed on each of the following measures: 1) nine skull volume measures, 2) nine skull distance measures, and 3) ten face distance measures; cranial circumference was included in each of the three data sets. Area under the ROC curve (AUC) was reported. The best overall classification accuracy for percent of all animals correctly classified on the ROC curve, its corresponding sensitivity for percent of cases correctly classified, and its corresponding specificity for percent of controls correctly classified, were also reported in each comparison.

II.4 Results

II.4.1 Maternal blood alcohol concentration

The mean ± SEM maternal BACs at the end of alcohol infusion (1 hour; point in time at which BACs are known to peak) were significantly higher in the HBA treatment (280.0 ± 9.7 mg/dl) compared to the BA treatment (198.9 ± 8.6 mg/dl) ($p = 0.001$).

II.4.2 Fetal and six-month-old body weights

There were no significant differences between groups with regard to fetal birth weight (NC, 5.71 ± 0.35 kg; SC, 5.74 ± 0.33 kg; BA, 5.13 ± 0.49 kg; HBA, 4.68 ± 0.31 kg) and six-month-old body weight (NC, 36.59 ± 4.33 kg; SC, 38.72 ± 4.04 kg; BA, 34.09 ± 2.25 kg; HBA, 33.02 ± 1.71 kg).

II.4.3 Correlations among measures

As expected, Pearson correlations among all nine skull volume measures and the cranial circumference were strongly positive (Table II), and all were statistically significant ($p < 0.001$). The correlation coefficients ranged from r = 0.640, between the nasal and parietal bones, to r = 0.955 between total skull bone volume and frontal bone. Each of the bone volumes were highly correlated with cranial circumference (r = 0.716 to 0.939).

Pearson correlations among the nine skull distance measurements and cranial circumference were all positive (Table III), and 53% were statistically significant ($p < 0.001$). The significant correlations ranged from r = 0.530, between the interorbital distance and orbital height, to r = 0.897 between the bitragal width and cranial circumference. Notably, all of the skull distance measures except orbital width and skull nasal length were significantly correlated with cranial circumference (r = 0.579 to 0.897). Orbital width did not correlate significantly with any of the other skull measures and skull nasal length significantly correlated with only one skull measure (lower facial depth).

Pearson correlations among ten facial measurements and the cranial circumference were all positive and 43.6% were statistically significant (Table IV). The significant correlation coefficients ($p < 0.001$) ranged from r = 0.460, between the outer canthal width and lower facial depth, to r = 0.977 between the nasal bridge length and facial nasal length. All of the facial distance measures except the lower facial height and palpebral fissure length were significantly correlated with the cranial circumference (r = 0.579 to 0.897). Orbital width did not correlate significantly with any of the other skull measures and skull nasal length significantly correlated with only one skull measure (lower facial depth).

Table II. Pearson correlation coefficients among the nine volumetric skull measures and the cranial circumference measure

	Occipital	Parietal	Frontal	Nasal	Lacrimal	Jugal	Maxilla	Mandible	Total Skull	Cranial Circ.
Occipital	**1.000**	**0.892**	**0.828**	**0.729**	**0.775**	**0.850**	**0.874**	**0.821**	**0.931**	**0.847**
Parietal	**0.892**	**1.000**	**0.850**	**0.640**	**0.799**	**0.817**	**0.849**	**0.794**	**0.912**	**0.821**
Frontal	**0.828**	**0.850**	**1.000**	**0.804**	**0.843**	**0.916**	**0.871**	**0.836**	**0.955**	**0.918**
Nasal	**0.729**	**0.640**	**0.804**	**1.000**	**0.693**	**0.778**	**0.771**	**0.686**	**0.811**	**0.801**
Lacrimal	**0.775**	**0.799**	**0.843**	**0.693**	**1.000**	**0.785**	**0.798**	**0.650**	**0.838**	**0.716**
Jugal	**0.850**	**0.817**	**0.916**	**0.778**	**0.785**	**1.000**	**0.904**	**0.894**	**0.952**	**0.928**
Maxilla	**0.874**	**0.849**	**0.871**	**0.771**	**0.798**	**0.904**	**1.000**	**0.839**	**0.950**	**0.882**
Mandible	**0.821**	**0.794**	**0.836**	**0.686**	**0.650**	**0.894**	**0.839**	**1.000**	**0.915**	**0.869**
Total Skull	**0.931**	**0.912**	**0.955**	**0.811**	**0.838**	**0.952**	**0.950**	**0.915**	**1.000**	**0.939**
Cranial Circ.	**0.847**	**0.821**	**0.918**	**0.801**	**0.716**	**0.928**	**0.882**	**0.869**	**0.939**	**1.000**

All correlations are in bold, indicating correlations are significant at $p < 0.001$ for all measures

Pearson correlations among ten facial measurements and the cranial circumference were all positive and 43.6% were statistically significant (Table IV). The significant correlation coefficients ($p < 0.001$) ranged from r = 0.460, between the outer canthal width and lower facial depth, to r = 0.977 between the nasal bridge length and facial nasal length. All of the facial distance measures except the lower facial height and palpebral fissure length were significantly correlated with the cranial circumference (r = 0.543 to 0.837). Palpebral fissure length did not correlate significantly with any of the other facial measures.

Pearson correlations between the ten facial distance measures and the nine underlying skull distance measures resulted in 29 positive correlations ($p < 0.001$) out of 90 (32%, Table V). A majority of these 29 reflected common structural features between facial landmarks and underlying skull structures (e.g., lower facial depth in the face correlated with the same measure in bone; inner and outer canthal widths in facial measures correlated with bone measures of minimal frontal width, bitragal width, bigonial width, and interorbital distance; facial nasal length correlated with bone lower facial depth, etc.). Mid-facial depth (akin to the “flattened mid-face” of FAS) significantly correlated with six of the nine bone distance measures. Palpebral fissure length and philtrum length are two facial measures most directly comparable to measures used in FAS dysmorphology evaluations. Palpebral fissure length was not significantly correlated with any underlying bone measure and philtrum length was significantly correlated only with orbital height.

Table III. Pearson correlation coefficients among the nine skull distance measures and the cranial circumference

	Upper Facial Depth	Lower Facial Depth	Orbital Height	Orbital Width	Minimal Frontal Width	Bitragal Width	Bigonial Width	Interorbital Distance	Skull Nasal Length	Cranial Circ.
Upper Facial Depth	**1.000**	**0.721**	**0.569**	0.259	**0.546**	**0.730**	0.323	**0.606**	0.110	**0.823**
Lower Facial Depth	**0.721**	**1.000**	**0.665**	0.256	0.468	**0.677**	0.513	**0.569**	**0.595**	**0.812**
Orbital Height	**0.569**	**0.665**	**1.000**	0.469	0.217	**0.531**	**0.583**	**0.530**	0.433	**0.605**
Orbital Width	0.259	0.256	0.469	**1.000**	0.374	0.496	0.246	0.402	0.046	0.462
Minimal Frontal Width	**0.546**	0.468	0.217	0.374	**1.000**	**0.681**	0.429	**0.581**	0.157	**0.754**
Bitragal Width	**0.730**	**0.677**	**0.531**	0.496	**0.681**	**1.000**	**0.566**	**0.783**	0.178	**0.897**
Bigonial Width	0.323	0.513	**0.583**	0.246	0.429	**0.566**	**1.000**	**0.623**	0.414	**0.579**
Interorbital Distance	**0.606**	**0.569**	**0.530**	0.402	**0.581**	**0.783**	**0.623**	**1.000**	0.286	**0.780**
Skull Nasal Length	0.110	**0.595**	0.433	0.046	0.157	0.178	0.414	0.286	**1.000**	0.382
Cranial Circ.	**0.823**	**0.812**	**0.605**	0.462	**0.754**	**0.897**	**0.579**	**0.780**	0.382	**1.000**

Correlations in bold are significant at $p < 0.001$

Table IV. Pearson correlation coefficients among the ten face distance measures and the cranial circumference

	Nasal Width	Facial Nasal Length	Nasal Bridge Length	Philtrum Length	Lower Facial Height	Mid-Facial Depth	Lower Facial Depth	Palpebral Fissure Length	Inner Canthal Width	Outer Canthal Width	Cranial Circ.
Nasal Width	**1.000**	**0.631**	**0.576**	**0.634**	0.517	**0.717**	0.502	0.318	**0.606**	0.463	**0.728**
Facial Nasal Length	**0.631**	**1.000**	**0.977**	0.404	0.247	**0.817**	**0.527**	0.0583	0.488	0.259	**0.582**
Nasal Bridge Length	**0.576**	**0.977**	**1.000**	0.396	0.197	**0.767**	0.497	-0.0136	0.490	0.251	**0.544**
Philtrum Length	**0.634**	0.404	0.396	**1.000**	**0.624**	0.506	0.337	0.241	**0.554**	**0.547**	**0.543**
Lower Facial Height	0.517	0.247	0.197	**0.624**	**1.000**	0.413	0.0809	0.325	0.378	0.364	0.382
Mid-Facial Depth	**0.717**	**0.817**	**0.767**	0.506	0.413	**1.000**	**0.758**	0.199	**0.643**	0.463	**0.822**
Lower Facial Depth	0.502	**0.527**	0.497	0.337	0.0809	**0.758**	**1.000**	0.141	**0.579**	0.460	**0.754**
Palpebral Fissure Length	0.318	0.0583	-0.0136	0.241	0.325	0.199	0.141	**1.000**	0.144	0.288	0.222
Inner Canthal Width	**0.606**	0.488	0.490	**0.554**	0.378	**0.643**	**0.579**	0.144	**1.000**	**0.836**	**0.837**
Outer Canthal Width	0.463	0.259	0.251	**0.547**	0.364	0.463	0.460	0.288	**0.836**	**1.000**	**0.724**
Cranial Circ.	**0.728**	**0.582**	**0.544**	**0.543**	0.382	**0.822**	**0.754**	0.222	**0.837**	**0.724**	**1.000**

Correlations in bold are significant at $p < 0.001$

Table V. Pearson correlation coefficients among the ten face distance measures and the nine skull distance measures

	Nasal Width	Face Nasal Length	Nasal Bridge Length	Philtrum Length	Lower Facial Height	Mid-Facial Depth	Lower Facial Depth	Palpebral Fissure Length	Inner Canthal Width	Outer Canthal Width
Upper Facial Depth	**0.534**	0.320	0.311	0.523	0.357	**0.745**	**0.668**	0.213	**0.660**	**0.556**
Lower Facial Depth	**0.674**	**0.760**	**0.697**	0.505	0.288	**0.952**	**0.812**	0.117	**0.617**	0.510
Orbital Height	0.507	0.467	0.483	**0.537**	0.293	0.494	0.385	0.380	0.512	0.446
Orbital Width	0.314	0.062	0.078	0.377	0.197	0.322	0.484	0.465	0.483	0.517
Minimal Frontal Width	0.295	0.288	0.274	0.305	0.210	**0.532**	0.523	-0.013	**0.705**	**0.673**
Bitragal Width	**0.605**	0.379	0.317	0.478	0.330	**0.687**	**0.594**	0.191	**0.761**	**0.753**
Bigonial Width	0.494	0.495	0.488	0.445	0.244	0.482	0.240	0.075	**0.675**	**0.691**
Interorbital Distance	**0.533**	0.418	0.430	0.409	0.143	**0.588**	0.507	0.059	**0.813**	**0.694**
Skull Nasal Length	0.467	**0.919**	**0.920**	0.322	0.247	**0.808**	0.437	0.071	0.349	0.126

Correlations in bold are significant at $p < 0.001$

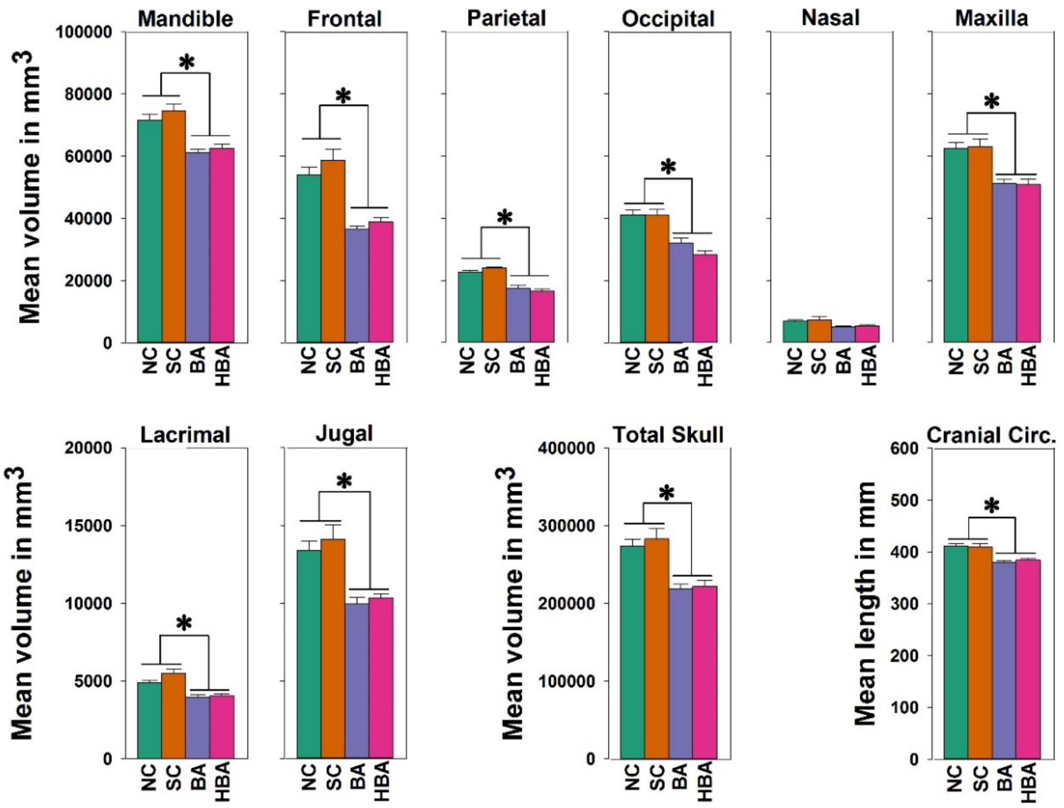

Figure IV. Treatment effects on nine volumetric skull measures and the cranial circumference measures. The y axis indicates the mean volume (± SEM) in mm^3 for the eight segmented bone volumes and total skull volume, or length (in mm) for cranial circumference. Note the scale for the six bones in the top panels (maximum of 100,000 mm^3) differs from that in the lower panels for the lacrimal and jugal bones (maximum of 20,000 mm^3). For the bone volumes, the ANOVA α level was adjusted to 0.0056 (=0.05/9) for the nine ANOVAs performed, followed by the Holm-Sidak method for pairwise comparisons ($p < 0.05$). For cranial circumference, the ANOVA α level was 0.05 followed by the Holm-Sidak method for pairwise comparisons ($p < 0.05$). Significant group differences are indicated within each panel. An asterisk (*) indicates that the volumes of two control groups (NC and SC) were significantly greater than the two alcohol-exposed groups (BA and HBA); NC and SC did not differ from each other, and BA and HBA did not differ from each other.

II.4.4 Skull bone volumes and cranial circumference

As shown in Figure IV, significant effects of prenatal treatment were evident in eight of the nine volumetric skull measures (Bonferroni-corrected $\alpha = 0.0056$) and in the cranial circumference measure ($p < 0.05$). Bones with significant treatment effects included the mandible (F (3, 35) = 15.988, $p < 0.001$), frontal (F (3, 35) = 24.906, $p < 0.001$), parietal (F (3, 35) = 26.724, $p < 0.001$), occipital (F (3, 35) = 18.285, $p < 0.001$), maxilla (F (3, 35) = 12.850, $p < 0.001$), lacrimal (F (3, 35) = 16.894, $p < 0.001$), jugal (F (3, 35) = 14.740, $p < 0.001$), total skull bone volume (F (3, 35) = 23.944, $p < 0.001$), and cranial circumference (F (3, 35) = 15.089, $p < 0.001$). Pairwise group comparisons (Holm-Sidak $p < 0.05$) confirmed that the bone volumes of the HBA and BA groups were significantly reduced relative to the NC and SC groups for all skull bones except the nasal bone, the total skull bone volume, and the cranial circumference. There were no significant differences between the BA and HBA groups, or between the NC and the SC groups.

Covariance analyses using either total skull bone volume or cranial circumference and sex as covariates were used to assess alcohol treatment effects on individual skull bone volumes. This was done to determine if the individual bone volumes would remain significant after the effects of head size or total skull bone volume and sex differences were removed. After covarying for total skull bone volume and sex, treatment effects on volumetric skull measures were no longer significant (Bonferroni-corrected $\alpha = 0.00625$). This was consistent with the strong correlations between total skull bone volume and the volume of each individual bone. After covarying for cranial circumference and sex, significant effects among the four treatment groups were found in four of the nine volumetric skull measures (Bonferroni-corrected $\alpha = 0.0056$; Figure V). These included the frontal, parietal, and occipital bones, as well as the total skull bone volumes. Pairwise comparisons (Holm-Sidak $p < 0.05$) showed the HBA treatment differed from both NC and SC groups for the parietal and occipital bones. The occipital bone was the only bone volume measure to show a significantly greater reduction in the HBA treatment compared to the BA treatment, suggesting a dose-dependent effect. Thus, when variance associated with cranial circumference (and sex) was statistically controlled, the parietal and occipital bones still distinguished the HBA group from the NC and SC groups.

II.4.5 Craniofacial distance measures

Significant treatment effects were evident in five of the nine skull distance measures (Bonferroni-corrected $\alpha = 0.0056$; Figure VI), including the upper facial depth ($F(3, 35) = 8.997$, $p < 0.001$), bitragal width ($F(3, 35) = 10.949$, $p < 0.001$), interorbital distance ($F(3, 35) = 7.806$, $p < 0.001$), and nasal length ($F(3, 35) = 5.575$, $p < 0.001$). Holm-Sidak pairwise group comparisons showed significant differences ($p < 0.05$) between the BA and HBA groups and the NC and SC groups for upper facial depth, bitragal width, and interorbital distance. No significant differences were found between the BA and HBA groups, or between the NC and SC groups in these three skull distance measures. Bigonial width showed differences between the HBA and SC groups, but HBA did not differ significantly from NC. Nasal length showed differences between the BA and HBA groups, but neither of those was significantly different from either the NC or SC groups.

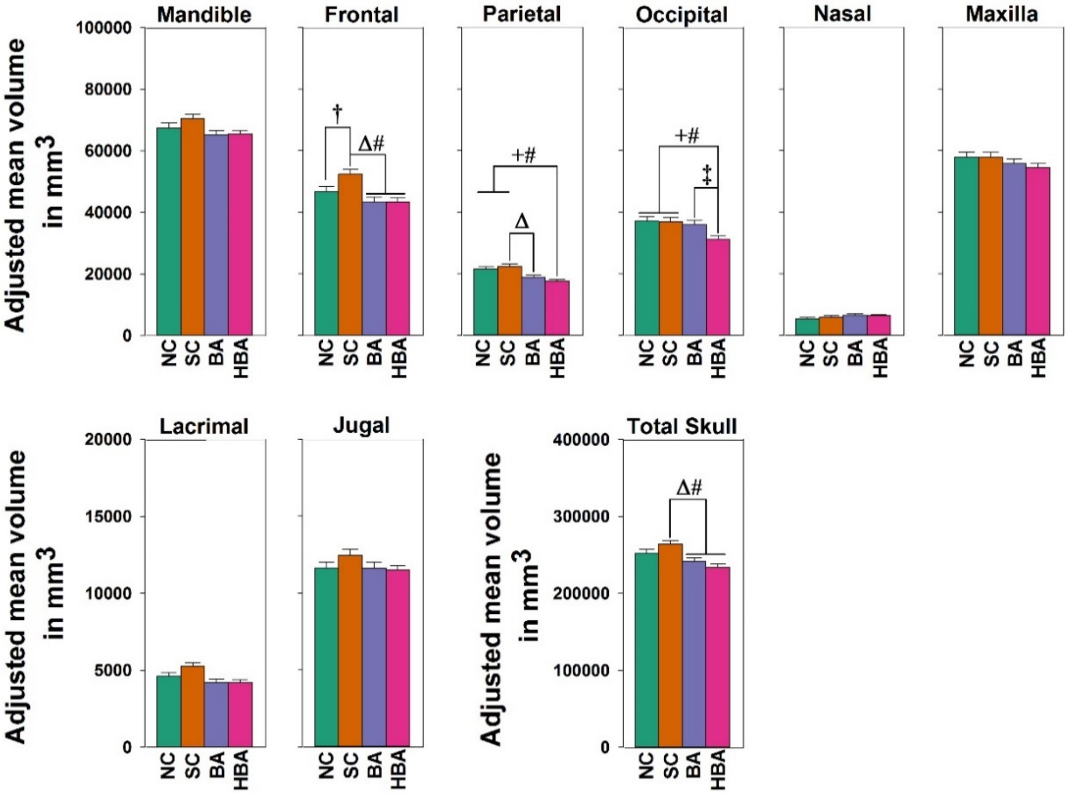

Figure V. Treatment effects on nine volumetric skull measures while controlling for cranial circumference and sex, showing the adjusted group means (± SEM) after removal of the influence of the two covariates. The y axis indicates the adjusted volume in mm^3 for the nine measures (note scale differences between the top and bottom panels). For bone volumes, the ANOVA α level was adjusted to 0.0056 (=0.05/9) for the nine ANOVAs performed, followed by the Holm-Sidak method for pairwise comparisons ($p < 0.05$). For cranial circumference, the ANOVA α level was 0.05 followed by the Holm-Sidak method for pairwise comparisons ($p < 0.05$). Significant group differences are indicated within each panel. Note that after controlling for effects of differences in cranial circumference, the effects of the heavy binge alcohol (HBA) treatment relative to controls were still detectable in the parietal and occipital bone volumes, and the HBA even differed from the BA group in the occipital bone volume. Significance between NC vs SC is indicated with a dagger sign (†), BA vs SC is indicated with a delta sign (Δ), HBA vs SC is indicated with a pound sign (#), HBA vs NC is indicated with a plus sign (+), and HBA vs BA is indicated with a double dagger sign (‡).

For the facial distance measures, significant treatment effects were found in five of the ten measures (Bonferroni-corrected α = 0.005; Figure VII), including the philtrum length (F (3, 35) = 5.244, $p < 0.001$), mid-facial depth (F (3, 35) = 6.946, $p < 0.001$), lower facial depth (F (3, 35) = 5.195, $p < 0.001$), inner canthal width (F (3, 35) = 15.097, $p < 0.001$), and outer canthal width (F (3, 35) = 6.618, $p < 0.001$). However, follow-up Holm-Sidak pairwise group comparisons for these five measures indicated that only the inner canthal width showed significant reductions ($p < 0.05$) in both alcohol-exposed groups compared to the two control groups. None of the other measures showed significant differences between the alcohol-exposed and both control groups. Covariance analyses were performed to evaluate the effects of cranial circumference and sex on the nine skull distance measures (Bonferroni-corrected α = 0.0056) and the ten face distance measures (Bonferroni-corrected α = 0.005). None of the skull or face measures remained significant between the alcohol-exposed groups and the control groups.

II.4.6 Discriminant analysis

Area under ROC curve (AUC) results from the univariate ROC analyses are shown in Table VI, VII, and VIII. Several bone volumetric measures were identified as best predictors in classifying between alcohol-exposed groups and control groups across the ROC analysis of the six treatment pairs (Table VI). The mandible, frontal bone, parietal bone, and total skull bone volumes achieved an AUC of 0.99-1.0, with the best overall accuracy of 100% (sensitivity 100%, specificity 100%). The occipital bone provided the best discrimination between the BA and HBA groups (AUC = 0.708; accuracy of 75%, sensitivity and specificity of 75%). For the skull distance measures (Table VII), the

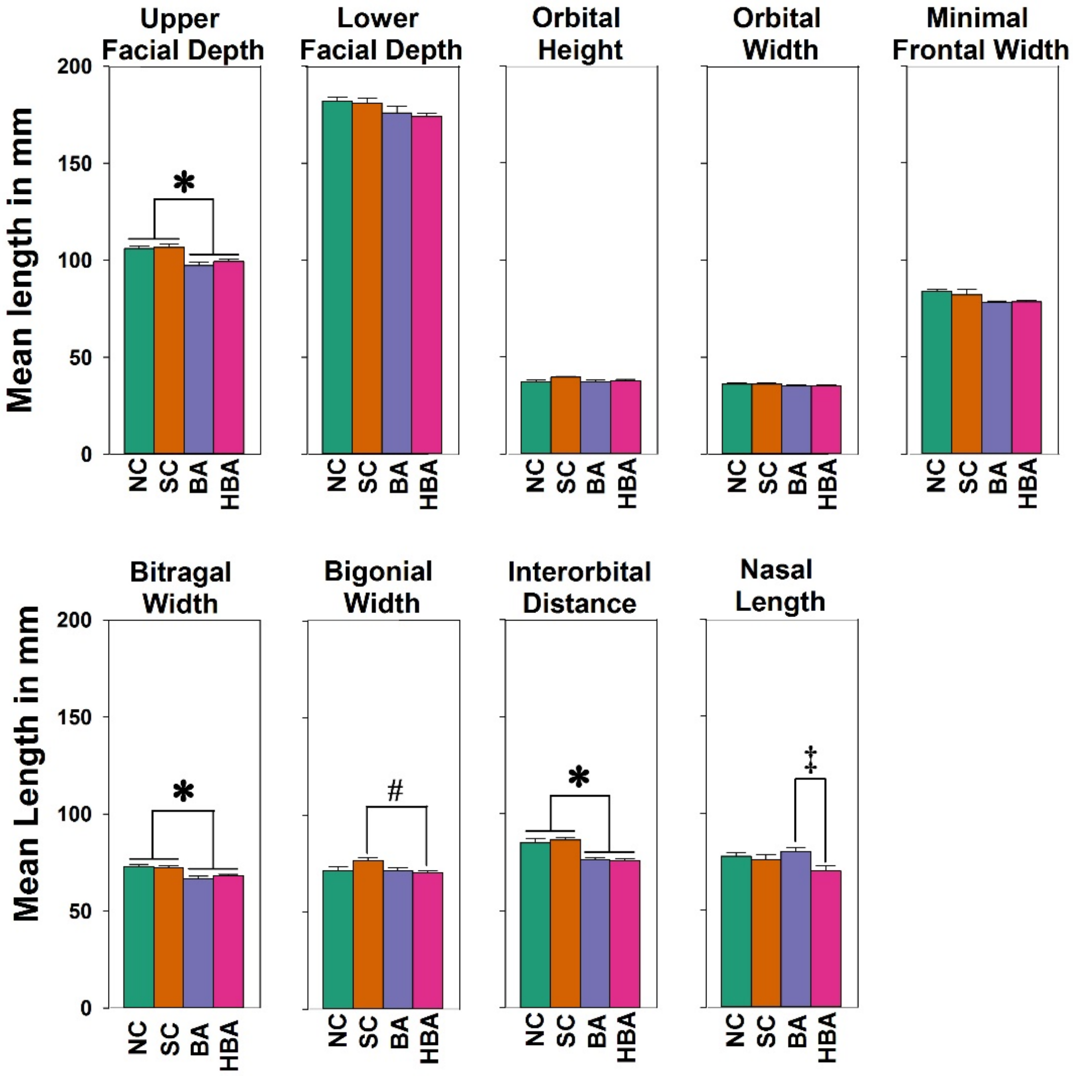

Figure VI. Treatment effects on nine skull distance measures. The y axis indicates the mean length (± SEM) in mm. The ANOVA α level was adjusted to 0.0056 (=0.05/9) for the nine ANOVAs performed, followed by the Holm-Sidak method for pairwise comparisons ($p < 0.05$). Significant group differences are indicated within each panel. An asterisk (*) indicates significance between the following four pairs: BA vs NC; HBA vs NC; BA vs SC; and HBA vs SC. Significance between HBA vs SC is indicated with a pound sign (#) and significance between HBA vs BA is indicated with a double dagger sign (‡).

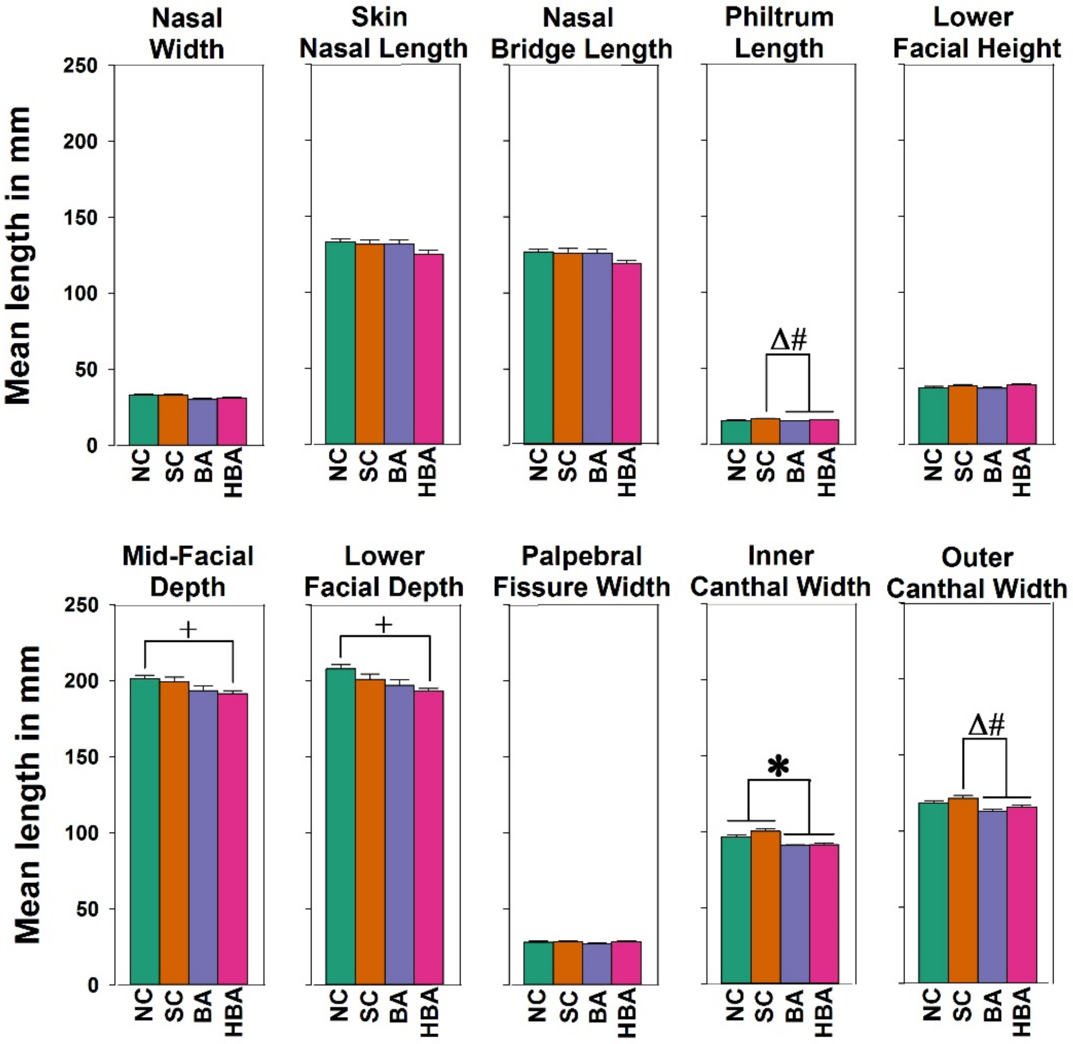

Figure VII. Treatment effects on ten face measures. The y axis indicates the mean length (± SEM) in mm. The ANOVA α level was adjusted to 0.005 (=0.05/10) for the ten ANOVAs performed, followed by the Holm-Sidak method for pairwise comparisons (*p* < 0.05). Significant group differences are indicated within each panel. An asterisk (*) indicates significance between the following four pairs: BA vs NC; HBA vs NC; BA vs SC; and HBA vs SC. Significance between BA vs SC is indicated with delta sign (Δ), HBA vs SC is indicated with a pound sign (#), and HBA vs NC is indicated with a plus sign (+).

interorbital distance was the best predictor in distinguishing between an alcohol and control treatment (AUC between 0.984-1.0) with overall accuracies between 93.8-100% (sensitivities between 87.5-100%, specificities of 100%). For the facial soft-tissue measures (Table VIII), the inner canthal width was the best predictor in distinguishing between an alcohol and control treatment. The AUC ranged between 0.906-1.0, and accuracies between 90-100% (sensitivities 87.5-100%, specificities 75-100%). The cranial circumference was the next best predictor in distinguishing between an alcohol and control treatment, with AUC ranging between 0.875-0.984, and accuracies between 93.8-95% (sensitivities 87.5-100%, specificities 87.5-100%). Of the skull and facial distance measures, the best predictors to classify between the BA and HBA groups were the skull nasal length (AUC 0.802; overall accuracy of 75%; sensitivity 58.3% and specificity 100%) and nasal bridge length (AUC 0.781; overall accuracy of 75%; sensitivity 83.3% and specificity 62.5%).

II.4.7 Relative sensitivity of total skull bone volume and cranial circumference

From the discriminant analysis (above and Table VI), total skull bone volume was 100% accurate in classifying alcohol-exposed and control lambs, more accurate than the cranial circumference (with which it was highly correlated, r = 0.939). The effect size of the alcohol treatment for total skull bone volume (Cohen's d = 2.81) was larger than the effect size for cranial circumference (Cohen's d = 2.23). In the context of potential usefulness of total skull bone volume as a screening measure to help identify a larger proportion of individuals with FASD, the relative sensitivity of total skull bone volume (a novel candidate measure) was compared to the cranial circumference (similar to head

Table VI. Results of univariate ROC analysis: Areas under ROC curve (AUCs) are shown for (a) skull bone volumetric measurements and cranial circumference

(a) Bone	No Covariates					
	BA vs NC	HBA vs NC	BA vs SC	HBA vs SC	NC vs SC	HBA vs BA
Mandible	**1**	**1**	**1**	**1**	0.734	0.656
Frontal	**1**	**1**	**1**	**1**	0.594	0.615
Parietal	**1**	0.990	**1**	**1**	**0.766**	0.625
Occipital	0.984	**1**	0.938	0.979	0.547	**0.708**
Nasal	0.891	0.771	0.828	0.740	0.531	0.510
Maxilla	**1**	0.958	0.969	0.927	0.563	0.563
Lacrimal	0.953	0.927	0.984	0.958	0.734	0.542
Jugal	0.984	0.979	**1**	**1**	0.547	0.635
Total skull bone	**1**	**1**	**1**	**1**	0.578	0.531
Cranial circumference	0.984	0.948	0.984	0.875	0.531	0.635

Best AUC results in each comparison are highlighted in bold.

Table VII. Results of univariate ROC analysis: Areas under ROC curve (AUCs) are shown (b) skull distance measurements

(b) Skull	BA vs NC	HBA vs NC	BA vs SC	HBA vs SC	NC vs SC	HBA vs BA
Upper facial depth	0.906	0.885	0.922	0.844	0.500	0.698
Lower facial depth	0.719	0.813	0.703	0.771	0.547	0.583
Cranial circumference	0.969	0.927	0.875	0.833	0.578	0.542
Orbital height	0.547	0.542	0.844	0.781	**0.844**	0.542
Orbital width	0.734	0.698	0.781	0.792	0.578	0.646
Minimal frontal width	0.953	0.927	0.734	0.760	0.500	0.510
Bitragal width	0.891	0.865	0.906	0.844	0.531	0.656
Bigonial width	0.578	0.510	0.844	0.823	0.797	0.604
Interorbital distance	**0.984**	**0.990**	**1**	**1**	0.781	0.500
Skull Nasal length	0.625	0.750	0.625	0.677	0.547	**0.802**

Best AUC results in each comparison are highlighted in bold.

Table VIII. Results of univariate ROC analysis: Areas under ROC curve (AUCs) are shown for (c) face distance measurements and cranial circumference

(c) Face	BA vs NC	HBA vs NC	BA vs SC	HBA vs SC	NC vs SC	HBA vs BA
Nasal width	0.891	0.781	0.828	0.708	0.609	0.594
Face Nasal length	0.531	0.771	0.531	0.719	0.578	0.729
Nasal bridge length	0.531	0.802	0.500	0.719	0.516	**0.781**
Philtrum length	0.766	0.563	0.938	0.833	**0.766**	0.677
Lower facial height	0.688	0.510	0.875	0.563	0.719	0.688
Mid-facial depth	0.766	0.854	0.703	0.760	0.563	0.583
Lower facial depth	0.781	0.917	0.672	0.729	0.734	0.552
Palpebral fissure length	0.641	0.510	0.750	0.531	0.516	0.729
Inner canthal width	**1**	0.906	**0.984**	**0.906**	0.688	0.573
Outer canthal width	0.906	0.646	0.891	0.802	0.688	0.677
Cranial circumference	0.948	**0.948**	**0.984**	0.875	0.531	0.635

Best AUC results in each comparison are highlighted in bold.

circumference in clinical screening in which scores $\leq 10^{th}$ percentile are used to help diagnose FAS). Lambs of the NC and SC groups were combined (n = 16) and the 10^{th} percentile of this combined control group was established for both the cranial circumference measure (390.7 mm) and the total skull bone volume measure (254358 mm^3). Alcohol-exposed lambs of both groups (BA and HBA) were then predicted based on whether or not they were less than the 10^{th} percentile cutoff. For cranial circumference, 14 out of 20 alcohol-exposed lambs (70%) were under the cutoff (7/8 BA; 1/12 HBA), whereas all 20 of the alcohol-exposed lambs (100%) were under the cutoff for total skull volume. A two-tailed Fisher's Exact Test confirmed that the classification based on total skull bone volume was significantly more sensitive than the one based on cranial circumference ($p = 0.020$).

II.5 Discussion

Although facial dysmorphology is a cardinal feature of FAS, children with FASD may not have identifiable features or their facial features may be too subtle to detect reliably on clinical exam [99, 130, 131]. As a result, many children exposed prenatally to alcohol are not recognized as having FASD until later in adolescence when unruly behavior or developmental and learning disabilities become problematic. This study of lambs born to ewes given alcohol during the first trimester equivalent tested whether more sensitive structural indices could be achieved from a single CT scan of the head. Quantitative measures obtained from this scan provide a novel biomarker for prenatal alcohol exposure utilizing individual bone volumes and collectively, the total skull bone volume. The scan also allows for morphometric measures, skull bone and soft tissue, which model anthropometric studies in humans [103, 132, 133] and rodents [122, 126].

An important discovery from this sheep model is that quantitative volume measures of the bones of the neurocranium may be one of the most sensitive structural indicators of the effects of binge alcohol during the first eight weeks of human pregnancy. Both the binge alcohol (BA) and heavy binge alcohol (HBA) treatments resulted in significant and severe reductions in total skull bone volume, volumes of the frontal, parietal, occipital, maxilla, mandible, lacrimal, and jugal bones, as well as cranial circumference. After statistically controlling for smaller cranial circumference in the alcohol-exposed groups, significant reductions in the volumes of the parietal and occipital bones were evident in the HBA group. Discriminant analysis showed that the frontal bone, parietal bone and total skull bone volumes achieved 100% sensitivity and specificity in predicting prenatal treatment (alcohol or control). Volumes of these bones were better predictors of alcohol exposure than cranial circumference, and were consistent with the greater effect size of alcohol treatment for total skull bone volume (d = 2.81) and cranial circumference (d = 2.23). All alcohol-exposed lambs were at or below the 10th percentile of the control lamb distribution for total skull bone volume. The sensitivity of classification of alcohol-exposure based on this 10th percentile cutoff for total skull volume was significantly better than a similar classification based on a 10th percentile cutoff for cranial circumference. Taken together, these findings suggest that CT derived measures of neurocranial bone volumes may provide a novel method for identifying children with FASD.

Cranial circumference in this model is directly parallel to reduced head circumference in FAS. Head circumference is routinely evaluated on a physical exam [103, 134] and is a simple, direct and easily-obtained measure that has population norms. The smaller head circumference found in children with FAS [135, 136] has been modeled in mice exposed to alcohol prenatally [126] and was replicated in this study. However, the results in this study indicate that total skull volume is more sensitive and more accurate than cranial circumference in predicting prenatal alcohol exposure, even though the two measures were strongly correlated (r = 0.939). These findings suggest that, if skull bone volume determinations could safely become available in alcohol-exposed and non-exposed children, the neurocranium bone volume would be a more accurate predictor of prenatal alcohol exposure than either facial dysmorphology or head circumference.

Although CT scanning of the head is not without risk and segmentation of the skull bones may be clinically demanding, quantitative CT scans eventually could provide better identification of prenatal alcohol exposure in clinical screening of children at risk for FASD. The lack of age-specific norms for cranial bone volumes and the potential risk of unnecessary radiation exposure with elective use of CT in children currently limits application of this approach in helping identify children with FASD. While it may be possible to build a reasonably large normative data base from CT scans in children undergoing head CT for medical purposes, perhaps it is more difficult to justify non-diagnostic CT scans for FASD (or other) children. Nevertheless, research and development efforts in biomedical imaging are improving safety by lowering scan times and creating new technology that reduces radiation exposure. For example, electron-beam

CT is a relatively new technology. A study in children found that multi-detector CT delivered higher doses of radiation compared with the doses delivered in electron-beam CT [137]. In time, as electron-beam CT and other technology becomes more clinically available, it is reasonable to expect that the safety of CT will sufficiently outweigh the risks and that the quantitative approaches used in this study will become clinically feasible on a routine basis.

Prenatal alcohol exposure significantly affected all three of the neurocranium bones (frontal, parietal and occipital) and four of the five viscerocranium bones (maxilla, mandible, lacrimal, jugal, but not nasal). Overall, the bone volume changes were highly correlated, such that in the analysis using total skull bone volume as a covariate, none of the individual bone volumes remained significant. However, the neurocranium bone volumes were generally better predictors of prenatal alcohol exposure in the discriminant analysis, and only the parietal and occipital bones distinguished the HBA group after the effects of cranial circumference were statistically removed. The neurocranium bones are directly and anatomically related to the three skull distance measures (upper facial depth, bitragal width, interorbital distance) and one facial measure (inner canthal width) that were significantly reduced in the binge and heavy binge alcohol treatments. Thus, it appears that prenatal binge alcohol exposure effects on head and skull measures may be more directly related to growth of the neurocranium than the viscerocranium, and relative to routine FAS screening measures, alcohol-induced reductions in the neurocranium volumes may provide better detection of prenatal alcohol exposure.

In comparing the two binge alcohol exposure treatments, no significant differences were evident in any of the volumetric or linear distances in the BA and HBA treatments in the absence of covariance analysis. The two alcohol treatments used in this "weekend binge drinking" model of the first eight weeks of human pregnancy both produced relatively high peak blood alcohol concentrations (199 and 280 mg/dl, respectively). Both alcohol treatments were equally prone to produce skull volume and craniofacial changes. The 1.75 g/kg per day dose was sufficient to induce craniofacial abnormalities. The only differences identified in the BA and HBA treatments were from the covariance analysis (with cranial circumference and sex as covariates), which statistically controlled for overall effects of head size. In that analysis, the HBA treatment produced significantly greater reductions than the BA treatment in the adjusted means of the occipital bone volume. The occipital bone was also the most accurate predictor in distinguishing between the BA and HBA treatments in the discriminant analysis. This suggests that the occipital bone volume may be a sensitive biomarker for increasing severity of binge drinking during the first trimester.

In terms of craniofacial distance measures, reductions in three of the nine bone distances (upper facial depth, bitragal width, interorbital distance) and one of the ten soft-tissue face distances (inner canthal width) distinguished BA and HBA lambs from NC and SC lambs. All four measures were highly correlated with cranial circumference. When cranial circumference was used as a covariate, none of the measures remained significant between the BA and HBA groups and the NC and SC groups. The interorbital distance predicted the alcohol-exposed treatments from the control treatments with 93.8-100%

accuracy (87.5-100% sensitivities and 93.8-100% specificities) and, the inner canthal width was 90-100% accurate (87.5-100% sensitivities and 75-100% specificities). There were significant correlations between several facial measures and the underlying bone measures that were closely associated with those facial features. Significant reductions in the correlated measures of interorbital distance (bone) and inner canthal width (face), as well as the high accuracy in classifying prenatal alcohol treatment based on interorbital distance and on inner canthal width, suggests that these two measures (associated with reduced distances between the eyes) may also help identify children with FASD. These findings are the first report of quantitative skull and facial morphometric changes in the sheep model of maternal binge alcohol exposure during a portion of the first trimester equivalent.

A previous rodent study analyzed facial measurements on embryonic day 17 C57BL/6N mice and found significant treatment effects in 12 of the 15 measures analyzed. Four measures (upper face, mid-face, nasal length, nasal bridge) identified the alcohol group from the pair and chow fed groups [122], which showed only partial correspondence to the four measures identified in this sheep study (upper facial depth, bitragal width, interorbital distance, and inner canthal width). Differences between the mouse model and sheep model outcomes could be explained either by differences in 1) alcohol exposure models (with the sheep model involving a more direct experimental control over binge-like exposure), 2) the older developmental status of the sheep (peripubertal lambs compared to late-fetal mice), or 3) species differences between sheep and rodents in how alcohol alters craniofacial development.

A comparable CT study of skull morphology was conducted in 21-day-old C57BL/6J mice that showed bone volumes were capable of identifying alcohol-exposed offspring [126], similar to findings in this study. The mouse model studies, involving maternal consumption of alcohol liquid diets, produce prenatal and postnatal growth deficits in offspring that can be conflated with craniofacial bone growth deficits. In this sheep model paradigm, there were no significant effects on birth weight or postnatal growth of the lambs.

Palpebral fissure length is a cardinal feature to assess FAS in children [97, 98, 133, 138], yet palpebral fissure length was not reliably affected in this sheep model of prenatal alcohol exposure and it was not significantly correlated with cranial circumference or total skull bone volume. The results of this study indicate that neither the orbital height, orbital width (bone) nor the palpebral fissure length (face) were significantly different between alcohol-exposed and control lambs. This contrasts with a human study in which significant reductions were found in palpebral fissure length, inner canthal width and outer canthal width [132]. A recent human study concluded that palpebral fissure length and head circumference are independent of each other and that short palpebral fissures are likely reduced due to forebrain damage, not necessarily due to smaller head size [129]. In the embryonic mouse model, a direct correlation was identified between reduced palpebral fissure length and reduced globe size as well as forebrain reduction implicating a correlation to forebrain damage [139]. Palpebral fissure length in this sheep model was not useful in distinguishing between the four treatment groups. In contrast and consistent with the human study by Moore and colleagues, the sheep model did find significant alcohol-induced reductions in the inner canthal width relative to controls (NC; SC), and the outer canthal width was significantly reduced relative to the SC group. This suggests that in the sheep model, craniofacial effects are more prominent in measures linked to craniofacial and skull width development (inner and outer canthal widths, interorbital widths, bitragal width, upper facial depth) rather than direct orbital measures. These differences may reflect species differences in response to alcohol exposure, or they may point to a previously unrecognized sensitivity of mid-facial width measurements in FASD screening. The Moore et al. study also included a wide range of ages, an ethnically diverse population and unknown maternal drinking history. These sources of variance may have important influences on craniofacial morphometry.

There are many translational advantages of the sheep model of FASD (Cudd, 2005), in which dose, pattern and timing of alcohol exposure are experimentally controlled. The resulting blood alcohol concentrations are known and these underscore the translational importance of the current findings that identify neurocranium bone volumes as a potential biomarker of prenatal alcohol exposure. Sheep model studies are limited by several factors that make it difficult to get large sample sizes and adequate sex representation for experiments. Studies take longer to complete, are more labor intensive and are more expensive than rodent studies. Despite these limitations, experimental studies can be done utilizing the sheep model in a translational role for preclinical studies of FASD. This is due to improved ability in controlling and matching the experimental conditions of daily patterns, developmental timing of alcohol exposure more similar to humans and the development of measures to advance diagnostic phenotypes of FASD.

Sheep have body weights and head/brain sizes that are more comparable to humans and they have long gestational periods (147 days) closely resembling human gestation (280 days). Sheep also have brain development stages *in utero* that can be matched more directly to prenatal brain development in humans [57]. Findings in this study illustrate the translational value of the sheep model, confirming that the effects on bone volumes are replicable in multiple species, but also provide novel evidence that neurocranium bone volumes may provide an optimal structural biomarker of the effects of first trimester binge drinking associated with FASD.

To summarize, these results confirmed our hypothesis that CT morphometric analysis is an effective tool for detecting prenatal binge alcohol exposure in lambs. Lambs born to ewes exposed to alcohol during the period of embryonic development comparable to the first eight weeks of human pregnancy had reduced CT-derived volumetrics of the bones and, less reliably, reduced facial and skull measures. Discriminant analysis of CT measures could identify alcohol-exposed from non-exposed lambs with 100% accuracy. These changes correlate to reduced craniofacial bone volumes in the rodent model and reduced head circumference in both rodents and humans. Facial measurements in the sheep share some similarities in humans with FAS, including reductions in the upper facial depth, bitragal width, and inner canthal distance, but other dysmorphic effects seen in humans were not reliably produced in this sheep model (palpebral fissure width).

Several findings in this study highlight the potential translational value of the sheep model and the development of better diagnostic tools for craniofacial phenotypes of FASD. To the extent that CT scans can become feasible in FASD research settings, the findings in this study predict several relatively straightforward measures that should accurately identify otherwise non-dysmorphic children who experienced binge-like alcohol exposure during the first trimester. The best predictors would most likely be segmented bone volumes of the neurocranium (frontal, parietal, occipital or volume of the total skull). These measures should have high sensitivity and specificity in classifying prenatal binge-alcohol exposed children from non-exposed children. Inclusion of the occipital bone volume may also help determine which children were heavily exposed during the first trimester (likely to include those diagnosed with FAS). Concurrent use of multiple quantitative CT measures (e.g., neurocranium bone volumes together with cranial circumference, interorbital distance and inner canthal width) may further improve the reliability of classification. Implementation of CT morphometrics would also require establishment of age-specific normative data. The degree to which these bone structural phenotypes (observed in this study in peripubertal sheep) might change over development is not known, and whether they could be applied to earlier ages (childhood) or later ages (adolescence or young adulthood) remains to be determined. The implication is that development of comparative CT analysis may significantly improve the identification of children with FASD; individuals whose status otherwise would either be unknown, uncertain or overlooked.

II.6 Acknowledgments

This study was supported by Texas A&M CVM Post-Doctoral Grant (SMB) and NIAAA Grant AA017120 and AA18166-2 (SW). This work was done in conjunction with the Collaborative Initiative on Fetal Alcohol Spectrum Disorders (CIFASD), which is funded by grants from the National Institute on Alcohol and Alcohol Abuse (NIAAA). Additional information about CIFASD can be found at www.cifasd.org. Those participating in this study wish to acknowledge the primary and important role of the late Dr. Timothy Cudd in designing and initiating this work.

CHAPTER III

MATERNAL CHOLINE SUPPLEMENTATION IN A SHEEP MODEL OF FIRST TRIMESTER BINGE ALCOHOL FAILS TO PROTECT AGAINST BRAIN VOLUME REDUCTIONS IN PERIPUBERTAL LAMBS*

III.1 Overview

Fetal alcohol spectrum disorder (FASD) is *a leading potentially preventable birth defect.* Poor nutrition may contribute to adverse developmental outcomes of prenatal alcohol exposure and supplementation of essential micronutrients such as choline have shown benefit in rodent models. The sheep model of first trimester binge alcohol exposure was used in this study to model the dose of maternal choline supplementation used in an ongoing prospective clinical trial involving pregnancies at risk for FASD. Primary outcome measures included volumetrics of the whole brain, cerebellum and pituitary derived from magnetic resonance imaging

(MRI) in six-month-old lambs, testing the hypothesis that alcohol-exposed lambs would have brain volume reductions that would be ameliorated by maternal choline supplementation. Pregnant sheep were randomly assigned to one of five groups - heavy binge alcohol (HBA; 2.5 g/kg/treatment ethanol), heavy binge alcohol plus choline supplementation (HBC; 2.5 g/kg/treatment ethanol and 10 mg/kg/day choline), saline control (SC), saline control plus choline supplementation (SCC; 10 mg/kg/day choline and

---

*Reprinted with permission from "Maternal choline supplementation in a sheep model of first trimester binge alcohol fails to protect against brain volume reductions in peripubertal lambs" by Birch SM, Lenox MW, Kornegay JN, Paniagua B, Styner MA, Goodlett CR, Cudd TA, Washburn SE, 2016. *Alcohol*, 55: 1-8, Copyright © 2016 by Elsevier Inc.

normal control (NC). Ewes were given intravenous alcohol (HBA, HBC; mean peak BACs of ~280 mg/dl) or saline (SC, SCC) on three consecutive days per week from gestation day (GD) 4-41; choline was administered on GD 4-148. MRI scans of lamb brains were performed postnatally on day 182. Lambs from both alcohol groups (with or without choline) showed significant reductions in total brain volume; cerebellar and pituitary volumes were not significantly affected. This is the first report of MRI-derived volumetric brain reductions in a sheep model of FASD following binge-like alcohol exposure during the first trimester. These results also indicate that maternal choline supplementation comparable to doses in human studies fails to prevent brain volume reductions typically induced by first trimester binge alcohol exposure. Future analyses will assess behavioral outcomes along with regional brain and neurohistological measures.

III.2 Introduction

Prenatal alcohol exposure results in multiple teratogenic effects on central nervous system (CNS) development, including altered cellular proliferation and migration, decreased synaptic connectivity, increased apoptotic cell death and impaired myelination. These may all contribute to brain growth restriction, neurodevelopmental delays, changes in structure and function and resultant abnormal behavior and cognition [140-144]. The presence of CNS abnormalities, together with dysmorphic facial features and growth deficits, constitute the three characteristic phenotypes required to diagnose fetal alcohol syndrome (FAS) [98, 99]. However, the majority of children expressing adverse cognitive and neurodevelopmental effects resulting from prenatal alcohol exposure do not meet the diagnostic criteria for FAS. An umbrella classification, fetal alcohol spectrum disorders

(FASD), has been adopted to encompass the full spectrum of alcohol-related neurodevelopmental disorders [18, 145, 146].

Given that FASD is *a leading potentially preventable birth defect* [20], with prevalence estimates ranging from 1% [103, 104] to as high as 2-5% [105], priorities have been placed on efforts to develop early interventions that may provide significant benefits and thus mitigate the lifelong effects of FASD. Choline supplementation has emerged as a particularly promising nutraceutical therapeutic approach, based mainly on positive results from preclinical rodent models [147].

Choline is classified as an essential nutrient that has many important roles in brain development and function. It is involved directly as a precursor or through metabolites in maintaining the integrity of cell membranes and cell signaling, lipid and cholesterol transport, synthesis of the neurotransmitter acetylcholine, methyl metabolism, and DNA methylation [148, 149]. The recommended daily intake of choline for pregnant women is 450 mg/day [150]. During pregnancy, phosphatidylcholine production is increased in the liver, providing an important source of choline to the developing fetus [151]. Choline deficiency has been implicated in the molecular etiology of FASD because alcohol can decrease choline availability to the fetus by several mechanisms. The detrimental effects of choline deficiency may be further exacerbated by reduced maternal intake of choline and thus fetal deficiency of choline can ultimately contribute to abnormal brain development [151, 152].

Studies with rodent models of FASD over the last 15 years by Thomas and colleagues as well as by others have demonstrated that choline administration during and/or after the time of alcohol exposure (either during gestation or during the early neonatal period of brain development in rats comparable to that of the human third trimester) can significantly improve a variety of alcohol-induced neurobehavioral deficits. Choline supplementation has been shown to improve deficits in behavioral and physical development and brain weight [153], spatial learning and memory [154, 155], spatial working memory [156], visual discrimination [157], locomotor hyperactivity [158, 159], trace fear conditioning [160], and trace eyeblink conditioning [161]. Positive improvements associated with choline supplementation in the rodent models were achieved with daily doses (typically 250 mg/kg/day) that far exceed the minimum daily choline requirements for rodents.

Based on these promising results from the rodent models, the Collaborative Initiative on Fetal Alcohol Spectrum Disorders (CIFASD) designed and implemented a prospective randomized clinical trial in the Ukraine involving multivitamin and mineral (MVM) supplements in which a subgroup of the MVM group was also given a choline supplement (750 mg/day, about 10 mg/kg/day) as an additional component of the MVM intervention. The sheep model study reported here was concurrently designed to optimize the translational comparisons with the prospective randomized human clinical trial. A choline dosing regimen of 10 mg/kg/day was selected and the choline supplement was started at the beginning of pregnancy (at the start of the binge alcohol exposure period), whereas in clinical trials, participants were enrolled after the first prenatal appointment (typically around 19 weeks gestation). Choline supplementation was initiated at the start of alcohol exposure in the current study to maximize the likelihood of benefits from early intervention. This is the first report of the sheep model with choline supplementation which models the CIFASD Ukrainian clinical trial which was recently published [162].

Although rodent studies have provided the primary foundation of research in FASD, including the use of choline as a potential intervention, the sheep model provides important (if not unique) translational value. The gestational period in sheep is relatively long (147 days) with the first trimester human equivalent extending from GD 4-41, the second trimester equivalent from GD 42-108, and the third trimester equivalent from GD 109-132 [163]. Sheep also serve as a better model for humans in terms of the rate of brain development over gestation (the third trimester equivalent takes place in-utero similarly to humans and in contrast to the rodent model), the body and brain mass of the fetus and maternal-fetal physiology. Techniques for instrumentation and experimental manipulation of the pregnant ewe are also now well established and feasible.

The primary goal of this study was to model binge drinking in the first trimester and evaluate maternal choline supplementation administered throughout gestation as a preventative intervention for pregnancies at risk for FASD. We used a heavy binge-like alcohol treatment to model repeated weekend binge drinking over the first trimester equivalent (GD 4-41), a pattern of drinking which is similar in women who abuse alcohol during pregnancy and a known risk factor for FASD [109, 111, 164]. A second goal of this study was to incorporate structural volumetrics with MRI to obtain brain volume measures like those done in human studies. Although the use of MRI is routine in clinical veterinary medicine, quantitative 3-dimensional brain imaging for experimental studies has not been developed for use in sheep or other large animals. Therefore many of the tools for automated segmentation and quantification of various brain regions, commonly available in humans and rodents [165], have not been developed for experimental veterinary applications. For this study, protocols and procedures were developed so that quantitative data from the sheep brain could be compared to measures routinely available from structural imaging in children with FASD [166]. Volumetric reductions have been demonstrated in the whole brain [167-169] and cerebellum [25, 42, 50, 170] and many studies have documented more selective changes in specific brain regions [171, 172].

Given our goal of implementing structural MRI protocols in the sheep model, our first approach was to obtain quantitative volumetric data of the whole brain of peripubertal lambs (six months old), a stage roughly equivalent to children entering puberty during early adolescence [124]. The cerebellum was also evaluated because it is easily segmented and it is known to be vulnerable to prenatal alcohol exposure [29, 42, 170, 173, 174]. We also quantified the volume of the pituitary as a potentially contrasting outcome, given the interesting findings reported in mouse models of binge-like gestational exposure. In these studies, exposure either on gestational day 8 or on gestational days 12-16 yielded increased pituitary volume when assessed on gestational day 17 [175, 176]. Our fundamental hypothesis was that prenatal binge-like alcohol exposure over the first trimester equivalent would produce brain volume reductions detectable by MRI, directly modeling the microencephaly seen in children with FAS. We also tested the hypothesis that maternal supplementation of choline in doses similar to those used in the CIFASD clinical trial, administered throughout the entire pregnancy, would protect against brain volume reductions.

III.3 Materials and methods

III.3.1 Animals

All animals and experimental procedures were approved by the Institutional Animal Care and Use Committee (IACUC) at Texas A&M University. Prior to breeding, Suffolk ewes (aged 2-5 years) received multi-species Clostridium bacterin-toxoid (Covexin 8, Intervet/Schering-Plough Animal Health, Summit, NJ) 2 ml intramuscularly, albendazole (Valbazen Suspension 7.5 mg/kg, Pfizer Animal Health, New York, NY) 0.75 ml/25 lb of body weight orally, and ivermectin (Ivomec Drench for Sheep 0.8%, Merial, Duluth, GA) 3 ml/26 lb body weight orally. The day of mating, corresponding to when ewes were marked by the ram, was designated as GD 0. Ewes were penned individually but had visual contact at all times with herd mates in adjacent pens in an environmentally regulated facility (22°C and a 12:12 light/dark cycle). Pregnancy was confirmed ultrasonographically on GD 25 and ewes that were not pregnant were removed from the experiment. Ewes were fed a “complete” ration (TAMU Ewe Ration, Nutrena, Cargill, Minneapolis, MN) designed to meet 100% National Research Council requirements (feed does not include choline) as calculated by ARIES (software version 2007, University of California, Davis) and had free access to drinking water. Maternal food consumption was monitored daily. All subjects consumed all feed offered.

III.3.2 Choline dose development

The aim of this study was to model the choline dose implemented in the CIFASD clinical trial, thus providing a strong basis for translational comparisons. This study intentionally avoided the very high doses of choline used in the rodent models (~250 mg/kg per day) because they are ~25X higher (on a per kg basis) than the doses used in the Ukraine clinical trial (Coles et al., 2015). The high choline doses often used in rodent studies are not likely to be used in clinical studies in pregnant women. The choline dose we chose (10 mg/kg per day) is higher than what the current daily recommended dose is during human pregnancy (450 mg/day, ~6mg/kg per day). In the CIFASD randomized clinical trial, alcohol-using and nondrinking women were randomized to one of three multivitamin/mineral supplement groups: none, multivitamins/minerals (MVM), and multivitamin/minerals plus choline. The choline group was given a daily dose of 750 mg (~10 mg/kg per day), thus helping to guide the decision for the dose of choline used in the sheep model [162]. Higher daily doses of choline (on a mg/kg basis) may be given postnatally in humans [177], but this sheep model was developed to test choline supplementation during pregnancy with binge-like alcohol exposure during the first trimester equivalent. Consequently, the dosing regimen used in this sheep model is both relevant and highly translational in respect to dose of choline and timing outcome of the children postnatally.

In ruminants, choline is absorbed maximally in the abomasum and small intestine but it is often degraded in the rumen on its way. Because of this, a commercially available microencapsulated choline supplement (designed for ruminants, primarily dairy cattle) was developed to allow the choline supplement to survive transfer through the rumen where it can be absorbed in the abomasum and small intestine (ReaShure® (choline chloride 28.8%), Balchem Corporation, New Hampton, NY). To test this product in sheep, we fed 10 mg/kg of choline (based on weight of choline in ReaShure®) to ten nonpregnant ewes and then collected abomasal contents 30, 60 and 120 min after administration. Choline levels in these samples were compared to the abomasal contents from 6 normal control animals that did not receive a choline supplement. The level of choline in the abomasum was significantly higher in both the 30 min (848 nmol/ml) and 60 min (627 nmol/ml) samples following choline administration with ReaShure® as compared to the normal controls (557 nmol/ml) ($p < 0.001$). Abomasal levels returned to baseline levels comparable to the normal controls at the 120 min time point.

In a second preliminary study to evaluate plasma choline and betaine levels, 14 pregnant ewes were assigned to three treatment groups: 1) saline control choline (SCC; isotonic saline (0.9%) during the 1st trimester plus 10 mg/kg/day choline until GD 133), 2) heavy binge alcohol (HBA; 2.5 g/kg/treatment ethanol during the 1st trimester), and 3) heavy binge alcohol plus choline (HBC; 2.5 g/kg/treatment ethanol during 1st trimester plus 10 mg/kg/day choline until GD 133). Plasma samples were collected on GD 134 and shipped frozen to the laboratory of Dr. C. Keen at University of California-Davis, who performed the choline analyses using mass spectroscopy. Due to the limited number of available ewes, no saline control (SC; no choline) group was included for the GD 134 samples. However, a set of four normal control (NC) ewes were sampled on GD 147 to provide a comparative index of choline levels during late pregnancy. For the GD 134 samples, plasma choline levels were significantly higher ($p < 0.05$) in the two choline treated groups, SCC (5.55 ± 0.03 µM) and HBC (6.08 ± 0.62 µM), compared to the alcohol only group, HBA (3.94 ± 0.15 µM). Betaine levels were significantly higher ($p < 0.01$) in the HBC group (210.1 ± 8.7 µM) compared to the SCC group (131.1 ± 1.1 µM) and the

HBA group (118.4 ± 12.8 µM). For the NC plasma samples from GD 147, the levels for choline and betaine, respectively, were 5.06 ± 0.56 µM and 147.5 ± 21.8 µM. Overall, these data suggest that the first trimester binge alcohol treatments may reduce choline levels and metabolism but that the choline supplementation appears to increase choline levels and choline metabolism in the HBC group. Also, choline supplementation did not influence blood alcohol concentrations (~280 mg/dl) which indicates that the fetal exposure to alcohol with the maternal intravenous alcohol infusions was not altered by choline administration.

III.3.3 Treatment groups

Ewes (n = 44) were randomly assigned to one of five treatments - normal control (NC) group (n = 8 ewes), saline control group (SC; isotonic saline (0.9%)) group (n = 8 ewes), saline control plus choline (SCC; isotonic saline (0.9%) plus 10 mg/kg/day choline) group (n = 6 ewes), heavy binge alcohol (HBA; 2.5 g/kg/treatment ethanol) group (n = 14 ewes), and heavy binge alcohol plus choline (HBC; 2.5 g/kg/treatment ethanol plus 10 mg/kg/day choline) group (n = 8). The alcohol infusions in ewes modeled a weekend binge drinking pattern over the first trimester-equivalent in sheep (GD 4-41), with alcohol administered on three consecutive days per week, followed by four days without treatment (18 treatments in total).

An intravenous catheter (16 ga., 5.25 inch Angiocath™; Becton Dickinson, Sandy, UT) was placed into the jugular vein of each ewe (except for the NC group) on GD 4. Beginning on this day, alcohol (2.5 g/kg body weight) or saline was administered intravenously via a pump over a 1-hour period (VetFlo® 7701B IV Vet Infusion Pump, Grady Medical, Temecula, CA). The alcohol solution was prepared by adding 95% ethanol to sterile 0.9% saline to achieve a 40% w/v alcohol solution. Solutions were prepared under aseptic conditions and passed through a 0.2 μm bacteriostatic filter. The saline control group received an infusion of isotonic saline (0.9%) that was equal in volume to the alcohol infusions. Lambs produced from ewes in the five treatment groups that entered the imaging study included 8 NC lambs (2 females, 6 males), 8 SC lambs (4 females, 4 males), 6 SCC lambs (2 females, 4 males), 14 HBA lambs (7 females, 7 males), and 8 HBC (2 females, 6 males).

Ewes in the SCC and HBC treatment groups received 10 mg/kg oral choline (ReaShure® (choline chloride 28.8%; daily dose based on weight of choline, Balchem Corporation, New Hampton, NY) in which the supplement was mixed with their daily feed for the entirety of their pregnancy.

III.3.4 Maternal blood alcohol concentration

To measure peak BAC, blood was drawn from the jugular vein of each ewe one hour after alcohol infusions began on GD 6, 27, and 41, as previously described [109, 128]. A 20 μl aliquot of blood was collected in a microcapillary tube and transferred into a vial containing 0.6 N perchloric acid and 4 mM n-propyl alcohol (internal standard) in distilled water. The vial was tightly capped with a septum-sealed lid and stored at room temperature until analysis by headspace gas chromatography (Varian Associates model 3900, Palo Alto, CA) within 24 h of collection.

III.3.5 Postnatal management

At birth, newborn lambs were weighed and measured, their navels were dipped in iodine (VetOne Stronger Iodine, 7%, MWI, Meridian, ID) and they were given oxytetracycline (Liquamycin®, LA-200®, 200 mg/ml, Pfizer Animal Health, New York, NY) 1 ml intramuscularly and selenium/vitamin E (BO-SE®, 1 mg/ml, Intervet/Schering-Plough Animal Health, Summit, NJ) 0.5 ml subcutaneously. Each ewe was checked for satisfactory milk production. Lambs were closely monitored for nursing until weaning at 2 months of age and weight gain and health status were recorded throughout the study. At one and two months of age, lambs were vaccinated using multi-species clostridium bacterin-toxoid (Covexin 8, Intervet/Schering-Plough Animal Health, Summit, NJ) 2 ml intramuscularly. Ewes were removed from the premises after weaning and lambs were housed in outdoor covered pens. At weaning, lambs received moxidectin (Cydectin® Oral Drench for Sheep 0.1%, 1mg/ml, Boehringer Ingelheim, St. Joseph, MO) 0.2 ml/kg body weight orally, amprolium (Corid® 9.6% Oral Solution, Merial, Duluth, GA) 0.5 ml/kg orally once daily for ten days, and vitamin B1 (Thiamine Hydrochloride, 500 mg/ml, Rafter 8 Products, Calgary, Alberta, Canada) 1.5 ml subcutaneously once daily every third day for a total of four treatments. Weaned lambs were fed a “complete” ration (Ringmaster Start-To-Finish Show Lamb Pellets, Nutrena, Minneapolis, MN) designed to meet 100% National Research Council requirements (feed does not contain choline) as calculated by ARIES (software version 2007, University of California, Davis), and had free access to drinking water.

At six months of age, lambs were euthanized using sodium pentobarbital, 75 mg/kg intravenously (Beuthanasia®, Intervet/Schering-Plough Animal Health, Summit, NJ). The right and left internal carotid arteries were exposed in the cervical region. They were catheterized with tubing (2mm, Masterflex, Cole Parmer, Niles IL) and sutured to the adjacent fascia. The corresponding right and left jugular veins were then exposed and cut transversely with a scalpel. Saline was administered intravenously through the carotid arteries to perfuse the brain over an approximate 15-min period via a peristaltic pump (Masterflex, model 7014-20, Cole Parmer, Niles IL) until the fluid draining from the jugular veins was clear. The brain was then perfused with formalin (SP® Buffered 10% Formalin, Cardinal Health, Dublin, OH) for an additional 15-min period. The head was removed at the atlanto-occipital joint and an MRI was performed immediately.

III.3.6 Magnetic resonance imaging

The formalin-perfused lamb heads were scanned in a 15 channel knee coil (TxRx, Siemens Medical, USA) at the Texas A&M Institute for Preclinical Studies (TIPS) using a dedicated Siemens Magnetom Verio 3T MRI scanner (Siemens Medical, USA). Images were acquired in the sagittal plane using the following Siemens MPRAGE (Ultrafast Gradient Echo 3D) sequence: TR = 2300 ms, TE = 3.79 ms, TI = 900 ms, FA = 9, Slice thickness = 0.43 mm, FoV = 256 mm x 256 mm, resolution = 0.4 mm x 0.4 mm x 0.4 mm, number of averages = 24, phase oversampling = 80%, and slice oversampling = 11.1%. Scan time was approximately 7 hours per specimen with ~288 2D slices per animal (Figure VIII).

III.3.7 Volumetric analysis

The whole brain volume and volumes of the cerebellum and the pituitary were manually segmented from each MRI slice (0.43 mm thickness) based on a previously described segmentation technique utilizing ITK Snap [178]. This software allows the lamb brains to be viewed and segmented slice-by-slice simultaneously in three dimensions. On each of the ~288 2D slices, the brain was manually segmented into the three regions of interest. ITK Snap was used to reassemble individual segmented slices into a 3D reconstruction so that the volume could be calculated (Figure IX). Absolute volumes were determined for the total brain, cerebellum, and pituitary gland individually. In addition, relative volumes were calculated by dividing the cerebellar and pituitary volume by the total brain volume from each subject and then multiplying by one hundred to determine a percentage of the total brain (a measure of cerebellar and pituitary effects relative to effects on whole brain).

III.3.8 Statistical analysis

Given the unequal numbers of males and females in the NC, SCC, and HBC groups and the low number of lambs of each sex across treatment groups overall, the power to detect potential sex differences was very limited. The data was first screened for potential differences between males and females. This was to determine whether the male and female data could be combined within groups for the purposes of statistical analyses without confounding the analysis of prenatal treatment. The NC, SCC, and HBC groups each had only two females. The within-group ranking of the data of those subjects was determined and each fell within the range of the majority sex of the group. Therefore, the individual data did not skew the within-group distribution for any measure of the NC, SCC or the HBC groups. For the two groups with equal numbers of males and females (SC and HBA), a two-way analyses of variance (ANOVA), with sex and treatment as the grouping factors was calculated. None of the measures showed a significant main or interactive effect of sex, so the data of males and females were combined within groups for subsequent analyses of variance.

Statistical analysis was performed with SigmaPlot® (Version 12.5, Systat Software, Inc). Data are presented as mean ± standard error of the mean (SEM). Treatment effects on measurements of total brain volume, cerebellum volume, pituitary volume, percentage cerebellum, and percentage pituitary were analyzed using a one-way ANOVA with a $p < 0.05$ level of significance. Body weights at birth and at six months and whole brain, cerebellar and pituitary volumes were analyzed initially with a one-way ANOVA (including the normal controls). In addition, those dependent variables were also analyzed with two-way ANOVAs (involving only four groups that were instrumented and infused (alcohol or saline) as grouping factors and omitting the NC group) to assess treatment effects of alcohol and choline supplementation. Measures meeting the significance level on the univariate one-way ANOVAs were followed by pairwise comparisons among the five treatments (four treatments with the two-way ANOVAs) within each measure with multiple comparisons corrected by the Holm-Sidak method.

III.4 Results

III.4.1 Maternal blood alcohol concentration

The mean ± SEM maternal BACs at the end of alcohol infusion (1 hour; point in time at which BACs are known to peak) were 280.5 ± 12.0 mg/dl in the heavy binge alcohol (HBA) group and 277.1 ± 9.0 mg/dl in the heavy binge alcohol plus choline (HBC) group. There were no statistically significant differences in BACs between these two groups or across days of sampling.

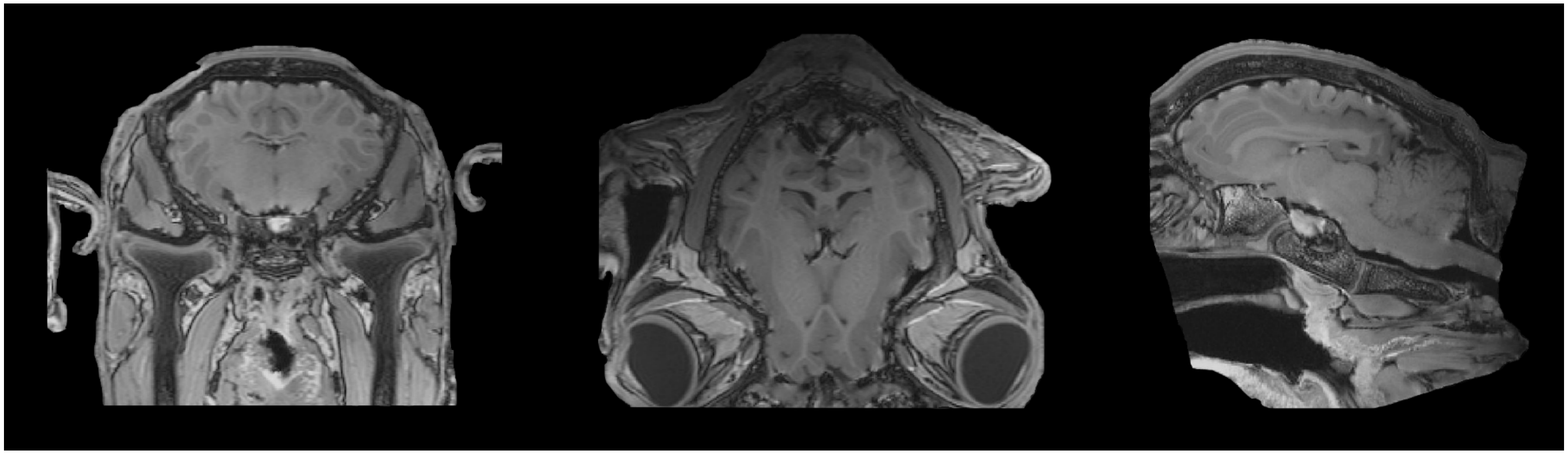

Figure VIII. Magnetic resonance imaging (MRI) derived images of a six-month-old lamb brain. From left to right, representative transverse (or coronal/frontal in humans), dorsal (or horizontal/transverse/axial in humans), sagittal views show high resolution.

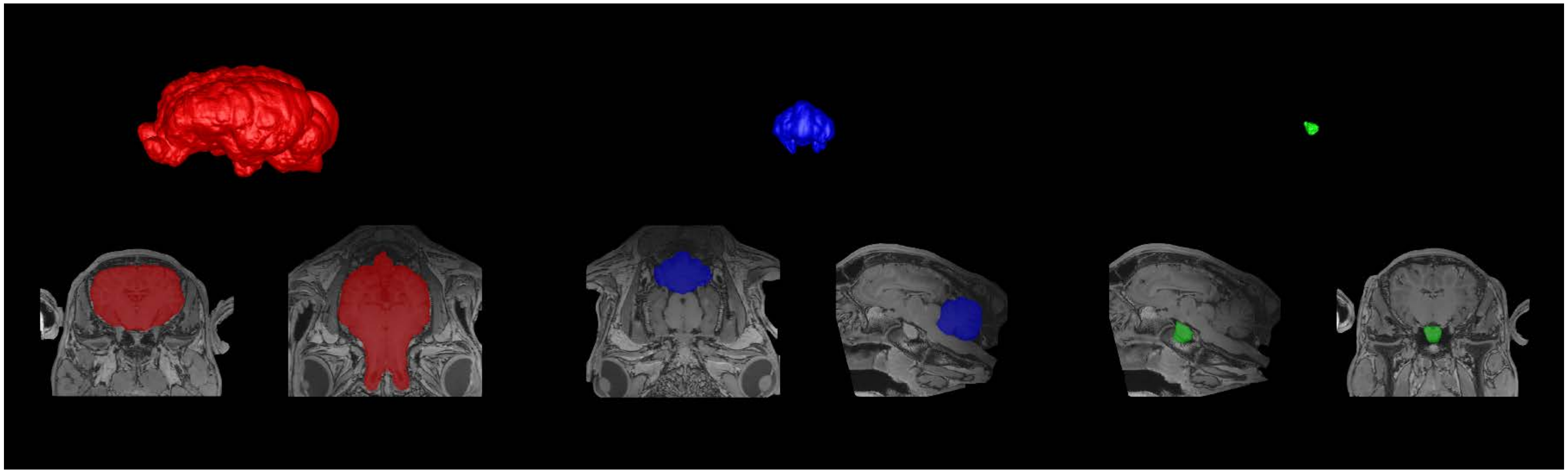

Figure IX. Manually segmented MRI derived images of a normal six-month-old lamb brain. Scans are color-coded and reconstructed in 3D in ITK-Snap [178] by which volumes are calculated: whole brain (red; transverse [coronal/frontal in humans] and dorsal [horizontal/transverse/axial in humans] views shown), cerebellum (blue; dorsal [horizontal/transverse/axial in humans] and sagittal views shown), and pituitary (green; sagittal and transverse [coronal/frontal in humans] views shown).

III.4.2 Birth and six-month-old body weights

Birth weights by group were 5.16 ± 0.60 kg (NC), 5.74 ± 0.33 kg (SC), 6.15 ± 0.65 kg (SCC), 4.34 ± 0.36 kg (HBA), and 4.94 ± 0.27 kg (HBC). Although these group differences were statistically significant in the overall one-way ANOVA (F (4, 39) = 2.650, p = 0.048), follow-up Holm-Sidak pairwise group comparisons showed no significant differences among the five treatment groups, in part because the NC group was highly variable and was intermediate between the two alcohol-exposed groups and the two saline control groups. The two-way ANOVA on birth weight, with alcohol and choline supplementation as grouping factors (omitting the NC group), yielded a significant main effect of alcohol administration, confirming the reduced birth weights of the alcohol-treated groups (F (1, 31) = 8.48, p = 0.007). There were no main or interactive effects of choline supplementation on birth weight.

For body weight at six months, there were no significant main or interactive effects of alcohol treatment or choline supplementation. Six month weights by group were 28.87 ± 3.74 kg (NC), 38.72 ± 4.04 kg (SC), 34.00 ± 3.07 kg (SCC), 33.22 ± 1.47 kg (HBA), and 33.75 ± 1.90 kg (HBC). The two-way ANOVA on six month body weights showed no significant main or interactive effects of alcohol treatment or choline supplementation.

III.4.3 Whole brain volume

As shown in Figure X (top row), significant effects among the five treatment groups were evident in the whole brain volume measures (one-way ANOVA, F (4, 39) = 9.575, p < 0.001). Follow-up pairwise comparisons (Holm-Sidak corrected) confirmed that the whole brain volumes of the two alcohol-exposed groups (HBA; HBC) were significantly reduced relative to the three control groups (NC; SC; SCC). There were no significant differences between the heavy binge alcohol groups, with (HBC) and without (HBA) choline supplementation, or among the three control (NC, SC, SCC) groups. In addition, the two-way ANOVA with alcohol and choline supplementation as grouping factors (omitting the NC group) yielded a significant main effect of alcohol administration, confirming the reduced whole brain volume of the alcohol-treated groups (F (1, 32) = 35.67, $p < 0.001$). There were no main or interactive effects of choline supplementation on whole brain volume.

III.4.4 Cerebellar and pituitary volumes

In one-way ANOVAs for absolute volumes of the cerebellum and pituitary, there were no significant differences among the five treatment groups in either the cerebellum (F (4, 39) = 2.280, p = 0.078) or pituitary (F (4, 39) = 0.774, p = 0.549) (Figure X; top row). There were also no significant differences in the relative volume, expressed as percent of the total brain, for the cerebellum (F (4, 39) = 0.959, p = 0.441) and pituitary (F (4, 39) = 1.104, p = 0.368) (Figure X; bottom row). However, with a two-way ANOVA for cerebellar volume involving the four prenatally infused groups (alcohol or saline, omitting the NC group), the main effect of alcohol administration reached statistical significance, confirming that alcohol reduced cerebellar volumes in the HBA and HBC groups (F (1, 32) = 9.29, p = 0.005). There were no main or interactive effects of choline supplementation on the cerebellar volume. For pituitary volume, the two-way ANOVA yielded no significant main or interactive effects of alcohol treatment or choline supplementation.

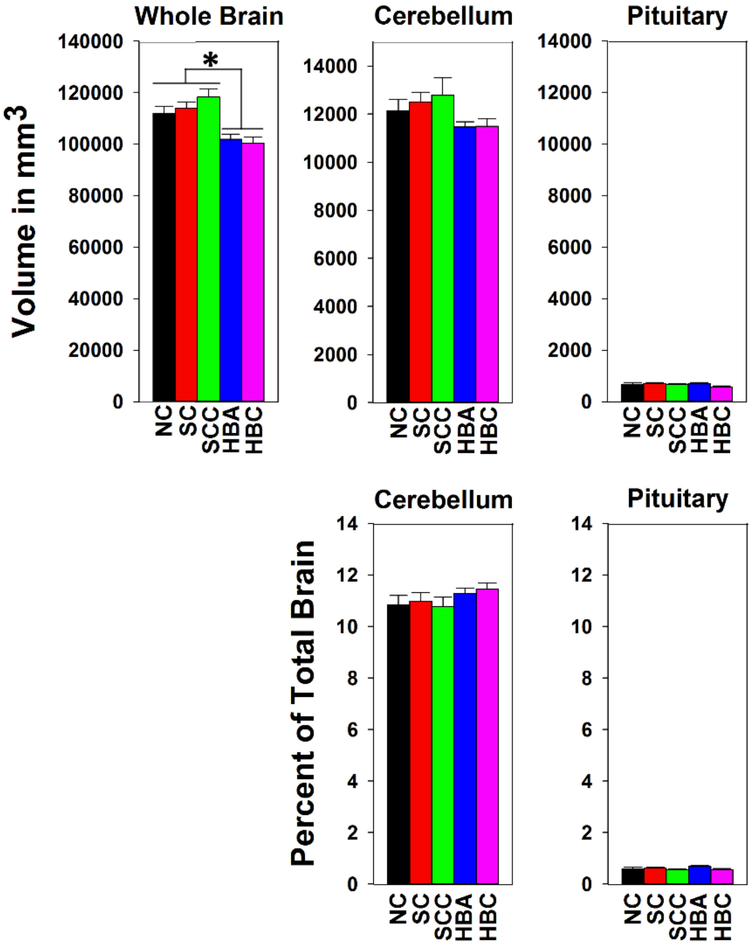

Figure X. Treatment effects on the whole brain, cerebellum, and pituitary volumes (top row) and treatment effects on the cerebellum and pituitary as a percentage of total brain size (bottom row). The y axis (top row) indicates the mean volume (+ SEM) in mm3 for whole brain volume, cerebellum and pituitary. Note the scale for the whole brain in the top left panel (maximum of 140,000 mm3) differs from that of the cerebellum and pituitary in the two top right panels (maximum of 14,000 mm3). The bottom panel is the percent total brain (maximum 14%). The ANOVA α level was 0.05, followed by the Holm-Sidak method for pairwise comparisons ($p < 0.05$). Significant group differences are indicated within each panel. An asterisk (*) indicates that the volumes of three control groups (NC, SC. SCC) were significantly greater than the two alcohol-exposed groups (HBA and HBC); NC, SC, and SCC did not differ from each other, and HBA and HBC did not differ from each other.

III.5 Discussion

The use of choline as an interventional strategy to lessen the effects of prenatal alcohol exposure on the developing fetus has been studied prenatally and postnatally in the rodent, showing some beneficial improvements in memory, behavior and cognition [153, 156, 158-160]. Currently, there is one published randomized clinical trial (from the CIFASD initiative) involving prenatal choline supplementation as a component of a multivitamin and mineral (MVM) supplementation trial (Coles et al., 2015). That study indicated benefits of the MVM supplements in infants on Bayley Mental Development scores (particularly in males), but there were no significant additional benefits of choline beyond these scores. Also, the MVM supplements did not prevent lower birthweights and head circumferences in the prenatal alcohol exposed infants. The current findings in this sheep model suggest that the reduced brain size and lower birth weights associated with first trimester binge alcohol exposure are not likely ameliorated with the dose of choline used (matched between the sheep study and the clinical trial), even if the choline supplements were started early in pregnancy and continued until birth.

Choline doses used in this study (10 mg/kg per day) were carefully matched to the dose used in the CIFASD clinical trial. However, on a mg/kg basis, this dose is more than an order of magnitude lower than the doses used in rodent studies that showed benefits in neurobehavioral and physical developmental outcomes (typically ~250 mg/kg per day). This raises the appropriate question as to whether the dose of choline needed to produce beneficial effects needs to be much higher than is currently used for clinical interventions. The failure of maternal choline supplementation to mitigate brain volume reductions associated with prenatal alcohol exposure suggests that any potential cognitive, cellular, and other benefits of choline in the sheep model of FASD, prenatally or postnatally, remains to be determined. Other complex questions about pharmacokinetics, metabolism and bioavailability of choline (as a nutraceutical) across species (rodents, sheep and humans) also need to be addressed in future studies. Additionally, most women are likely to consume varying amounts of choline in their daily diet. In the Ukraine clinical trial, the supplement they received is in addition to whatever amount of choline is present in their daily diet (Coles et al., 2015). Since the choline requirements in ruminants are not well established, most commercial rations do not contain choline. Therefore we can only say with certainty that the ewes received the 10 mg/kg/day choline for the duration of their pregnancy. If doses of choline (as a nutraceutical, rather than just to correct a deficiency) need to be high (as used in the rodent studies), this may limit the feasibility in clinical settings due to tolerability. Currently, there is one study in children (aged 2-5 years old) with FASD that assessed tolerability and potential adverse effects associated with choline supplementation [177] but this information is not known for pregnant women.

To our knowledge, there are no published human or animal model studies that evaluate volumetric structural brain measures with choline supplementation given either prenatally or postnatally with heavy binge-like alcohol exposure. The current study of lambs born to ewes given alcohol during the first trimester equivalent of gestation was intended to assess quantitative measures of three easily obtained structural volumes known to be affected by prenatal alcohol exposure in peripubertal lambs (modeling early adolescent children) and to determine whether prenatal choline supplementation has measureable effects on brain volume.

This is the first report of quantitative MRI showing reduced total brain volume in six-month-old lambs modeling heavy week-end binge drinking over the first trimester. Our finding of total brain volume reductions in alcohol-exposed lambs are consistent with numerous neuroimaging studies in children and young adults with known prenatal alcohol exposure and FASD regardless of whether they meet the full diagnostic criteria for FAS [166]. Brain imaging studies in murine models have also shown whole brain volume reductions (O'Leary-Moore, Parnell et al., 2010; [176]; [179]. Importantly, the prenatal alcohol-induced reductions in brain volumes observed in this sheep model occurred with a weekend binge exposure model that produced BAC profiles consistent with binge drinking (~280 mg/dl).

Significant reductions in absolute cerebellum volumes reported in this study (compared to saline-infused controls) were consistent with neuroimaging findings in humans [25, 42, 50, 170] while a contrasting study in rats found that cerebellar weight, volume, Purkinje cell number and granule cell density were only reduced in the third trimester and all three trimester exposure models. Moreover, data from the first trimester exposure did not differ from the control groups [180]. It is reasonable to conclude that cerebellar volume reduction is more severe when alcohol exposure extends beyond the first trimester, but even first trimester exposure can lead to significant cerebellar deficits. There would be value in analyzing regional volumes of other cortical and subcortical brain structures to determine whether they are more susceptible to first trimester alcohol exposure.

Consistent with prior murine studies [175, 176, 179, 181, 182], neither absolute nor relative pituitary volume differed significantly among the five treatment groups. However, two studies in GD 17 mice showed an increased pituitary volume following exposure to alcohol during GD 8 and 12-16 [175, 176].

Limitations with this model include increased time, effort, and expense associated with accruing representative numbers of sheep for evaluation. Also, because of the high expense of anesthesia and long MRI scan times to acquire high resolutions images, animals were euthanized and their brains were perfused with formalin immediately prior to scanning. Although possible, we do not believe that fixation would differentially affect alcohol exposed brains versus normal control brains.

In conclusion, our findings confirm that heavy binge alcohol exposure in the first trimester in the sheep model produces significant brain volume reductions in peripubertal lambs and that maternal choline supplementation at 10 mg/kg/day failed to prevent these reductions. MRI-based volumetric findings in the brain are comparable to outcomes reported for children and adolescents with FASD, further supporting the translational advantages of the sheep model. The lack of brain volume protection by gestational choline treatments suggest that even though choline supplementation in preclinical rodent studies benefits neurodevelopmental and cognitive functions, it may not spare brain volume. Future studies in this sheep model will evaluate behavioral and additional brain structure volumetrics.

III.6 Acknowledgements

This study was supported by Texas A&M CVM Post-Doctoral Grant (SB) and NIAAA Grant AA017120 and AA18166-2 (SW). This work was done in conjunction with the Collaborative Initiative on Fetal Alcohol Spectrum Disorders (CIFASD), which is funded by grants from the National Institute on Alcohol and Alcohol Abuse (NIAAA). Additional information about CIFASD can be found at www.cifasd.org. Those participating in this study wish to acknowledge the primary and important role of the late Dr. Timothy Cudd in designing and initiating this work. Additionally we would like to thank Dr. Jan Adams and Dr. Carl Keen in the Department of Nutrition at UC Davis for completing the choline mass spectroscopy work in our pilot studies.

CHAPTER IV

MAGNETIC RESONANCE IMAGING AND HISTOPATHOLOGY CORRELATION IN THE GOLDEN RETRIEVER MODEL FOR DUCHENNE MUSCULAR DYSTROPHY

IV.1 Overview

Duchenne muscular dystrophy (DMD) is an X-linked recessive disorder caused by mutations in the dystrophin gene. Affected boys have repeated cyclic events that include skeletal muscle necrosis, degeneration, attempts at regeneration, muscle atrophy and eventual replacement of skeletal muscle tissue by fibrofatty tissue. Golden retriever muscular dystrophy (GRMD) is genetically homologous and affected dogs demonstrate similar pathologic features. Magnetic resonance imaging (MRI) has been utilized in natural history and treatment studies in both of DMD and GRMD. Correlative registration studies of histological images to three-dimensional imaging modalities like MRI are essential to quantitatively analyze skeletal muscle changes. This study had three central aims, 1) register and correlate corresponding histology and MR images of the pectineus muscle using a novel registration technique, 2) compare a commercially available histology segmentation program (Aperio) to a novel custom algorithm for automated histomorphometry, and 3) compare outputs from 4.7T research and 3T clinical scanners to determine potential clinical application of the registration techniques. We found that histology and MR images co-registered but metrics were poorly correlated. Moreover, the custom algorithm and Aperio software provided similar results and with optimization, a fully automated algorithm could be applied to current research. Finally, only T1 values were correlated between the 4.7T or 3T scanners. Neither T1 values, nor any of the 3T metrics correlated with histologic segmentations.

IV.2 Introduction

Duchenne muscular dystrophy (DMD) is an X-linked recessive disorder caused by mutations in the dystrophin gene. Resulting muscle cell membrane fragility leads to recurring bouts of myofiber necrosis, with progressive replacement of muscle by fat and connective tissue [73, 183, 184].

Numerous therapies are being developed for DMD to either restore dystrophin expression or reverse secondary effects such as fibrosis and inflammation [185-187]. Traditionally, skeletal muscle biopsies have been considered the “gold standard” for not only diagnosis but also as an outcome parameter in clinical trials. Skeletal muscle pathology data in children are often limited to small biopsy samples [188], which may not be representative of the segmental nature of lesions and their muscle-wide distribution [189-191].

Magnetic resonance imaging (MRI) has been increasingly utilized as a non-invasive biomarker to evaluate DMD patients. Results from quantitative MRI studies have been shown to correlate with disease related parameters [192, 193]. While MRI allows numerous muscles to be assessed without the need for biopsy, few studies have correlated findings with histopathology. In one such study, Kinali et al. (2011) used semiquantitative indices to correlate MRI and histopathologic changes in the extensor digitorum brevis (EDB) of DMD patients.

Animal models play a major role in preclinical studies to determine treatment efficacy and side effects. The phenotype of dogs with golden retriever muscular dystrophy (GRMD) more closely mirrors that of affected boys compared to the mildly affected *mdx* mouse. Dystrophic dogs have a larger body, longer lifespan and early onset of disease in keeping with DMD [194]. Similar to humans, skeletal muscles lack dystrophin and undergo cycles of necrosis with eventual replacement by abundant fibrous tissue and some fat. A number of studies have defined MRI features in both GRMD natural history and preclinical trials [195, 196].

Although MRI is becoming a mainstay in DMD and animal model treatment trials, interpretation has been limited by a lack of systematic studies to correlate changes with histopathologic lesions. This study partially addressed this gap through three interrelated aims: a) quantitatively evaluate microscopic sections of muscle using a commercially available pathology software program (Aperio) and compare the results with those from a digitally matched corresponding MR image through a custom registration technique; b) develop a custom algorithm that automatically segments histopathology slides to counter the tedious and subjective nature of manual segmentation, and c) determine whether a clinical scanner could provide meaningful in vivo data by comparing output parameters from pectineus muscle scans performed on both a 3T clinical and 4.7T research scanner. We hypothesized that findings from co-registered MR and histology images would correlate, that comparable data would be provided by a custom automated algorithm and commercially available software program (Aperio), and that the 3T and 4T scanners would provide similar results, supporting use of this technique clinically.

IV.3 Materials and methods

IV.3.1 Animals

Dogs from a GRMD colony at Texas A&M University were cared for and assessed according to principles outlined in the National Research Council Guide for the Care and Use of Laboratory Animals. Their use was covered by Texas A&M Institutional Animal Care and Use Committee (IACUC) protocol, Standard Operating Procedures—Canine X-Linked Muscular Dystrophy (TAMU IACUC 2015-0110). The pectineus muscle was harvested post-mortem from nine GRMD dogs. Each muscle was placed into an individually labeled container with formalin (SP® Buffered 10% Formalin, Cardinal Health, Dublin, OH).

IV.3.2 Magnetic resonance imaging

We were motivated to reduce motion artifacts caused by vibrations that occur during high-resolution scans and to more closely simulate an in-vivo scan. Prior to scanning, each formalin fixed pectineus muscle was embedded in a 50ml conical tube (VWR, Radnor, PA) using a 0.08% agarose (Apex Bioresearch Products, Agarose General Purpose, San Diego, CA) gel (0.8 grams agarose in 100ml water). Each dog was identified with a numerical value and all investigators were blinded to identity. Samples were scanned first with the 3T scanner and then the 4.7T scanner. MRI metrics analyzed included T1, T2, water, fat, fractional anisotropy (FA), and apparent diffusion coefficient (ADC).

Embedded pectineus muscles were scanned in a 7cm ring coil (Siemens Medical, USA) at the Texas A&M College of Veterinary Medicine, Veterinary Medical Teaching

Hospital using a dedicated Siemens Magnetom Verio 3T MRI scanner (Siemens Medical, USA). Images were acquired in the transverse plane using the following Siemens T1_TSE_Dixon sequence: TR = 710 ms, TE = 38 ms, FA = 140, slice thickness = 2.0 mm, FoV = 50 mm x 50 mm, resolution = 0.2 mm x 0.2 mm x 2.0 mm, number of averages = 6, phase oversampling = 0%. Scan time was approximately 36 minutes per specimen with ~30 2D slices per sample. The next sequence used was T1_MAP sequence: TR = 16.7 ms, TE = 5.51 ms, FA = 4, 21, slice thickness = 1.7 mm with a 20% gap, FoV = 50 mm x 50 mm, resolution = 0.2 mm x 0.2 mm x 1.7 mm, number of averages = 9, phase oversampling = 10%. Scan time was approximately 51 minutes per specimen with ~30 2D slices per sample. The third sequence used was T2_MAP sequence: TR = 3500 ms, TE = 15, 30, 45, 60, 75, 90 ms, FA = 180, slice thickness = 2mm, FoV = 50 mm x 50 mm, resolution = 0.2 mm x 0.2 mm x 2.0 mm, number of averages = 1, phase oversampling = 0%. Scan time was approximately 15 minutes per specimen with ~30 2D slices per sample. The fourth sequence used was the RESOLVE DTI (Multi-shot echo planar imaging diffusion tensor imaging) sequence: TR = 4700 ms, TE = 68, 96 ms, FA = 180, slice thickness = 2 mm, FoV = 95 mm x 95 mm, resolution = 1.7 mm x 1.7 mm x 2.0 mm, number of averages = 1, phase oversampling = 0%, number of diffusion encoding directions = 13. Scan time was approximately 23 minutes per specimen with ~30 2D slices per sample.

These pectineus samples were next scanned in a 40 cm bore 4.7T Varian Bruker scanner equipped with an in-house developed birdcage coil. The T1-weighted images were acquired with TR = 268 ms, TE = 6.1 ms, FA = 21° and 72°, slice thickness = 1 mm, and a matrix size of 256 × 256 over a 30 × 30 mm^2 field of view (FOV), resolution = 0.12 mm x 0.12 mm and number of averages = 4. Four 5-slice acquisitions were interleaved to obtain 20 slices from each sample. Scan time was approximately 38 minutes per specimen. The T2-weighted images were acquired using a spin echo sequence with TR = 3s, TE = 20, 40, 60, 80 ms, slice thickness = 1 mm, matrix size = 256 x 256, FOV = 30 × 30 mm^2, slice thickness = 1mm, resolution 0.12 mm x 0.12 mm and number of averages = 1. Scan time was approximately 62 minutes per specimen. A third sequence, a three point Dixon sequence was acquired with TR = 1s, TE = 40 ms, slice thickness = 1mm and matrix size was 256 × 256 over 30 × 30 mm^2 of FOV and resolution = 0.12 mm × 0.12 mm. Scan time was approximately 26 minutes per specimen. A fourth sequence, a DTI (diffusion tensor imaging) sequence was acquired with TR = 3s, TE 68 ms, slice thickness = 1mm, and a matrix size = 128 x 128 over a 30 mm × 30 mm FOV, gradient = 8.5 Gauss/cm, δ (duration of gradient) = 7 ms, Δ (time between two gradients) = 25 ms, resolution = 0.23 mm × 0.23 mm and slice thickness = 1 mm, number of diffusion encoding directions = 6. Scan time was approximately 69 minutes per specimen. Twenty one millimeter thick transverse slices with a one millimeter slice gap were acquired to cover a 40 mm region including the middle of the muscle.

Upon completion of both scans, the pectineus muscle was removed from the agarose gel, rinsed in deionized water and placed back into formalin for storage.

IV.3.3 Histologic sectioning and processing of pectineus samples

The pectineus muscles were sectioned mid-muscle and the central cut was placed face down into a tissue cassette. Fixed tissues were paraffin-embedded and processed routinely. Five micrometer mid-muscle sections were trichrome stained. Histology slides were scanned on a NanoZoomer 2.0-HT slide scanning system to create digital files at a maximum 40x optical zoom (Hamamatsu, Japan).

IV.3.4 MR image and histology image registration

One of the authors (AE) exported the histology images at 10X magnification using NDPITools [197]. A mask was created using GIMP (GNU Image Manipulation Program, University of California, Berkley) and then images were resized, cropped, edited, retouched and authored with an open-source software program. An edge fitting tool based on a live-wire boundary extraction algorithm [198] was used to create a mask containing the segmented foreground of the histologic section. Masking removed the background portion of the scanned slide and artifacts around the borders of the muscle tissue (Figure XI, B). Histology images were imported into Matlab® for further processing. The in-plane resolution of the histology image was down-sampled to match the MRI resolution because the histology voxel resolution differed tremendously from the MRI voxel resolution (0.91 µm x 0.91 µm x 5.00 µm versus 0.12 mm x 0.12 mm x 1.00 mm). Histology images were then converted to HSV images and an adaptive histogram equalization algorithm was used to improve the texture of the hue images (Figure XI, C). Initial orientation of the histology image (trichrome) was determined by transforming it in the 3D MRI volume. Then, an optimization algorithm was used to refine the transformation parameters and generate an oblique MRI slice corresponding to the histology slice (Figure XI, D). Red channel and texture enhanced hue images were compared with the MRI images to increase visual similarity using affine transformation

(Figure XI, E). Finally, a non-rigid B-spline transformation was used to register the histology slice to the oblique MRI slice using Elastix registration software (Figure XI, F). The average T1, T2, water, fat, FA, and ADC data points were recorded from the MR image corresponding to the histopathology image that was graded (Figure XI).

IV.3.5 Aperio ImageScope segmentation of histopathology

Histology images were analyzed for compartment percentages of muscle, fibrous tissue, fat, and interstitial space. The interstitial space is defined as the non-staining white space in the slide and it included the fat and artefactual tears or spaces created by sectioning.

A board-certified veterinary anatomic pathologist (SMB) graded the pectineus digital histology images using an edited version of the positive pixel count algorithm (version 9.1) embedded in the Aperio ImageScope software (version 12.1.0.5029, Leica Biosystems, Nussloch, Germany). The algorithm parameters were optimized for trichrome staining: hue value = 0.66, hue width = 0.30, color saturation threshold = 0.04, lwp (high) = 200, lwp (low) = lp (high) = 200, and lp (low) = lsp (high) = 200.

The tissue (Figure XII, A) was first manually outlined with the pen tool in Aperio and artefactual tissue tears and creases were subtracted with the negative pen tool (Figure XII, B). The "manually outlined area" of the remaining tissue was calculated by the software in μm^2 and converted to mm^2 by dividing by one million. The Aperio algorithm output analyzes the manually segmented area composed of the numbers of strong pixels (Nsp; red staining with trichrome or fibrous/collagen tissue), negative pixels (Nn; blue staining with trichrome or muscle tissue), total of strong positive and negative pixels

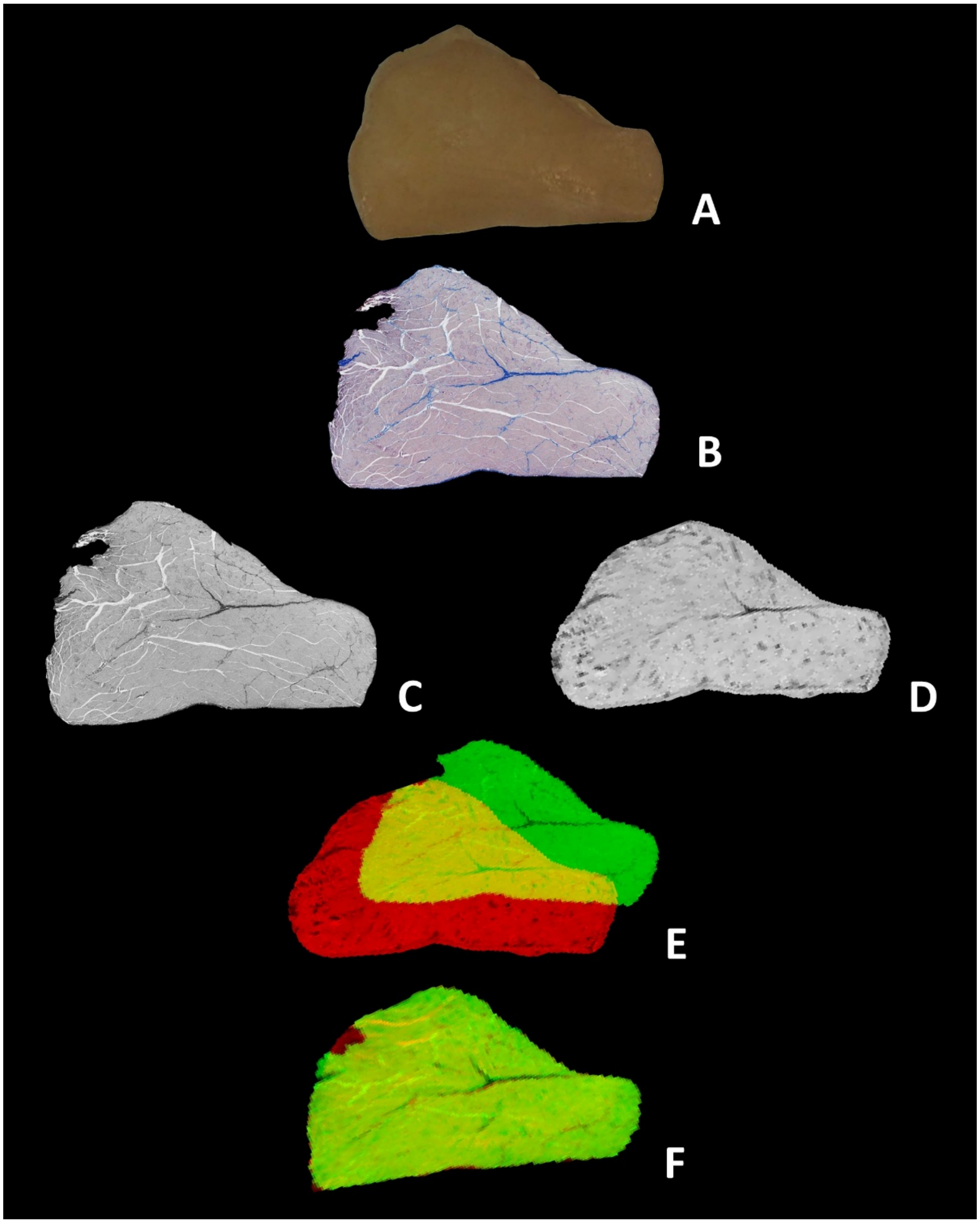

Figure XI. **Stepwise example of the registration process. A-F, Images show the pectineus muscle sectioned at mid-muscle (A), the corresponding trichrome digital image (B), the trichrome image from step B, converted to grayscale (C), and the corresponding MR image (D). Red and green channels were applied to both C (green) and D (red) to allow for alignment (E) and, the final trichrome digital image was registered with the MR image (F).**

(NTotal = Nn + Nsp), pixel area (mm^2; area of one pixel) and total pixel area (mm^2; ATotal = (Nn + Nsp)*pixel area) (Figure XII, C). Fat within each muscle was manually segmented with the pen tool and the areas were added to get total fat in mm^2 by taking µm^2 and dividing by one million (Figure XII, D).

$$Manually\ outlined\ area\ in\ mm^2 = \frac{area\ in\ \mu m^2}{1{,}000{,}000}$$

$$NTotal = Nn + Nsp$$

$$Atotal = \frac{(Nn + Nsp) * pixel\ area}{1{,}000{,}000}$$

The following equations were calculated to determine areas of muscle, fibrous tissue, fat and interstitial space in each manually segmented pectineus muscle analyzed.

$$Area\ of\ muscle\ mm^2 = Nn * pixel\ area$$

$$Area\ of\ fibrous\ tissue\ mm^2 = Nsp * pixel\ area$$

$$Area\ of\ fat\ mm^2 = \frac{manually\ segemented\ area\ of\ fat\ in\ \mu m^2}{1{,}000{,}000}$$

$$\begin{aligned} &Area\ of\ interstitial\ space\ mm^2 \\ &\quad = manually\ outline\ area\ in\ mm^2 \\ &\quad - (area\ of\ muscle\ mm^2 + area\ of\ fibrous\ tissue\ mm^2 \\ &\quad + area\ of\ fat\ mm^2) \end{aligned}$$

The following equations were calculated to determine the percentage of muscle, fibrous tissue, fat and interstitial space in each manually segmented pectineus muscle analyzed.

$$\%\ muscle = \frac{Area\ of\ muscle\ mm^2}{ATotal} * 100$$

$$\% \, fibrous\ tissue = \frac{Area\ of\ fibrous\ tissue\ mm^2}{ATotal} * 100$$

$$\% \, fat = \frac{Area\ of\ fat\ mm^2}{ATotal} * 100$$

$$\% \, interstitial\ space = \frac{Area\ of\ interstitial\ space\ mm^2}{ATotal} * 100$$

IV.3.6 Custom algorithm segmentation of histopathology

One of the authors (SM) first converted histology images from the original NDPI files to TIFF files. A border was drawn around the muscle tissue using GIMP (Figure XII, F). TIFF images were then used for both the registration to MR images described previously and also in the custom algorithm so that both methods of analysis used the same image and borders. A custom, automated algorithm to segment the muscle, fibrous tissue and interstitial space was developed for this study. This novel algorithm included an estimate of inevitable segmentation error given the vast size of the NanoZoomer histology images. Adaptive thresholding was also incorporated in the algorithm to compensate for variations in trichrome staining between samples. This algorithm calculated the percent muscle, percent fibrous tissue and the percent interstitial space within each section (Figure XII, G).

IV.4 Statistical analysis

Descriptive statistics were carried out wherever appropriate by using SigmaPlot® (Version 13, Systat Software, Inc.). Data are presented as mean ± standard error of the mean (SEM). The following data sets were evaluated: 1) 4.7T and 3T MRI measures (T1,

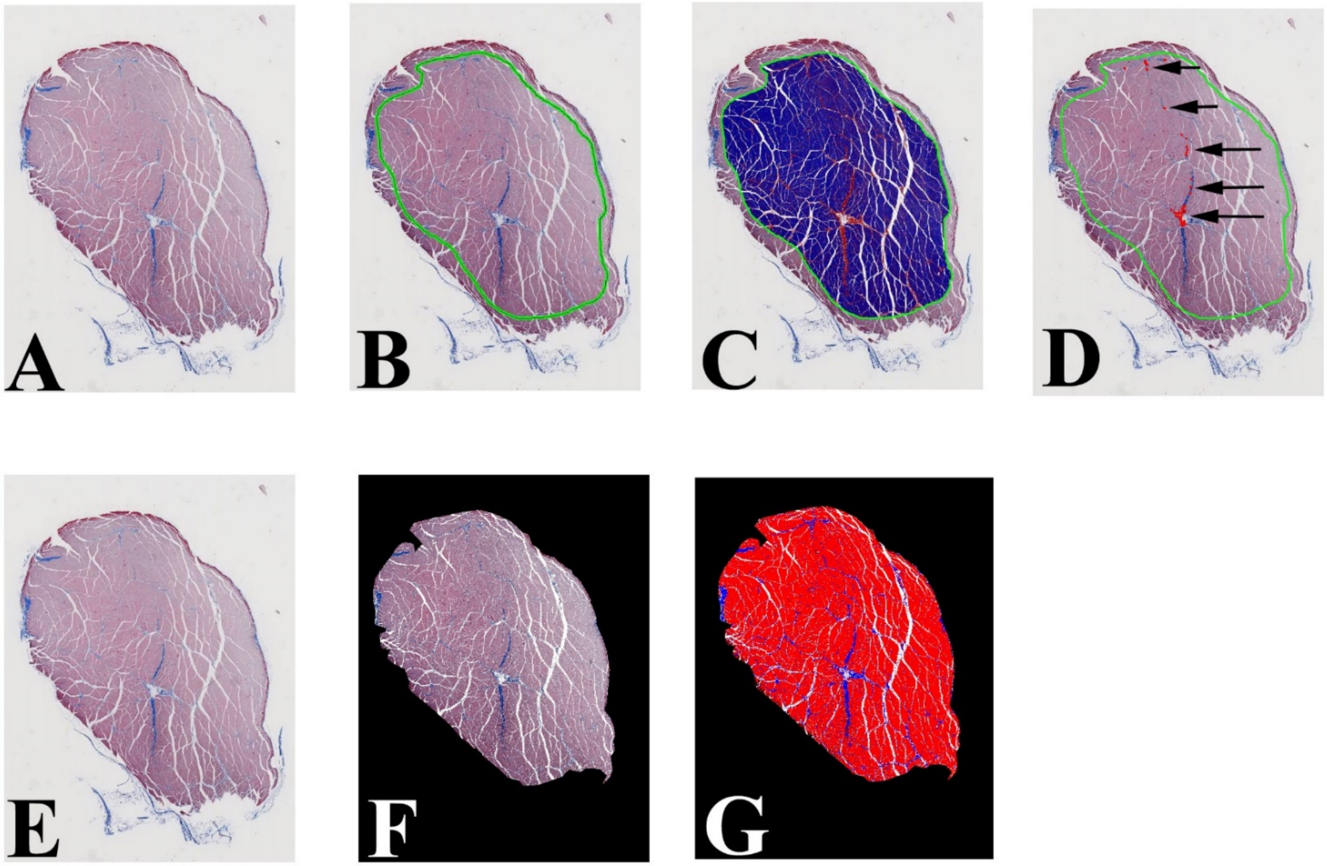

Figure XII. Stepwise example of Aperio histology segmentation and custom algorithm segmentation. A-D, Images from Aperio show the digitalized muscle (A), the manually drawn border (B), the edited Aperio algorithm to quantitate muscle (blue) and fibrous tissue (red) (C), and the manually segmented fat (red, see arrows) (D). E-G, Images from the custom algorithm show the digitalized muscle (E), the mask created to crop the outside borders (F), and the custom algorithm to quantitate muscle (red) and fibrous tissue (blue) (G).

T2, water, fat, FA, ADC) and histology measures (muscle, fibrous tissue, interstitial space, fat), 2) Aperio histology and custom algorithm histology measures (muscle, fibrous tissue, interstitial space, fat), and 3) 4.7T and 3T MRI measures (T1, T2, water, fat, FA, ADC). The MRI metrics and histology segmentations were assessed by calculating the Pearson correlation coefficient (*r*). The strength of correlation coefficients was assessed by the criteria of Portney and Watkins [199]: little to no relationship ($r \leq 0.25$), fair degree of relationship ($r = 0.26 - 0.50$), moderate to good relationship ($r = 0.51 - 0.75$), and good to excellent relationship ($r \geq 0.76$). Measures from the Aperio and custom algorithm segmentation methods as well as measures from the 4.7T and 3T MRI methods were assessed by calculating the Bland-Altman analysis and intraclass correlation coefficient (ICC). A range of agreement was defined as mean bias ± 2.0 SD for the Bland-Altman analysis [200-202]. ICC results were interpreted based on guidelines by Fleiss [203]: excellent relationship ($r > 0.75$), fair to good relationship ($r = 0.40 - 0.75$), and poor relationship ($r < 0.40$).

IV.5 Results

IV.5.1 Correlations between histology and MRI

Pearson correlations between histology and MRI measures are listed in table IX. Significant correlations were identified between both Aperio fat (%) and custom muscle (%) for 4.7T water ($p = <0.001$; 0.004, respectively), fat ($p = <0.001$; 0.004, respectively), and FA ($p = 0.005$; 0.020, respectively). Custom interstitial space (%) correlated positively with 4.7T ADC ($\text{x}10^{-3}$ mm^2/s) ($p = 0.020$). Measures from the 3T scanner did not correlate with any of the histology measures.

Table IX. Pearson correlations between MRI and histology measures

	4.7T						3T					
	T1 (ms)	**T2 (ms)**	**Water (%)**	**Fat (%)**	**FA**	**ADC ($x10^{-3}$ mm2/s)**	**T1 (ms)**	**T2 (ms)**	**Water (%)**	**Fat (%)**	**FA**	**ADC ($x10^{-3}$ mm2/s)**
Aperio % Muscle	0.080	0.392	0.649	-0.649	-0.479	0.014	0.159	0.129	0.004	-0.004	-0.121	0.200
Aperio % Fibrous Tissue	0.027	-0.307	-0.515	0.515	0.351	0.039	-0.114	-0.015	-0.002	0.002	0.075	-0.139
Aperio % Fat	-0.508	-0.604	**-0.972*** **	**0.972*** **	**0.839** **	-0.237	-0.289	-0.566	-0.009	0.009	0.274	-0.383
Aperio % Interstitial Space	0.283	-0.095	0.030	-0.030	-0.294	0.430	0.001	0.392	0.206	-0.206	-0.288	0.191
Custom % Muscle	0.316	0.592	**0.850** **	**-0.850** **	**-0.732* **	0.012	0.355	0.414	0.192	-0.192	-0.202	0.148
Custom % Fibrous Tissue	0.010	-0.383	-0.356	0.356	0.329	0.309	-0.349	-0.107	-0.408	0.408	0.017	0.245
Custom % Interstitial Space	0.199	-0.118	0.292	-0.292	-0.403	**0.751* **	-0.261	0.280	-0.204	0.204	-0.350	0.560

Correlations in bold are significant at *$p < 0.05$, ** $p < 0.01$, *** $p < 0.001$

IV.5.2 Comparisons between histology segmentation methods

Data from nine GRMD dogs evaluated in the histopathology portion of the study are summarized in table X. Fat was manually segmented (SMB) using the Aperio software but the custom algorithm was unable to accurately differentiate fat from the interstitial space compartment.

A Bland-Altman analysis indicated that the 95% limits of agreement between the Aperio segmentation and custom algorithm segmentation for the nine GRMD samples ranged from 2.98 to 18.45 for muscle (%), –1.49 to –22.10 for fibrous tissue (%), and 0.29 to –17.82 for interstitial space (%) (Figure XIII). Muscle and interstitial space (%) had fair to good relationships for ICC (ICC = 0.506; 0.427, respectively) while fibrous tissue (%) had a poor relationship for ICC (ICC = 0.261) (Figure XIV).

While the values between methods for muscle and interstitial space had a good relationship, there were notable discrepancies between methods with the fibrous tissue compartment percentages differing by up to 22%. The custom algorithm consistently overestimated the muscle (%) and underestimated the fibrous tissue (%) and interstitial space (%).

Table X. Muscle, fibrous tissue, interstitial space, and fat values from Aperio and custom algorithm segmentation methods

	Muscle (%)		Fibrous Tissue (%)		Interstitial Space (%)		Fat (%)	
Dog	**Aperio**	**Custom**	**Aperio**	**Custom**	**Aperio**	**Custom**	**Aperio**	**Custom**
1	68.71	83.33	31.29	16.67	34.01	22.59	0.00	--
2	85.32	90.95	14.53	8.94	27.93	18.35	0.15	--
3	76.17	89.81	23.52	9.93	34.54	22.23	0.31	--
4	79.92	84.92	19.45	14.54	16.18	15.56	0.63	--
5	81.66	88.48	18.19	11.40	18.64	16.43	0.15	--
6	55.64	66.45	38.46	17.65	30.18	30.18	5.90	--
7	77.26	89.43	22.70	10.54	21.63	12.26	0.04	--
8	69.76	83.23	30.20	16.74	34.44	25.96	0.04	--
9	67.72	78.96	35.10	20.88	38.75	28.11	0.18	--
Mean	73.24	83.95	25.94	14.14	28.48	19.71	0.82	--
SEM	3.12	2.55	2.73	1.34	2.65	1.76	0.64	--

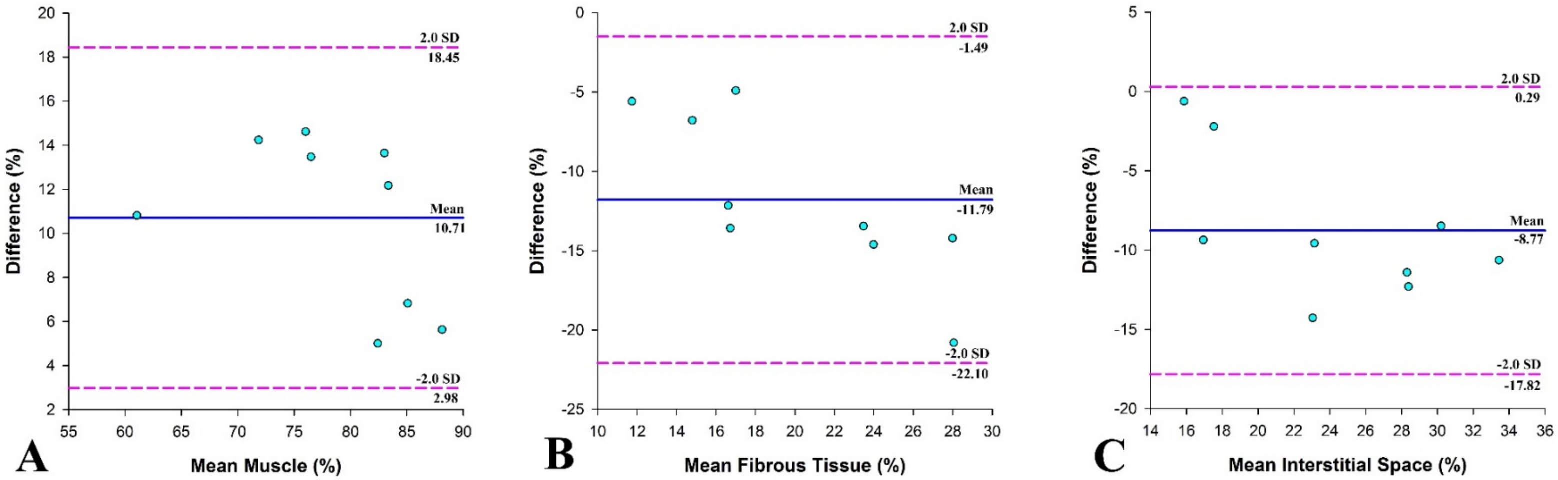

Figure XIII. Bland-Altman plots of measures from Aperio and custom algorithm segmentation methods. A-C, Graphs show mean muscle (A), fibrous tissue (B), and interstitial space (C). Each data point represents values from each animal measured.

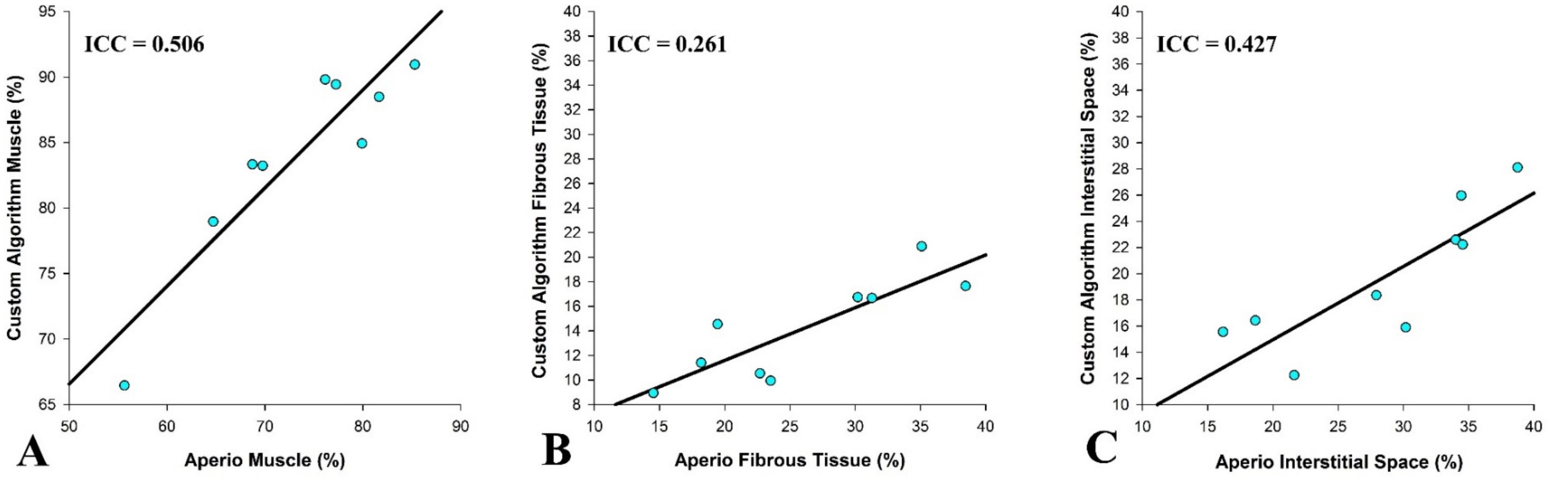

Figure XIV. Scatter plots of correlation between Aperio and custom algorithm segmentation measures. A-C, Graphs show methods plotted (X, Y; Aperio, Custom) for muscle (A), fibrous tissue (B), and interstitial space (C), with intraclass correlation of coefficient (ICC) statistics included in each graph.

IV.5.3 Comparisons between MRI scanners

The data from nine GRMD dogs evaluated in the MRI portion of the study and the values for T1, T2, water, fat, FA, and ADC from both the 4.7T and 3T scanners are summarized in table XI.

A Bland-Altman analysis indicated that the 95% limits of agreement between the 4.7T measures and 3T measures ranged from 167.16 to -168.43 for T1 (ms), 4.11 to 30.76 for T2 (ms), 4.39 to -12.36 for water (%), 12.36 to -4.39 for fat (%), -0.34 to -0.36 for FA, and -0.17 to -0.40 for ADC (x 10^{-3} mm^2/s) (Figure XV). Only T1 had an excellent relationship for ICC (ICC = 0.792) while T2, water, fat, FA, and ADC all had poor relationships (ICC = 0.287; 0.081; 0.081; 0.041; 0.219, respectively) (Figure XVI).

T1 is the only measure that appears to be a reliable between scanners while the other measures are all poorly correlated. Additionally, none of the histology measures correlate with either T1 or any of the 3T MRI metrics.

Table XI. T1, T2, water, fat, fractional anisotropy (FA), and apparent diffusion coefficient (ADC) values from 4.7T and 3T MRI scans

	T1 (ms)		T2 (ms)		Water (%)		Fat (%)		FA		ADC ($x10^{-3}$ mm^2/s)	
Dog	**4.7T**	**3T**	**4.7T**	**3T**	**4.7T**	**3T**	**4.7T**	**3T**	**4.7T**	**3T**	**4.7T**	**3T**
1	677.69	638.91	57.65	72.77	97.09	94.81	2.91	5.19	0.30	0.24	1.32	1.00
2	512.72	513.04	49.86	71.82	97.25	94.76	2.75	5.24	0.29	0.14	1.45	1.20
3	422.35	442.05	44.91	63.72	96.81	93.13	3.19	6.87	0.32	0.13	1.48	1.10
4	319.81	316.33	37.39	49.33	94.96	85.30	5.04	14.70	0.47	0.18	1.45	1.20
5	459.40	461.38	54.96	59.98	97.54	89.85	2.46	10.15	0.33	0.18	1.40	1.10
6	323.03	405.25	35.75	52.13	90.03	92.80	9.97	7.20	0.53	0.19	1.32	1.00
7	603.77	691.01	61.54	79.94	97.41	97.82	2.59	2.18	0.33	0.15	1.17	1.00
8	380.68	421.59	48.36	68.63	97.00	92.66	3.00	7.34	0.33	0.16	1.50	1.20
9	588.49	392.64	44.39	73.36	97.03	88.12	3.00	11.88	0.33	0.08	1.58	1.30
Mean	476.44	475.80	48.31	65.74	96.12	92.14	3.88	7.86	0.36	0.16	1.41	1.12
SEM	42.66	40.13	2.92	3.43	0.80	1.27	0.80	1.27	0.03	0.01	0.04	0.04

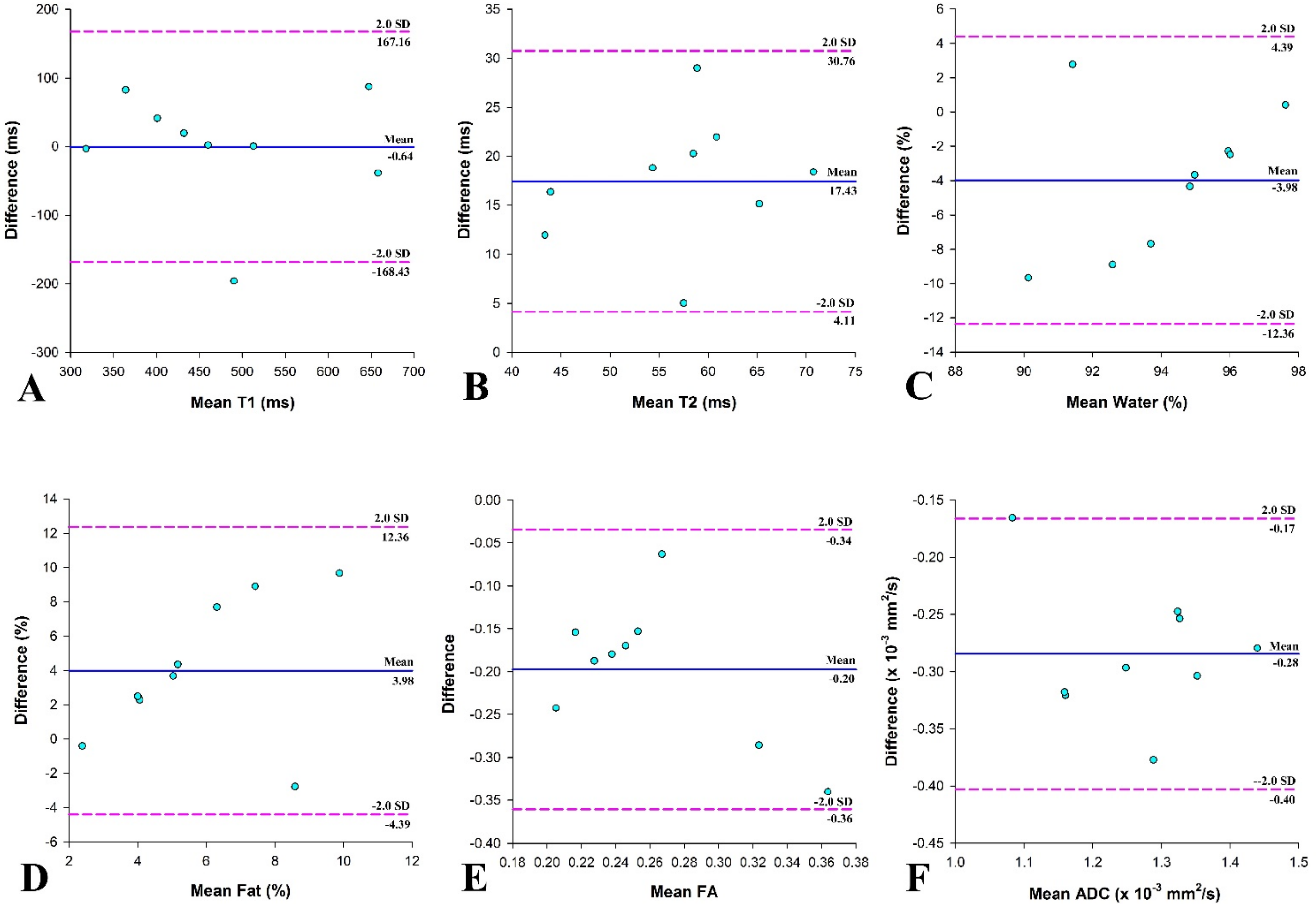

Figure XV. Bland-Altman plots of measures from 4.7T and 3T MRI scanners. A-E, Graphs show mean T1 (A), T2 (B), water (C), fat (D), fractional anisotropy (FA) (E), and apparent diffusion coefficient (ADC) (F). Each data point represents values from each animal measured.

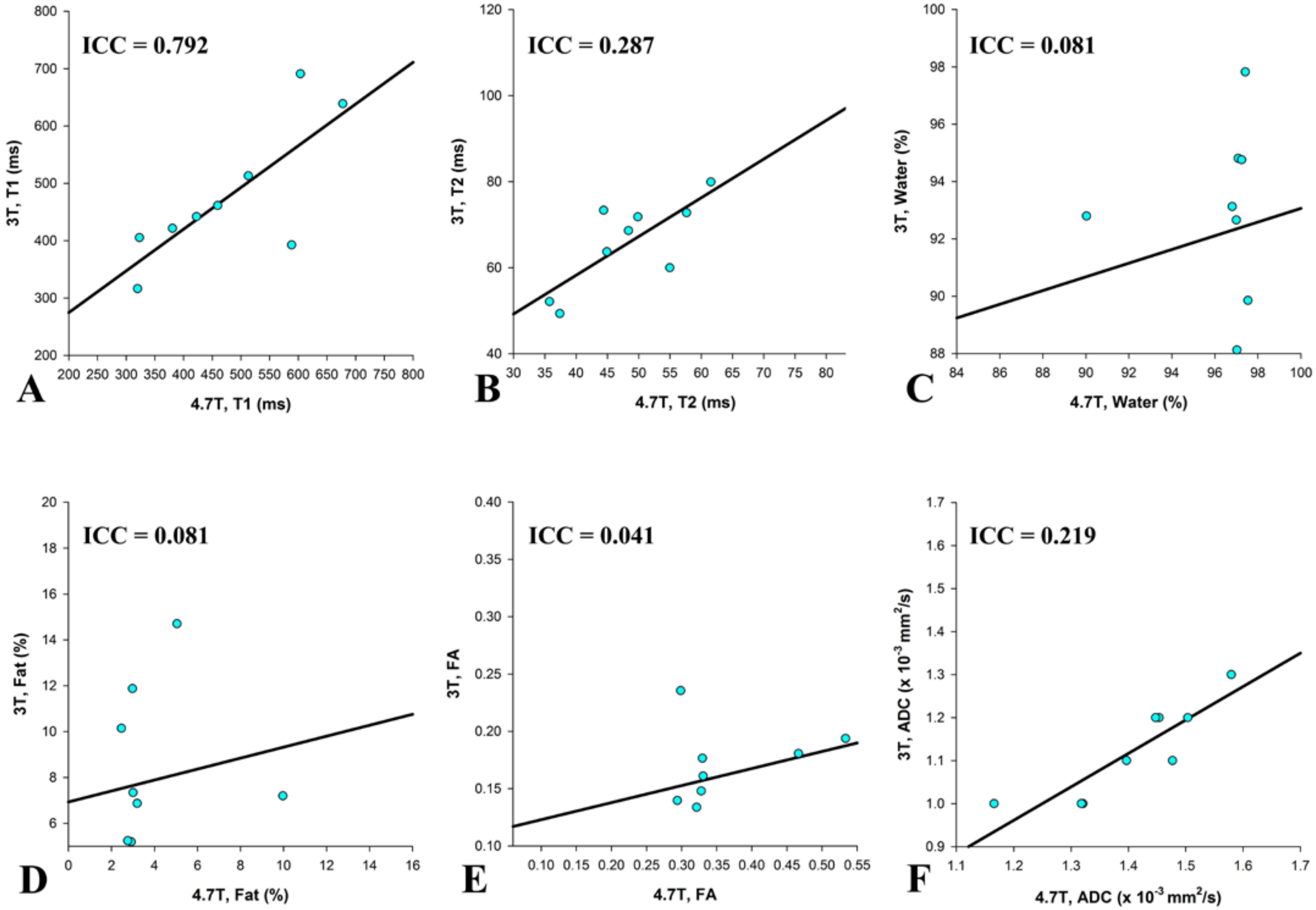

Figure XVI. Scatter plots of correlation between measures with 4.7T and 3T MRI scanners. A-E, Graphs show scanners plotted (X, Y; 4.7T, 3T) for T1 (A), T2 (B), water (C), fat (D), fractional anisotropy (FA) (E), and apparent diffusion coefficient (ADC) (F) with intraclass correlation of coefficient (ICC) statistics included in each graph.

IV.6 Discussion

The use of MRI as a biomarker in DMD has tremendous potential because it is non-invasive, quantifiable, and readily available in nearly all facets of human medicine. MRI has been used to evaluate patients with DMD dating back to the late 80's [74, 204], extending to the use of quantitative parameters to characterize DMD progression in the early 90's [205], and assessment of diffusion tensor imaging (DTI) more recently [90]. Diagnosing DMD and evaluating new therapeutics relies heavily on results obtained from skeletal muscle biopsies. Biopsies have generally been limited to large muscle groups in the thigh and arms as opposed to the more global and systematic assessment offered by MRI. Direct correlation of quantitative histopathology and MR results would allow researchers to more accurately evaluate MR outcome parameters and thus more reliably assess the benefit of new therapeutics.

This study was multifactorial and focused primarily on three aims, 1) register and correlate corresponding histology and MR images of the pectineus muscle using a novel registration technique, 2) compare a commercially available histology segmentation program (Aperio) to a novel custom algorithm for automated histomorphometry, and 3) compare outputs from 4.7T research and 3T clinical scanners to determine potential clinical application of the registration techniques. To the author's knowledge, this is the first study to take this approach in either DMD or GRMD. Several findings in this study were encouraging. First, we were able to use a novel multi-step registration process to successfully align 2D histologic images of the pectineus muscle with the corresponding 3D MR images similar to prior studies of prostate cancer [206, 207] and brain anatomy

[208, 209]. Importantly, these data establish a disease signature for use in clinical trials. However, clinical application of this technique will be limited by the long scan times required for high-resolution MR images. Also, alignment of the five micrometers histology sections and 1-2 mm MR images was challenging. This might be alleviated by using consecutive histology sections that equal MR image slice thickness. Artifacts created in sectioning also caused tissue spacing that doesn't exist on the MR image. Ideally, we would like to develop faster, lower resolution MRI sequences at 3T and 1.5T *in vivo* that could be compared to higher resolution MR and histologic images.

For the most part, we were unable to find significant correlations between measures from MR and histology images. The Aperio segmented fat (%) strongly correlated with the 4.7T fat (%) and also with the FA. But several studies evaluating skeletal muscle DTI have shown that low signal-to-noise ratio (SNR), water T2 value, and percentage fat composition can affect DTI parameters such as overestimating FA [210-212]. Also, in a recent skeletal muscle DTI study in DMD patients they found that low SNR and percentage fat composition can falsely elevate FA [94]. Therefore validity of the FA correlation in this study should be investigated to determine if the SNR was acceptable. MRI metrics have been successfully correlated to pathology in numerous brain injury studies, with FA decreasing in sync with white matter damage on histologic examination [213, 214]. ADC was shown to decrease with higher histopathologic fibrosis stages and also with higher necro-inflammatory grades [215]. The effects of pathology on MRI are complex, poorly understood, and could cancel each other out. For example, fibrosis could reduce T2, fat deposition could increase T2, and they could average each other out so that T2 would not be helpful in staging disease progression.

Confounding factors in this study could include a small sample size, large age distribution among the dogs resulting in various stages of disease progression (3 to 48 months), large region of interest (ROI) analyzed, and volume averaging. Muscle selection could also pose a problem. We chose the pectineus muscle because it's small and spherical making embedment manageable. However, this muscle has only been minimally assessed in GRMD. A relative lack of histopathologic involvement could have precluded lesion and MRI value correlation. *In vivo* longitudinal evaluation of more commonly examined muscles such as the cranial sartorius and vastus lateralis could provide further insight. Additionally, instead of doing whole cross-sectional ROI's, we could use many small ROI's to more closely correlate MR and histology images.

A second focal point of this study was to develop a custom automated algorithm. Traditional methods are labor intensive and can have high interobserver variability depending on the parameters assessed. This could be resolved by automated histomorphometry using high resolution digital whole slide imaging and image analysis software. Analogous techniques have been used for atherosclerotic histology [216], breast cancer [217], bone research [218] and skeletal muscle immunohistochemistry in *mdx* mice [219]. Since the custom algorithm consistently overestimated muscle and underestimated fibrous tissue compared to Aperio, we should reevaluate the histologic sections by manually grading these components to determine which method more closely identifies true pathology. The custom algorithm also failed to reliably differentiate among fat, interstitial space, and white space artifact on slides created when sectioning. Further refinement and optimization of this algorithm can hopefully incorporate fat segmentation. There were several other limitations with our technique. The algorithms in both segmentation models are based on color thresholds. Variability among staining sessions could be countered by running all slides as a single batch. Despite these limitations, we are encouraged and believe this novel segmentation method can be refined and applied to future DMD and GRMD research studies.

Finally, the last aim in this study was to compare outputs from a 4.7T research scanner and a 3T clinical scanner. We concluded that T1 values correlated between scanners but T2, water, fat, FA, and ADC values did not. A study in 2007 compared FA in brain scans using 3T and 1.5T scanners and found significant differences between the machines [220]. Another study comparing 3T to 7T also found differences in FA and mean, radial, and axial diffusivity (MD/RD/AD). The FA was dependent on location in the brain with 7T often giving higher FA values while the MD, RD, and AD were lower at 7T for most ROIs [221]. Therefore differences in magnet strength may make correlating DTI parameters (FA and ADC) difficult. Differences between the water and fat are likely because the resolution for 3T is poor and thus the true fiber structure is not captured. In most cases, the DTI and fat maps (provided by the scanner software) have low SNR resulting in values that should be interpreted carefully. Another reason we may see poor correlation between the fat values is because these samples are very small and based on manual segmentation, most samples had very minimal fat.

Future studies will address full histologic examination of an entire muscle from end to end. In this way, the segmental nature of dystrophic lesions can be better studied, allowing more precise correlation between histologic changes and MRI values. In addition, the registration technique should be updated to account for registration of multiple five micrometer histologic sections and the algorithm should be optimized to segment fat. Taken together, these improvements would facilitate a direct comparison between MR and histologic images.

In conclusion, our finding that MRI and histopathology can be directly correlated through a novel registration technique should improve image analysis in DMD and animal research. We also showed that the two segmentation methods yielded similar results, suggesting that with further optimization, a fully automated algorithm could further enhance future histologic studies. Finally, only T1 values from the 3T clinical scanner compared favorably to those from the 4.7T research scanner and none of the 3T values correlated with histopathology. Detailed correlative studies between histopathology and MRI are imperative if MRI will be used as a biomarker of disease severity and treatment response in future studies involving DMD.

IV.7 Acknowledgements

This research was supported by internal funds rather than specific grants.

CHAPTER V

CONCLUSIONS

The three studies outlined in this dissertation show how important multiple imaging modalities are in identifying disease, evaluating disease progression, and in monitoring disease response to new treatments. Technology continues to advance and with it comes better computers, better software, and better equipment that help us “view” the body from a perspective we once thought unimaginable.

FASD is a devastating disease that continues to plague the U.S. despite our knowledge and education on the effects of alcohol use during pregnancy. Because this problem continues today, we need better methods and techniques to identify affected children. If children are identified at an early age, they could potentially be educated differently. We know that sensitive brain structures responsible for behavior, attention, cognition, learning, memory, socioemotional function, and neurodevelopment among many others can all be affected with prenatal alcohol exposure. MRI allows non-invasive, quantitative analysis of the brain, which is vital to characterizing the detrimental effects of this disease. However, the use of animal models is necessary to control for variables and to be able to provide more detailed studies that can eventually be integrated into clinical evaluations. The sheep model is an excellent large animal model because brain development in utero more closely mimic’s that of human brain development.

The study outlined in chapter II showed how one CT scan could be used to perform quantitative evaluations in not only the soft tissue structures of the face, but also the underlying bone. We discovered that total bone volume is a more sensitive indicator than cranial circumference, which is a common measure used clinically in FAS and FASD. We also discovered that the interorbital distance is highly significant in predicting alcohol exposed lambs and that this measure also correlates to the soft tissue intercanthal width measure. These three measures, total skull bone volume, interorbital distance, and intercanthal width have not been described previously in human FASD studies. Although the segmentation of total skull bone volume can be tedious, and CT is not likely to be used presently in children because of radiation exposure, as technology advances, safer CT scans and automated software are likely to be developed.

Chapter III is an example of how new treatments need validation in animal guided studies prior to their use in human trials. Choline supplementation is recommended during pregnancy for brain and spinal cord development but it is also being evaluated as an interventional strategy to counter the negatives effects of prenatal alcohol exposure in women during pregnancy. This is important for several reasons. First, some women drink unknowingly during their first trimester because they don’t know they are pregnant. We know that sensitive structures in the brain and spinal cord formed during the first trimester can be adversely affected by alcohol exposure. An interventional strategy given at this time may help ameliorate potential negative outcomes associated with exposure. Second, some women are alcoholics and will continue to drink regardless of whether they are pregnant. To successfully implement interventional strategies, extensive animal model studies should first validate their safety and efficacy prior to human use. In human and rodent studies of FASD, choline has been shown to improve memory and learning deficits but minimal work has been done looking at structural brain benefits. In our study we showed binge like alcohol administered prenatally during the first trimester equivalent causes brain volume reductions in peripubertal lambs that this failed to resolve when ewes were administered a choline supplement throughout pregnancy. Although we did not test for behavioral associated benefits, brain volume was still reduced with or without choline supplementation. This finding has not been described previously either in the sheep model of FASD or the human literature.

Finally, chapter IV focused on correlating quantitative imaging with histopathology in the golden retriever model of DMD. DMD is an X-linked recessive disorder, primarily of boys, caused by mutations in the dystrophin gene resulting in progressive muscle wasting and replacement by fat and fibrous tissue. Boys are often wheelchair bound by their early teens die from cardiopulmonary complications by their late 20s to early 30s. There is no cure for DMD so the pursuit of new treatments is constant. While skeletal muscle biopsies are considered a “gold standard” in characterizing DMD, the procedure further compromises DMD boys who are already fragile and lack adequate muscle mass. Accordingly, there is a push to develop non-invasive, quantitative imaging techniques. In this study, we had three central aims, 1) register and correlate corresponding histology and MR images of the pectineus muscle using a novel registration technique, 2) compare a commercially available histology segmentation program (Aperio) to a novel custom algorithm for automated histomorphometry, and 3) compare outputs from 4.7T research and 3T clinical scanners to determine potential clinical application of the registration techniques. We found that histology and MR images co-registered but metrics were poorly correlated. The Aperio software provided similar results to the custom algorithm and with further optimization, a fully automated algorithm could be applied to the current research. Only T1 values were correlated between the 4.7T or 3T scanners. Neither T1 values, nor any of the 3T metrics correlated with histologic segmentations. Future studies in this area will focus on a full histologic examination of an entire muscle from end to end so that the segmental nature of dystrophic lesions can be better characterized in image correlation.

The FASD and DMD studies outlined here are examples of how advanced imaging techniques could be applied, potentially with modification, to characterize numerous diseases. The training I received during my PhD provides me with special insight on the integration of imaging modalities, quantitative techniques, and pathology. This unique niche will make me valuable as a veterinary anatomic pathologist, independent biomedical researcher, and professor.

REFERENCES

1. Purcell, E.M., H.C. Torrey, and R.V. Pound, *Resonance absorption by nuclear magnetic moments in a solid.* Physical Review, 1946. 69(1-2): p. 37-38.

2. Bloch, F., W.W. Hansen, and M. Packard, *Nuclear induction.* Physical Review, 1946. 69(3-4): p. 127-127.

3. Hahn, E.L., *Spin echoes.* Physical Review, 1950. 80(4): p. 580-594.

4. Ernst, R.R., *Nuclear magnetic double resonance with an incoherent radio-frequency field.* The Journal of Chemical Physics, 1966. 45(10): p. 3845-3861.

5. Damadian, R., *Tumor detection by nuclear magnetic resonance.* Science, 1971. 171(3976): p. 1151-1153.

6. Mansfield, P. and P.K. Grannell, *NMR "diffraction" in solids?* Journal of Physics C: Solid State Physics, 1973. 6(22): p. L422-L426.

7. Lauterbur, P.C., *Image formation by induced local interactions: Examples employing nuclear magnetic resonance.* Nature, 1973. 242(5394): p. 190-191.

8. Mansfield, P. and A.A. Maudsley, *Medical imaging by NMR.* Br J Radiol, 1977. 50(591): p. 188-94.

9. Damadian, R., M. Goldsmith, and L. Minkoff, *NMR in cancer: XVI. FONAR image of the live human body.* Physiol Chem Phys, 1977. 9(1): p. 97-100, 108.

10. Edelstein, W.A., et al., *Spin warp NMR imaging and applications to human whole-body imaging.* Physics in Medicine and Biology, 1980. 25(4): p. 751.

11. Hinshaw, W.S., P.A. Bottomley, and G.N. Holland, *Radiographic thin-section image of the human wrist by nuclear magnetic resonance.* Nature, 1977. 270(5639): p. 722-723.

12. Holland, G.N., R.C. Hawkes, and W.S. Moore, *Nuclear magnetic resonance (NMR) tomography of the brain: Coronal and sagittal sections.* J Comput Assist Tomogr, 1980. 4(4): p. 429-33.

13. Wesbey, G.E., M.E. Moseley, and R.L. Ehman, *Translational molecular self diffusion in magnetic resonance imaging. II. Measurement of the self-diffusion coefficient.* Invest Radiol, 1984. 19(6): p. 491-8.

14. Wesbey, G.E., M.E. Moseley, and R.L. Ehman, *Translational molecular self-diffusion in magnetic resonance imaging. I. Effects on observed spin-spin relaxation.* Invest Radiol, 1984. 19(6): p. 484-90.

15. Le Bihan, D., et al., *MR Imaging of intravoxel incoherent motions: Application to diffusion and perfusion in neurologic disorders.* Radiology, 1986. 161(2): p. 401-7.

16. Moseley, M.E., et al., *Diffusion-weighted MR imaging of anisotropic water diffusion in cat central nervous system.* Radiology, 1990. 176(2): p. 439-45.

17. Ogawa, S., et al., *Brain magnetic resonance imaging with contrast dependent on blood oxygenation.* Proceedings of the National Academy of Sciences of the United States of America, 1990. 87(24): p. 9868-9872.

18. Riley, E.P. and C.L. McGee, *Fetal alcohol spectrum disorders: An overview with emphasis on changes in brain and behavior.* Exp Biol Med (Maywood), 2005. 230(6): p. 357-65.

19. CDC, *Alcohol use among pregnant and nonpregnant women of childbearing age - United States, 1991-2005.* MMWR Morb Mortal Wkly Rep, 2009. 58(19): p. 529-32.

20. NIAAA, *NIH statement on international FASD awareness day*, a.d. Kenneth R. Warren, Editor. 2012.

21. Mattson, S.N., et al., *Fetal alcohol syndrome: A case report of neuropsychological, MRI and EEG assessment of two children.* Alcohol Clin Exp Res, 1992. 16(5): p. 1001-3.

22. Clarren, S.K., *Neuropathology in fetal alcohol syndrome*. In: West JR, editor. Alcohol and Brain Development. Oxford University Press; New York, 1986. p. 158-166.

23. Johnson, V.P., et al., *Fetal alcohol syndrome: Craniofacial and central nervous system manifestations.* Am J Med Genet, 1996. 61(4): p. 329-39.

24. Swayze, V.W., 2nd, et al., *Magnetic resonance imaging of brain anomalies in fetal alcohol syndrome.* Pediatrics, 1997. 99(2): p. 232-40.

25. Archibald, S.L., et al., *Brain dysmorphology in individuals with severe prenatal alcohol exposure.* Dev Med Child Neurol, 2001. 43(3): p. 148-54.

26. Lebel, C., et al., *Brain diffusion abnormalities in children with fetal alcohol spectrum disorder.* Alcohol Clin Exp Res, 2008. 32(10): p. 1732-40.

27. Li, Z., et al., *Occipital-temporal reduction and sustained visual attention deficit in prenatal alcohol exposed adults.* Brain Imaging Behav, 2008. 2(1): p. 39-48.

28. Willoughby, K.A., et al., *Effects of prenatal alcohol exposure on hippocampal volume, verbal learning, and verbal and spatial recall in late childhood.* J Int Neuropsychol Soc, 2008. 14(6): p. 1022-33.

29. Sowell, E.R., et al., *Regional brain shape abnormalities persist into adolescence after heavy prenatal alcohol exposure.* Cereb Cortex, 2002. 12(8): p. 856-65.

30. Riley, E.P., et al., *Abnormalities of the corpus callosum in children prenatally exposed to alcohol.* Alcohol Clin Exp Res, 1995. 19(5): p. 1198-202.

31. Bookstein, F.L., et al., *Midline corpus callosum is a neuroanatomical focus of fetal alcohol damage.* Anat Rec, 2002. 269(3): p. 162-74.

32. Bookstein, F.L., et al., *Corpus callosum shape and neuropsychological deficits in adult males with heavy fetal alcohol exposure.* Neuroimage, 2002. 15(1): p. 233-51.

33. Bookstein, F.L., et al., *Many infants prenatally exposed to high levels of alcohol show one particular anomaly of the corpus callosum.* Alcohol Clin Exp Res, 2007. 31(5): p. 868-79.

34. Bhatara, V.S., et al., *Brain function in fetal alcohol syndrome assessed by single photon emission computed tomography.* S D J Med, 2002. 55(2): p. 59-62.

35. Autti-Ramo, I., et al., *MRI findings in children with school problems who had been exposed prenatally to alcohol.* Dev Med Child Neurol, 2002. 44(2): p. 98-106.

36. Boronat, S., et al., *Correlation between morphological MRI findings and specific diagnostic categories in fetal alcohol spectrum disorders.* European Journal of Medical Genetics, 2016.

37. Sowell, E.R., et al., *Abnormal development of the cerebellar vermis in children prenatally exposed to alcohol: Size reduction in lobules I-V.* Alcohol Clin Exp Res, 1996. 20(1): p. 31-4.

38. Mattson, S.N., K.E. Calarco, and A.R. Lang, *Focused and shifting attention in children with heavy prenatal alcohol exposure.* Neuropsychology, 2006. 20(3): p. 361-9.

39. Roebuck, T.M., et al., *Prenatal exposure to alcohol affects the ability to maintain postural balance.* Alcohol Clin Exp Res, 1998. 22(1): p. 252-8.

40. Debaere, F., et al., *Cerebellar and premotor function in bimanual coordination: parametric neural responses to spatiotemporal complexity and cycling frequency.* Neuroimage, 2004. 21(4): p. 1416-27.

41. Roebuck-Spencer, T.M., et al., *Bimanual coordination in alcohol-exposed children: Role of the corpus callosum.* J Int Neuropsychol Soc, 2004. 10(4): p. 536-48.

42. O'Hare, E.D., et al., *Mapping cerebellar vermal morphology and cognitive correlates in prenatal alcohol exposure.* Neuroreport, 2005. 16(12): p. 1285-90.

43. Mattson SN, R.E., Archibald SA, et al, *Caudate volume predicts CVLT-C and WCST performance in children with heavy prenatal alcohol exposure.* Alcohol Clin Exp Res, 2001. 25(Suppl 5)(74A).

44. Mattson, S.N. and E.P. Riley, *A review of the neurobehavioral deficits in children with fetal alcohol syndrome or prenatal exposure to alcohol.* Alcohol Clin Exp Res, 1998. 22(2): p. 279-94.

45. Kodituwakku, P.W., W. Kalberg, and P.A. May, *The effects of prenatal alcohol exposure on executive functioning.* Alcohol Res Health, 2001. 25(3): p. 192-8.

46. Hoover, J.E. and P.L. Strick, *Multiple output channels in the basal ganglia.* Science, 1993. 259(5096): p. 819-21.

47. Kraft, E., et al., *The role of the basal ganglia in bimanual coordination.* Brain Res, 2007. 1151: p. 62-73.

48. Adnams, C.M., et al., *Patterns of cognitive-motor development in children with fetal alcohol syndrome from a community in South Africa.* Alcohol Clin Exp Res, 2001. 25(4): p. 557-62.

49. Connor, P.D., et al., *Effects of prenatal alcohol exposure on fine motor coordination and balance: A study of two adult samples.* Neuropsychologia, 2006. 44(5): p. 744-51.

50. Riikonen, R., et al., *Brain perfusion SPECT and MRI in foetal alcohol syndrome.* Dev Med Child Neurol, 1999. 41(10): p. 652-9.

51. Joseph, J., et al., *Three-dimensional surface deformation-based shape analysis of hippocampus and caudate nucleus in children with fetal alcohol spectrum disorders.* Human Brain Mapping, 2014. 35(2): p. 659-672.

52. Washburn, S.E., et al., *Effects of all three trimester moderate binge alcohol exposure on the foetal hippocampal formation and olfactory bulb.* Brain Inj, 2015. 29(1): p. 104-9.

53. Sowell, E.R., et al., *Abnormal cortical thickness and brain-behavior correlation patterns in individuals with heavy prenatal alcohol exposure.* Cereb Cortex, 2008. 18(1): p. 136-44.

54. Sowell, E.R., et al., *Voxel-based morphometric analyses of the brain in children and adolescents prenatally exposed to alcohol.* Neuroreport, 2001. 12(3): p. 515-23.

55. Sowell, E.R., et al., *Longitudinal mapping of cortical thickness and brain growth in normal children.* J Neurosci, 2004. 24(38): p. 8223-31.

56. Shaw, P., et al., *Intellectual ability and cortical development in children and adolescents.* Nature, 2006. 440(7084): p. 676-9.

57. Cudd, T.A., *Animal model systems for the study of alcohol teratology.* Exp Biol Med (Maywood), 2005. 230(6): p. 389-93.

58. Li, L., et al., *Voxelwise and skeleton-based region of interest analysis of fetal alcohol syndrome and fetal alcohol spectrum disorders in young adults.* Hum Brain Mapp, 2009. 30(10): p. 3265-74.

59. Wozniak, J.R., et al., *Diffusion tensor imaging in children with fetal alcohol spectrum disorders.* Alcohol Clin Exp Res, 2006. 30(10): p. 1799-806.

60. Sowell, E.R., et al., *Mapping white matter integrity and neurobehavioral correlates in children with fetal alcohol spectrum disorders.* J Neurosci, 2008. 28(6): p. 1313-9.

61. Pfefferbaum, A., et al., *Diffusion tensor imaging of deep gray matter brain structures: Effects of age and iron concentration.* Neurobiol Aging, 2010. 31(3): p. 482-93.

62. Cortese, B.M., et al., *Magnetic resonance and spectroscopic imaging in prenatal alcohol-exposed children: Preliminary findings in the caudate nucleus.* Neurotoxicol Teratol, 2006. 28(5): p. 597-606.

63. Fagerlund, A., et al., *Brain metabolic alterations in adolescents and young adults with fetal alcohol spectrum disorders.* Alcohol Clin Exp Res, 2006. 30(12): p. 2097-104.

64. Astley, S.J., et al., *Magnetic resonance spectroscopy outcomes from a comprehensive magnetic resonance study of children with fetal alcohol spectrum disorders.* Magn Reson Imaging, 2009. 27(6): p. 760-78.

65. Riikonen, R.S., et al., *Deep serotonergic and dopaminergic structures in fetal alcoholic syndrome: A study with nor-beta-CIT-single-photon emission computed tomography and magnetic resonance imaging volumetry.* Biol Psychiatry, 2005. 57(12): p. 1565-72.

66. Clark, C.M., et al., *Structural and functional brain integrity of fetal alcohol syndrome in nonretarded cases.* Pediatrics, 2000. 105(5): p. 1096-9.

67. Malisza, K.L., et al., *Evaluation of spatial working memory function in children and adults with fetal alcohol spectrum disorders: A functional magnetic resonance imaging study.* Pediatr Res, 2005. 58(6): p. 1150-7.

68. Astley, S.J., et al., *Functional magnetic resonance imaging outcomes from a comprehensive magnetic resonance study of children with fetal alcohol spectrum disorders.* J Neurodev Disord, 2009. 1(1): p. 61-80.

69. Spadoni, A.D., et al., *BOLD response during spatial working memory in youth with heavy prenatal alcohol exposure.* Alcohol Clin Exp Res, 2009. 33(12): p. 2067-76.

70. Sowell, E.R., et al., *Functional magnetic resonance imaging of verbal learning in children with heavy prenatal alcohol exposure.* Neuroreport, 2007. 18(7): p. 635-9.

71. O'Hare, E.D., et al., *Altered frontal-parietal functioning during verbal working memory in children and adolescents with heavy prenatal alcohol exposure.* Hum Brain Mapp, 2009. 30(10): p. 3200-8.

72. Fryer, S.L., et al., *Characterization of white matter microstructure in fetal alcohol spectrum disorders.* Alcohol Clin Exp Res, 2009. 33(3): p. 514-21.

73. Hoffman, E.P., R.H. Brown, Jr., and L.M. Kunkel, *Dystrophin: The protein product of the Duchenne muscular dystrophy locus.* Cell, 1987. 51(6): p. 919-28.

74. Murphy, W.A., W.G. Totty, and J.E. Carroll, *MRI of normal and pathologic skeletal muscle.* AJR Am J Roentgenol, 1986. 146(3): p. 565-74.

75. Huang, Y., et al., *Quantitative MR relaxometry study of muscle composition and function in Duchenne muscular dystrophy.* Journal of Magnetic Resonance Imaging, 1994. 4(1): p. 59-64.

76. Kuriyama, M., et al., *MR imaging of myopathy.* Comput Med Imaging Graph, 1989. 13(4): p. 329-33.

77. Marden, F.A., et al., *Compositional analysis of muscle in boys with Duchenne muscular dystrophy using MR imaging.* Skeletal Radiol, 2005. 34(3): p. 140-8.

78. Matsumura, K., et al., *Proton spin-lattice relaxation time of Duchenne dystrophy skeletal muscle by magnetic resonance imaging.* Muscle Nerve, 1988. 11(2): p. 97-102.

79. Matsumura, K., et al., *Duchenne muscular dystrophy carriers. Proton spin-lattice relaxation times of skeletal muscles on magnetic resonance imaging.* Neuroradiology, 1989. 31(5): p. 373-6.

80. Sookhoo, S., et al., *MRI for the demonstration of subclinical muscle involvement in muscular dystrophy.* Clin Radiol, 2007. 62(2): p. 160-5.

81. Garrood, P., et al., *MR imaging in Duchenne muscular dystrophy: Quantification of T1-weighted signal, contrast uptake, and the effects of exercise.* J Magn Reson Imaging, 2009. 30(5): p. 1130-8.

82. Mathur, S., et al., *Age-related differences in lower-limb muscle cross-sectional area and torque production in boys with Duchenne muscular dystrophy.* Arch Phys Med Rehabil, 2010. 91(7): p. 1051-8.

83. Akima, H., et al., *Relationships of thigh muscle contractile and non-contractile tissue with function, strength, and age in boys with Duchenne muscular dystrophy.* Neuromuscul Disord, 2012. 22(1): p. 16-25.

84. Kim, H.K., et al., *T2 mapping in Duchenne muscular dystrophy: Distribution of disease activity and correlation with clinical assessments.* Radiology, 2010. 255(3): p. 899-908.

85. Wren, T.A., et al., *Three-point technique of fat quantification of muscle tissue as a marker of disease progression in Duchenne muscular dystrophy: Preliminary study.* AJR Am J Roentgenol, 2008. 190(1): p. W8-12.

86. Kan, H.E., et al., *In vivo 31P MRS detection of an alkaline inorganic phosphate pool with short T1 in human resting skeletal muscle.* NMR Biomed, 2010. 23(8): p. 995-1000.

87. Torriani, M., et al., *Lower leg muscle involvement in Duchenne muscular dystrophy: An MR imaging and spectroscopy study.* Skeletal Radiol, 2012. 41(4): p. 437-45.

88. Kim, H.K., et al., *Quantitative skeletal muscle MRI: Part 2, MR spectroscopy and T2 relaxation time mapping-comparison between boys with Duchenne muscular dystrophy and healthy boys.* AJR Am J Roentgenol, 2015. 205(2): p. W216-23.

89. Hsieh, T.J., et al., *Muscle metabolism in Duchenne muscular dystrophy assessed by in vivo proton magnetic resonance spectroscopy.* J Comput Assist Tomogr, 2009. 33(1): p. 150-4.

90. Ponrartana, S., et al., *Effectiveness of diffusion tensor imaging in assessing disease severity in Duchenne muscular dystrophy: Preliminary study.* Pediatr Radiol, 2015. 45(4): p. 582-9.

91. Qi, J., et al., *Diffusion-weighted imaging of inflammatory myopathies: Polymyositis and dermatomyositis.* J Magn Reson Imaging, 2008. 27(1): p. 212-7.

92. Ai, T., et al., *Diffusion tensor imaging in evaluation of thigh muscles in patients with polymyositis and dermatomyositis.* Br J Radiol, 2014. 87(1043): p. 20140261.

93. Froeling, M., et al., *Muscle changes detected with diffusion-tensor imaging after long-distance running.* Radiology, 2015. 274(2): p. 548-62.

94. Hooijmans, M.T., et al., *Evaluation of skeletal muscle DTI in patients with Duchenne muscular dystrophy.* NMR Biomed, 2015. 28(11): p. 1589-97.

95. Ambrose, J., *Computerized transverse axial scanning (tomography). 2. Clinical application.* Br J Radiol, 1973. 46(552): p. 1023-47.

96. Hounsfield, G.N., *Computerized transverse axial scanning (tomography). 1. Description of system.* Br J Radiol, 1973. 46(552): p. 1016-22.

97. Jones, K.L. and D.W. Smith, *Recognition of the fetal alcohol syndrome in early infancy.* Lancet, 1973. 302(7836): p. 999-1001.

98. Bertrand, J., L.L. Floyd, and M.K. Weber, *Guidelines for identifying and referring persons with fetal alcohol syndrome.* MMWR Recomm Rep, 2005. 54(Rr-11): p. 1-14.

99. Wattendorf, D.J. and M. Muenke, *Fetal alcohol spectrum disorders.* Am Fam Physician, 2005. 72(2): p. 279-82, 285.

100. Astley, S.J. and S.K. Clarren, *Diagnosing the full spectrum of fetal alcohol-exposed individuals: Introducing the 4-digit diagnostic code.* Alcohol, 2000. 35(4): p. 400-10.

101. Sokol, R.J. and S.K. Clarren, *Guidelines for use of terminology describing the impact of prenatal alcohol on the offspring.* Alcohol Clin Exp Res, 1989. 13(4): p. 597-8.

102. Aase, J.M., K.L. Jones, and S.K. Clarren, *Do we need the term "FAE"?* Pediatrics, 1995. 95(3): p. 428-30.

103. Hoyme, H.E., et al., *A practical clinical approach to diagnosis of fetal alcohol spectrum disorders: Clarification of the 1996 institute of medicine criteria.* Pediatrics, 2005. 115(1): p. 39-47.

104. Leibson, T., et al., *The differential diagnosis of fetal alcohol spectrum disorder.* J Popul Ther Clin Pharmacol, 2014. 21(1): p. e1-e30.

105. May, P.A., et al., *Prevalence and epidemiologic characteristics of FASD from various research methods with an emphasis on recent in-school studies.* Dev Disabil Res Rev, 2009. 15(3): p. 176-92.

106. Lupton, C., L. Burd, and R. Harwood, *Cost of fetal alcohol spectrum disorders.* Am J Med Genet C Semin Med Genet, 2004. 127c(1): p. 42-50.

107. CDC, *Alcohol use and binge drinking among women of childbearing age--United States, 2006-2010.* MMWR Morb Mortal Wkly Rep, 2012. 61(28): p. 534-8.

108. Smith, S.M., et al., *Neural crest development in fetal alcohol syndrome.* Birth Defects Res C Embryo Today, 2014. 102(3): p. 210-20.

109. Conover, E.A. and K.L. Jones, *Safety concerns regarding binge drinking in pregnancy: A review.* Birth Defects Res A Clin Mol Teratol, 2012. 94(8): p. 570-5.

110. Maier, S.E. and J.R. West, *Drinking patterns and alcohol-related birth defects.* Alcohol Research & Health: The Journal Of The National Institute On Alcohol Abuse And Alcoholism, 2001. 25(3): p. 168-174.

111. Ramadoss, J., et al., *Binge alcohol exposure during all three trimesters alters bone strength and growth in fetal sheep.* Alcohol, 2006. 38(3): p. 185-92.

112. Moore, K.L., *The developing human : Clinically oriented embryology*, ed. T.V.N. Persaud and M.G. Torchia. 2013, Philadelphia, Pa.: Philadelphia, Pa. : Saunders/Elsevier.

113. Sulik, K.K., C.S. Cook, and W.S. Webster, *Teratogens and craniofacial malformations: Relationships to cell death.* Development, 1988. 103 Suppl: p. 213-31.

114. Smith, S.M., *Alcohol-induced cell death in the embryo.* Alcohol Health Res World, 1997. 21(4): p. 287-97.

115. Cartwright, M.M. and S.M. Smith, *Increased cell death and reduced neural crest cell numbers in ethanol-exposed embryos: Partial basis for the fetal alcohol syndrome phenotype.* Alcohol Clin Exp Res, 1995. 19(2): p. 378-86.

116. Rovasio, R.A. and N.L. Battiato, *Role of early migratory neural crest cells in developmental anomalies induced by ethanol.* Int J Dev Biol, 1995. 39(2): p. 421-22.

117. O'Rahilly, R. and F. Müller, *Human embryology and teratology*. 2nd ed. 1996: Wiley-Liss, Inc., New York.

118. Reynolds, M.L. and K. Mollgard, *The distribution of plasma proteins in the neocortex and early allocortex of the developing sheep brain.* Anat Embryol (Berl), 1985. 171(1): p. 41-60.

119. Sulik, K.K., *Craniofacial defects from genetic and teratogen-induced deficiencies in presomite embryos.* Birth Defects Orig Artic Ser, 1984. 20(3): p. 79-98.

120. Hernandez-Guerrero, J.C., C. Ledesma-Montes, and J.P. Loyola-Rodriguez, *Effects of maternal ethanol intake on second alcoholic generation murine skull and mandibular size.* Arch Med Res, 1998. 29(4): p. 297-302.

121. Robin, N.H. and E.H. Zackai, *Unusual craniofacial dysmorphia due to prenatal alcohol and cocaine exposure.* Teratology, 1994. 50(2): p. 160-4.

122. Anthony, B., et al., *Alcohol-induced facial dysmorphology in C57BL/6 mouse models of fetal alcohol spectrum disorder.* Alcohol, 2010. 44(7-8): p. 659-71.

123. Lipinski, R.J., et al., *Ethanol-induced face-brain dysmorphology patterns are correlative and exposure-stage dependent.* PLoS One, 2012. 7(8): p. e43067.

124. *The Merck Veterinary Manual*. Veterinary manual, ed. C.M. Kahn and S. Line. 2005, Whitehouse Station, N.J.: Whitehouse Station, N.J. : Merck & Co.

125. Schmidt, E.J., et al., *Micro-computed tomography-based phenotypic approaches in embryology: Procedural artifacts on assessments of embryonic craniofacial growth and development.* BMC Dev Biol, 2010. 10: p. 18.

126. Shen, L., et al., *Effect of prenatal alcohol exposure on bony craniofacial development: A mouse MicroCT study.* Alcohol, 2013. 47(5): p. 405-15.

127. Kaminen-Ahola, N., et al., *Maternal ethanol consumption alters the epigenotype and the phenotype of offspring in a mouse model.* PLoS Genet, 2010. 6(1): p. e1000811.

128. Washburn, S.E., et al., *Acute alcohol exposure, acidemia or glutamine administration impacts amino acid homeostasis in ovine maternal and fetal plasma.* Amino Acids, 2013. 45(3): p. 543-54.

129. Jones, K.L., et al., *Developmental pathogenesis of short palpebral fissure length in children with fetal alcohol syndrome.* Birth defects research. Part A, Clinical and molecular teratology, 2009. 85(8): p. 695-699.

130. Streissguth, A.P., et al., *Fetal alcohol syndrome in adolescents and adults.* JAMA, 1991. 265(15): p. 1961-7.

131. Streissguth, A.P., *A long term perspective of FAS.* Alcohol Health & Research World, 1994. 18(1): p. 8.

132. Moore, E.S., et al., *Unique facial features distinguish fetal alcohol syndrome patients and controls in diverse ethnic populations.* Alcohol Clin Exp Res, 2007. 31(10): p. 1707-13.

133. Astley, S.J., *Comparison of the 4-digit diagnostic code and the Hoyme diagnostic guidelines for fetal alcohol spectrum disorders.* Pediatrics, 2006. 118(4): p. 1532-45.

134. Jones, K.L., et al., *Fetal alcohol spectrum disorders: Extending the range of structural defects.* Am J Med Genet A, 2010. 152a(11): p. 2731-5.

135. Carter, R.C., et al., *Fetal alcohol-related growth restriction from birth through young adulthood and moderating effects of maternal prepregnancy weight.* Alcohol Clin Exp Res, 2013. 37(3): p. 452-62.

136. Ortega-Garcia, J.A., et al., *Head circumference at birth and exposure to tobacco, alcohol and illegal drugs during early pregnancy.* Childs Nerv Syst, 2012. 28(3): p. 433-9.

137. Hunold, P., et al., *Radiation exposure during cardiac CT: Effective doses at multi-detector row CT and electron-beam CT.* Radiology, 2003. 226(1): p. 145-52.

138. Chudley, A.E., et al., *Fetal alcohol spectrum disorder: Canadian guidelines for diagnosis.* CMAJ, 2005. 172(5 Suppl): p. S1-s21.

139. Parnell, S.E., et al., *Maternal oral intake mouse model for fetal alcohol spectrum disorders: Ocular defects as a measure of effect.* Alcohol Clin Exp Res, 2006. 30(10): p. 1791-8.

140. Thompson, B.L., P. Levitt, and G.D. Stanwood, *Prenatal exposure to drugs: Effects on brain development and implications for policy and education.* Nat Rev Neurosci, 2009. 10(4): p. 303-12.

141. Guerri, C., A. Bazinet, and E.P. Riley, *Foetal Alcohol Spectrum Disorders and alterations in brain and behaviour.* Alcohol Alcohol, 2009. 44(2): p. 108-14.

142. Ismail, S., et al., *Screening, diagnosing and prevention of fetal alcohol syndrome: Is this syndrome treatable?* Dev Neurosci, 2010. 32(2): p. 91-100.

143. Pollard, I., *Neuropharmacology of drugs and alcohol in mother and fetus.* Semin Fetal Neonatal Med, 2007. 12(2): p. 106-13.

144. Goodlett, C.R., K.H. Horn, and F.C. Zhou, *Alcohol teratogenesis: Mechanisms of damage and strategies for intervention.* Exp Biol Med (Maywood), 2005. 230(6): p. 394-406.

145. Ware, A.L., et al., *The effects of prenatal alcohol exposure and attention-deficit/hyperactivity disorder on psychopathology and behavior.* Alcohol Clin Exp Res, 2013. 37(3): p. 507-16.

146. Suttie, M., et al., *Facial dysmorphism across the fetal alcohol spectrum.* Pediatrics, 2013. 131(3): p. e779-88.

147. Idrus, N.M. and J.D. Thomas, *Fetal alcohol spectrum disorders: Experimental treatments and strategies for intervention.* Alcohol Res Health, 2011. 34(1): p. 76-85.

148. Ballard, M.S., M. Sun, and J. Ko, *Vitamin A, folate, and choline as a possible preventive intervention to fetal alcohol syndrome.* Med Hypotheses, 2012. 78(4): p. 489-93.

149. Zeisel, S.H. and K.A. da Costa, *Choline: An essential nutrient for public health.* Nutr Rev, 2009. 67(11): p. 615-23.

150. Institute of Medicine Standing Committee on the Scientific Evaluation of Dietary Reference, I., O.B.V. its Panel on Folate, and Choline, *The National Academies Collection: Reports funded by National Institutes of Health,* in *Dietary Reference Intakes for Thiamin, Riboflavin, Niacin, Vitamin B6, Folate, Vitamin B12, Pantothenic Acid, Biotin, and Choline*. 1998, National Academies Press (US) Washington (DC).

151. Zeisel, S.H., *What choline metabolism can tell us about the underlying mechanisms of fetal alcohol spectrum disorders.* Mol Neurobiol, 2011. 44(2): p. 185-91.

152. Shaw, G.M., et al., *Choline and risk of neural tube defects in a folate-fortified population.* Epidemiology, 2009. 20(5): p. 714-9.

153. Thomas, J.D., E.J. Abou, and H.D. Dominguez, *Prenatal choline supplementation mitigates the adverse effects of prenatal alcohol exposure on development in rats.* Neurotoxicol Teratol, 2009. 31(5): p. 303-11.

154. Ryan, S.H., J.K. Williams, and J.D. Thomas, *Choline supplementation attenuates learning deficits associated with neonatal alcohol exposure in the rat: effects of varying the timing of choline administration.* Brain Res, 2008. 1237: p. 91-100.

155. Thomas, J.D., et al., *Choline supplementation following third-trimester-equivalent alcohol exposure attenuates behavioral alterations in rats.* Behav Neurosci, 2007. 121(1): p. 120-30.

156. Thomas, J.D., et al., *Prenatal choline supplementation mitigates behavioral alterations associated with prenatal alcohol exposure in rats.* Birth Defects Res A Clin Mol Teratol, 2010. 88(10): p. 827-37.

157. Thomas, J.D., et al., *Neonatal choline supplementation ameliorates the effects of prenatal alcohol exposure on a discrimination learning task in rats.* Neurotoxicol Teratol, 2000. 22(5): p. 703-11.

158. Monk, B.R., F.M. Leslie, and J.D. Thomas, *The effects of perinatal choline supplementation on hippocampal cholinergic development in rats exposed to alcohol during the brain growth spurt.* Hippocampus, 2012. 22(8): p. 1750-7.

159. Thomas, J.D., M. Garrison, and T.M. O'Neill, *Perinatal choline supplementation attenuates behavioral alterations associated with neonatal alcohol exposure in rats.* Neurotoxicol Teratol, 2004. 26(1): p. 35-45.

160. Wagner, A.F. and P.S. Hunt, *Impaired trace fear conditioning following neonatal ethanol: Reversal by choline.* Behav Neurosci, 2006. 120(2): p. 482-7.

161. Thomas, J.D. and T.D. Tran, *Choline supplementation mitigates trace, but not delay, eyeblink conditioning deficits in rats exposed to alcohol during development.* Hippocampus, 2012. 22(3): p. 619-30.

162. Coles, C.D., et al., *Dose and timing of prenatal alcohol exposure and maternal nutritional supplements: Developmental effects on 6-month-old infants.* Matern Child Health J, 2015. 19(12): p. 2605-14.

163. Sawant, O.B., et al., *Different patterns of regional purkinje cell loss in the cerebellar vermis as a function of the timing of prenatal ethanol exposure in an ovine model.* Neurotoxicol Teratol, 2013. 35: p. 7-13.

164. Maier, S.E., and West, J.R., *Drinking patterns and alcohol-related birth defects.* Alcohol Research & Health, 2001. 25(3): p. 168-174.

165. Denic, A., et al., *MRI in rodent models of brain disorders.* Neurotherapeutics, 2011. 8(1): p. 3-18.

166. Moore, E.M., et al., *Fetal alcohol spectrum disorders: Recent neuroimaging findings.* Curr Dev Disord Rep, 2014. 1(3): p. 161-172.

167. Rajaprakash, M., et al., *Cortical morphology in children with alcohol-related neurodevelopmental disorder.* Brain Behav, 2014. 4(1): p. 41-50.

168. De Guio, F., et al., *A study of cortical morphology in children with fetal alcohol spectrum disorders.* Hum Brain Mapp, 2014. 35(5): p. 2285-96.

169. Yang, Y., et al., *Abnormal cortical thickness alterations in fetal alcohol spectrum disorders and their relationships with facial dysmorphology.* Cereb Cortex, 2012. 22(5): p. 1170-9.

170. de Zeeuw, P., et al., *Prenatal exposure to cigarette smoke or alcohol and cerebellum volume in attention-deficit/hyperactivity disorder and typical development.* Transl Psychiatry, 2012. 2: p. e84.

171. Spadoni, A.D., et al., *Neuroimaging and fetal alcohol spectrum disorders.* Neurosci Biobehav Rev, 2007. 31(2): p. 239-45.

172. Donald, K.A., et al., *Neuroimaging effects of prenatal alcohol exposure on the developing human brain: A magnetic resonance imaging review.* Acta Neuropsychiatr, 2015. 27(5): p. 251-69.

173. Bookstein, F.L., et al., *Damage to the human cerebellum from prenatal alcohol exposure: The anatomy of a simple biometrical explanation.* Anat Rec B New Anat, 2006. 289(5): p. 195-209.

174. Cardenas, V.A., et al., *Automated cerebellar segmentation: Validation and application to detect smaller volumes in children prenatally exposed to alcohol.* Neuroimage Clin, 2014. 4: p. 295-301.

175. Parnell, S.E., et al., *Dysmorphogenic effects of first trimester-equivalent ethanol exposure in mice: A magnetic resonance microscopy-based study.* Alcohol Clin Exp Res, 2014. 38(7): p. 2008-14.

176. Parnell, S.E., et al., *Magnetic resonance microscopy defines ethanol-induced brain abnormalities in prenatal mice: Effects of acute insult on gestational day 8.* Alcohol Clin Exp Res, 2009. 33(6): p. 1001-11.

177. Wozniak, J.R., et al., *Choline supplementation in children with fetal alcohol spectrum disorders has high feasibility and tolerability.* Nutr Res, 2013. 33(11): p. 897-904.

178. Yushkevich, P.A., et al., *User-guided 3D active contour segmentation of anatomical structures: Significantly improved efficiency and reliability.* Neuroimage, 2006. 31(3): p. 1116-28.

179. Parnell, S.E., et al., *Magnetic resonance microscopy-based analyses of the neuroanatomical effects of gestational day 9 ethanol exposure in mice.* Neurotoxicol Teratol, 2013. 39: p. 77-83.

180. Maier, S.E., et al., *Fetal alcohol exposure and temporal vulnerability: Regional differences in cell loss as a function of the timing of binge-like alcohol exposure during brain development.* Alcohol Clin Exp Res, 1999. 23(4): p. 726-34.

181. Godin, E.A., et al., *Magnetic resonance microscopy defines ethanol-induced brain abnormalities in prenatal mice: Effects of acute insult on gestational day 7.* Alcohol Clin Exp Res, 2010. 34(1): p. 98-111.

182. O'Leary-Moore, S.K., et al., *Magnetic resonance microscopy-based analyses of the brains of normal and ethanol-exposed fetal mice.* Birth Defects Res A Clin Mol Teratol, 2010. 88(11): p. 953-64.

183. McDouall, R.M., M.J. Dunn, and V. Dubowitz, *Nature of the mononuclear infiltrate and the mechanism of muscle damage in juvenile dermatomyositis and Duchenne muscular dystrophy.* J Neurol Sci, 1990. 99(2-3): p. 199-217.

184. Petrof, B.J., et al., *Dystrophin protects the sarcolemma from stresses developed during muscle contraction.* Proc Natl Acad Sci U S A, 1993. 90(8): p. 3710-4.

185. Robinson-Hamm, J.N. and C.A. Gersbach, *Gene therapies that restore dystrophin expression for the treatment of Duchenne muscular dystrophy*. Hum Genet, 2016. 135(9): p. 1029-40.

186. Kemaladewi, D.U. and R.D. Cohn, *Exon snipping in Duchenne muscular dystrophy*. Trends Mol Med, 2016. 22(3): p. 187-9.

187. Hoffman, E.P., et al., *Restoring dystrophin expression in Duchenne muscular dystrophy muscle progress in exon skipping and stop codon read through.* Am J Pathol, 2011. 179(1): p. 12-22.

188. Emery, A.E.H. and F. Muntoni (eds.), *Duchenne muscular dystrophy*. Oxford University Press; New York, 2003. Third edition.

189. Schmalbruch, H., *Regenerated muscle fibers in Duchenne muscular dystrophy: a serial section study*. Neurology, 1984. 34(1): p. 60-5.

190. Rubin, R., et al., *Rubin's Pathology : Clinicopathologic foundations of medicine*. 2008: Philadelphia : Lippincott Williams & Wilkins, [2008]. Fifth edition.

191. Anderson, J.R., *Muscular Dystrophy*, in *atlas of skeletal muscle pathology*. 1985, Springer Netherlands: Dordrecht. p. 67-74.

192. Finanger, E.L., et al., *Use of skeletal muscle MRI in diagnosis and monitoring disease progression in Duchenne muscular dystrophy*. Physical medicine and rehabilitation clinics of North America, 2012. 23(1): p. 1-ix.

193. Gutpell, K. and L. Hoffman, *Non-invasive assessment of skeletal muscle pathology and treatment for Duchenne muscular dystrophy*. OA Musculoskeletal Medicine, 2013. 1(4): p. 33.

194. Kornegay, J.N., et al., *Canine models of Duchenne muscular dystrophy and their use in therapeutic strategies.* Mamm Genome, 2012. 23(1-2): p. 85-108.

195. Kornegay, J.N., et al., *NBD delivery improves the disease phenotype of the golden retriever model of Duchenne muscular dystrophy*. Skeletal Muscle, 2014. 4(1): p. 18.

196. Fan, Z., et al., *Characteristics of magnetic resonance imaging biomarkers in a natural history study of golden retriever muscular dystrophy*. Neuromuscul Disord, 2014. 24(2): p. 178-91.

197. Deroulers, C., et al., *Analyzing huge pathology images with open source software.* Diagn Pathol, 2013. 8: p. 92.

198. Mortensen, E.N. and W.A. Barrett, *Interactive segmentation with intelligent scissors.* Graphical models and image processing, 1998. 60(5): p. 349-384.

199. Portney, L.G. and M.P. Watkins, *Foundations of clinical research : Applications to practice*. 3rd ed. ed. 2009, Upper Saddle River, N.J. :: Pearson/Prentice Hall.

200. Bland, J.M. and D.G. Altman, *Comparing methods of measurement: Why plotting difference against standard method is misleading.* The Lancet, 1995. 346(8982): p. 1085-1087.

201. Bland, J.M. and D.G. Altman, *Measuring agreement in method comparison studies.* Stat Methods Med Res, 1999. 8(2): p. 135-60.

202. Martin Bland, J. and D. Altman, *Statistical methods for assessing agreement between two methods of clinical measurement.* The Lancet, 1986. 327(8476): p. 307-310.

203. Fleiss, J.L., *Reliability of Measurement*, in *The Design and Analysis of Clinical Experiments*. 1999, John Wiley & Sons, Inc. p. 1-32.

204. Schreiber, A., et al., *Magnetic resonance imaging of children with Duchenne muscular dystrophy*. Pediatr Radiol, 1987. 17(6): p. 495-7.

205. Huang, Y., et al., *Quantitative MR relaxometry study of muscle composition and function in Duchenne muscular dystrophy*. J Magn Reson Imaging, 1994. 4(1): p. 59-64.

206. Reynolds, H.M., et al., *Development of a registration framework to validate MRI with histology for prostate focal therapy*. Medical Physics, 2015. 42(12): p. 7078-7089.

207. Kwak, J.T., et al., *Correlation of magnetic resonance imaging with digital histopathology in prostate.* Int J Comput Assist Radiol Surg, 2016. 11(4): p. 657-66.

208. Adler, D.H., et al., *Histology-derived volumetric annotation of the human hippocampal subfields in postmortem MRI.* NeuroImage, 2014. 84: p. 10.1016/j.neuroimage.2013.08.067.

209. Osechinskiy, S. and F. Kruggel, *Slice-to-volume nonrigid registration of histological sections to MR images of the human brain.* Anatomy Research International, 2011. 2011.

210. Froeling, M., et al., *DTI of human skeletal muscle: the effects of diffusion encoding parameters, signal-to-noise ratio and T2 on tensor indices and fiber tracts.* NMR Biomed, 2013. 26(11): p. 1339-52.

211. Williams, S.E., et al., *Quantitative effects of inclusion of fat on muscle diffusion tensor MRI measurements.* J Magn Reson Imaging, 2013. 38(5): p. 1292-7.

212. Damon, B.M., *Effects of image noise in muscle diffusion tensor (DT)-MRI assessed using numerical simulations.* Magn Reson Med, 2008. 60(4): p. 934-44.

213. Herrera, J.J., et al., *Acute white matter tract damage after frontal mild traumatic brain injury.* J Neurotrauma, 2016.

214. Tu, T.W., et al., *Radiological-pathological correlation of diffusion tensor and magnetization transfer imaging in a closed head traumatic brain injury model.* Ann Neurol, 2016. 79(6): p. 907-20.

215. Franca, M., et al., *Evaluation of fibrosis and inflammation in diffuse liver diseases using intravoxel incoherent motion diffusion-weighted MR imaging.* Abdom Radiol (NY), 2016.

216. van Engelen, A., et al., *Automated segmentation of atherosclerotic histology based on pattern classification.* Journal of Pathology Informatics, 2013. 4(2): p. 3-3.

217. Hiary, H., et al., *Automated segmentation of stromal tissue in histology images using a voting Bayesian model.* Signal, Image and Video Processing, 2013. 7(6): p. 1229-1237.

218. Zhang, L., et al., *Analysis of new bone, cartilage, and fibrosis tissue in healing murine allografts using whole slide imaging and a new automated histomorphometric algorithm.* Bone Research, 2016. 4: p. 15037.

219. Smith, L.R. and E.R. Barton, *SMASH – semi-automatic muscle analysis using segmentation of histology: A MATLAB application.* Skeletal Muscle, 2014. 4(1): p. 21.

220. Fushimi, Y., et al., *Fractional anisotropy and mean diffusivity: Comparison between 3.0-T and 1.5-T diffusion tensor imaging with parallel imaging using histogram and region of interest analysis.* NMR Biomed, 2007. 20(8): p. 743-8.

221. Zhan, L., et al., *Magnetic resonance field strength effects on diffusion measures and brain connectivity networks.* Brain Connectivity, 2013. 3(1): p. 72-86.